Title
Experimental Investigation of Proppant Flow and Transport in Intersected Hydraulic Fractures

Author
Ma, Wenpei

Publication Date
2020

Peer reviewed|Thesis/dissertation

UNIVERSITY OF CALIFORNIA SAN DIEGO

Experimental Investigation of Proppant Flow and Transport in Intersected Hydraulic Fractures

A thesis submitted in partial satisfaction of the requirements
for the degree Master of Science

in

Geotechnical Engineering

by

Wenpei Ma

Committee in charge:

Professor Ingrid Tomac, Chair
Professor John S McCartney
Professor Qiang Zhu

2020

The Thesis of Wenpei Ma is approved and it is acceptable in quality and form for publication on microfilm and electronically:

____

____

____

Chair

University of California San Diego

2020

DEDICATION

To my parents for their everlasting love and support.

TABLE OF CONTENTS

LIST OF FIGURES

LIST OF TABLES

ACKNOWLEDGEMENTS

First of all, I would like to express my deepest gratitude to my advisor, Dr. Ingrid Tomac, for her guidance, advice, support, and patience. I am so grateful for her supervision during the research project. Her enthusiastic and rigorous attitude in research enlightened my passion in learning and research and leads me to become a better researcher.

I would also like to thank Professor John S. McCartney for his help on providing suggestions on preparing the experiment. I also appreciate him and his group allowing me to borrow some tools from their laboratory.

I would like to thank Brain Yamashiro for his peer critiques and helps in theoretical part of the experiment. I want to thank Mahta Movasat, Shijun Wei, and Justin Perng for providing helps on preparing experiments.

Finally, I would like to thank my family and friends for their helps and supports.

ABSTRACT OF THE THESIS

Experimental Investigation of Proppant Flow and Transport in Intersected Hydraulic Fractures

by

Wenpei Ma

Master of Science in Geotechnical Engineering

University of California San Diego, 2020

Professor Ingrid Tomac, Chair

This study investigates proppant flow and transport in intersecting fractures at angles typical for intersections of pre-existing and new hydraulic fractures. Proppant is small granular material, which is placed into hydraulic fractures during geothermal and hydrocarbon reservoir stimulation and props the fluid paths open during reservoir exploitation. This study uses plexiglas laboratory slot experiments enhanced with an advanced image analysis for identifying particle trajectories and quantifying slurry velocities. Although proppant flow and transport has been broadly studied, the effects of intersecting fracture angles have not, especially coupled with fluid viscosities, flow rates, and proppant volumetric concentration effects. This study specifically investigates the role of intermediate fracture angles, which have been identified to occur most frequently when the new hydraulic fractures intercept the existing ones. Results show that proppant flow and transport behavior after the intersection is very sensitive to carrying fluid viscosity and flow rates alteration, while differentiating proppant volumetric concentrations have a limited effect. Fracture intersection angle itself has a clear effect on proppant flow velocities and proppant settlement; furthermore, it enhances the effects from fluid viscosity, fluid flow rates, and proppant volumetric concentrations. This study also studies the proppant agglomeration phenomenon in intersecting fractures. Different shapes of agglomerations are observed and categorized.

CHAPTER 1: INTRODUCTION

1.1 Background and Motivation

Proppant is small, synthetic, or natural, granular material widely used in gas and oil industry, and geothermal reservoirs during hydraulic fracturing for permeability enhancement and production improvement of reservoirs. Proppant is pumped together with fracturing fluid and subsequently placed into fractures to keep them open for a long-term reservoir exploitation. Although many researchers have investigated flow and transport of proppant into planar and simplified fractures, the flow and transport of proppants in different shapes of fracture systems has not yet been fully understood. Simple planar newly formed fractures could easily evolve to complex system while interacting with existing fractures, which has been shown in recent numerical and experimental studies (Zhang et al., 2007; Dayan et al. 2009; Sahai, 2012; Wong et al., 2013; Sahai et al., 2014; Aimene and Ouenes, 2015; Alotaibi and Miskimins, 2015; Li et al., 2016; Luo and Tomac, 2018a; Luo and Tomac, 2018b; Tong and Mohanty, 2016; Wen et al., 2016; Zou et al., 2016; Chang et al., 2017; Kesireddy, 2017; Kou et al., 2018; Pan et al., 2018; Fjaestad and Tomac, 2019; Kumar and Ghassemi, 2019; Sahai and Moghanloo, 2019; Hampton et al., 2019; Nandlal and Weijermars, 2019).

Although several previous studies investigated the deposited sand dune geometry in complex fracture systems in experimental slots, a relationship between the governing parameters which affect proppant placement efficiency through intersecting fractures at different angles have not yet been quantified. The governing parameters, which have been previously identified to affect the efficiency of proppant flow and transport in complex fracture systems, are intersecting fracture angles, fluid dynamic viscosity, slurry flow rate, and proppant concentration. This study uses micromechanics and quantifies slurry velocity field using Particle Image Velocimetry using the GeoPIV method, which can help understanding of how and to which extent relevant parameters govern the proppant flow and transport through fracture intersections. This study quantifies experimental results at a small scale of detail for two intersecting fracture angles, 30° and 45°.

1.2 Research Objectives

The specific objectives of this study are to better understand:

1. The effect of fracture intersection angle on proppant flow, transport, and settlement.
2. How variations of relevant parameters such as are proppant volumetric concentration, carrying fluid viscosity and fluid flow rate affect proppant flow and transport in intersected fracture and what their combined effect is.

1.3 Thesis Structure

The organization of this thesis is described below:

Chapter 1 provides an introduction, motivation and research objectives.

Chapter 2 introduces the past findings on proppant flow and transport in hydraulic fractures. Specific findings include role of proppant in hydraulic fractures, transportation of proppants in plane smooth fractures, transportation of proppant in complex smooth fractures, and phenomenon of particle agglomeration.

Chapter 3 describes experimental setups and methodology, including proppant selection, fluid selection and flow rate design, fracture geometry design, camera selection and video quality design, system setup, experiment scheme, the GeoPIV method, analysis approach and accuracy assessment.

In chapter 4 results and analysis are presented and discussed. Results include findings from visual observations of all experiments, direct and processed GeoPIV results. Analysis part includes effect of fracture intersection angles, effect of proppant volumetric concentrations, effect of flow rate, effect of fluid viscosity, and correlation between the slope of settled proppants and proppant flow velocity.

Chapter 5 provides conclusion and recommendations for future work based on this experiment. References are listed at the end of this thesis.

CHAPTER 2: LITERATURE REVIEW

2.1 Hydraulic Fracturing and Role of Proppant

Hydraulic fracturing is used for geothermal reservoirs permeability enhancement. This processes helps to expand current fractures, create new fractures, and maintain the conductivity of fractures. Hydraulic fracturing is generally used in low-permeability rocks such as igneous rock for geothermal energy extraction or tight sandstone and shale for hydrocarbon extractions. During hydraulic fracturing, pressurized fluid is introduced into subsurface through drilled wells, and new fractures form. Subsequently, a slurry of particles and fluid are injected into newly formed fractures to keep them open for a long term reservoir operation. Figure 2.1 shows an illustration of use of hydraulic fracturing process for Enhanced Geothermal Systems (EGS). As new or recycled cold fluids are injected to hot bed layers, fluid is heated during the process by surrounding rocks and extracted into the power plant to consume geothermal energy and transform into other form of energy such as electricity.

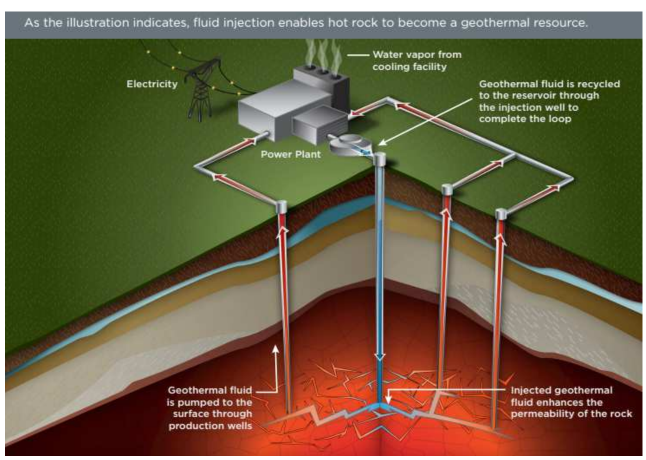

Figure 2.1 Illustration of Hydraulic Fracturing Process (from ImpactHound, referred from US Department of Energy)

Figure 2.2 shows the potential geothermal energy in United States. Most of usable geothermal resources are concentrated in the west part of the States, especially in Oregon, Idaho, Nevada, Utah, Colorado, New Mexico, Arizona and California.

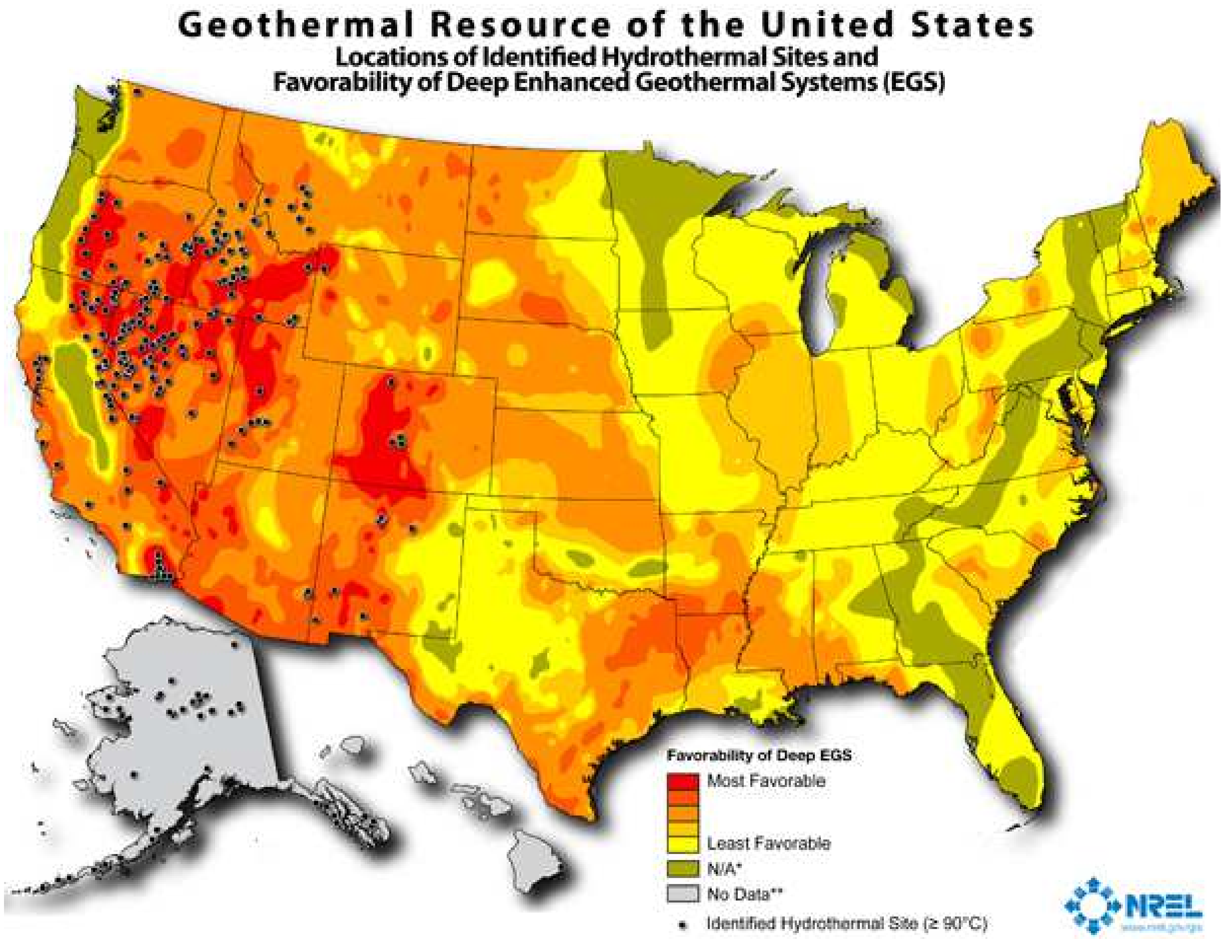

Figure 2.2 Geothermal Energy Potential of USA (from US Energy Information Administration, referred from National Renewable Energy Laboratory)

Figures 2.3 and 2.4 show the pilot geothermal plants and geothermal yield capacity worldwide. Geothermal plants are installed in the United States, Central America, Japan, Southeast

Asia, Oceania, East Africa, Tibet, Central Europe, etc. The United States has the largest geothermal yield capacity worldwide. Followings are Philippines, Indonesia, New Zealand, Italy, Iceland, Kenya, Japan, etc.

Figure 2.3 Geothermal Plants Worldwide (from ThinkGeoEnergy)

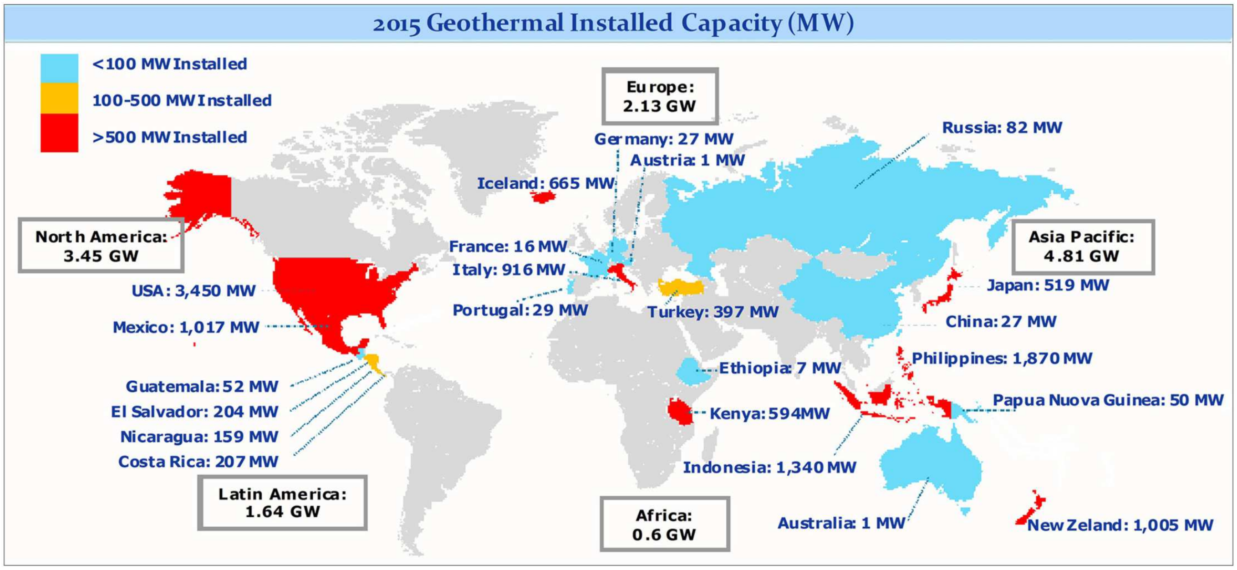

Figure 2.4 Geothermal Capacity Worldwide in 2015 (from Lund et al., 2015)

Most hydraulic fracturing jobs includes fracturing fluids and proppants. Proppants can be natural sands, which are favorable and environmentally friendly, but also synthetic. Proppant use can be critical to the hydraulic fracturing treatment. The main purpose of adding proppants into the fracturing fluid is to hold the fracture walls and maintain the fracture open so that the conductivity is guaranteed. A good proppant selection and design is beneficial to the conductivity of the fracturing treatment. Fracture conductivity is generally controlled by proppant physical properties, proppant composition and level of proppant degradation. Consideration of physical properties of proppants may include proppant strength, grain size and grain-size distribution, quantities of fines and potential impurities, roundness, density, etc. The majority source of fracking sands (proppants) are produced from Wisconsin and Minnesota, see Figure 2.5. Other minor sources include Black Mesa Basin in Utah and Arizona, Liano Uplift in Texas, Wavy Arch in Kentucky and Ohio, Valley and Ridge in the Appalachians.

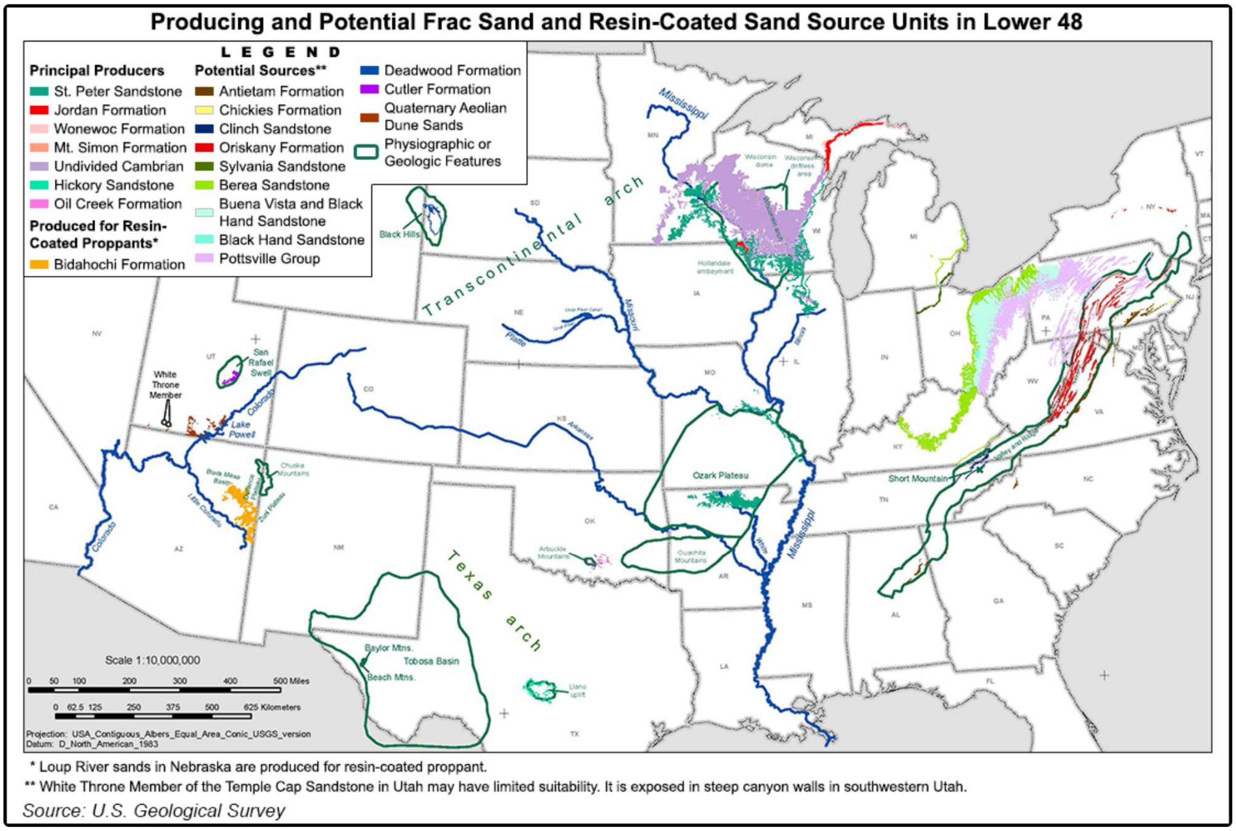

Figure 2.5 Major Proppant Production Resources in the United States (from NGI, referred from USGS)

2.2 Proppant Flow and Transport

Laboratory experiments of proppant flow and transport in planar hydraulic fractures have been performed for several decades. Researchers have identified and developed many major observations, conclusions, and theories about proppant settling, flow and transport. However, majority of real fractures is not planar, linear and smooth.

The first experiment on complex fractures was conducted by Dayan et al. (2009). Dayan et al (2009) found that proppant will not flow into secondary fractures if the flow rate in the primary fracture is too low and until proppant settled enough in the primary fractures. A few studies performed experimental parametric analyses to better understand different proppant flow and transport behaviors (Sahai, 2012; Sahai et al., 2014; Alotaibi and Miskimins, 2015; Li et al., 2016; Tong and Mohanty, 2016; Wen et al., 2016; ; Kesireddy, 2017; Pan et al., 2018; Sahai and Moghanloo, 2019).

Sahai (2012) observed that proppant falls into secondary fracture from primary fracture purely due to gravity effects; in addition, the proppant concentration has small effect on the secondary fractures sandbank height compared with flow rate, smaller proppants segregate more significantly and are easier to transport into secondary fractures and secondary fractures that are closer to the wellbore injection point will receive more proppant.

Sahai et al. (2014) found out that proppant travel efficiency through secondary fractures is related to fluid flow rate, proppant concentration, and proppant size.

Li et al. (2016) studied the effect of angles in Y-like shaped intersection, where two of the fractures in the same plane are called primary fractures. The dune height in secondary fracture therefore decreases, and the total propped area along primary fractures increases as the intersection angle between primary and secondary fractures increases from 30° to 90°. For 30° some proppants continue moving in the original flow direction, some of the proppant flows into the intersected fracture. For 90° most proppants continue moving in the original flow direction, only a few flows into the secondary fracture. In that way, dune height in the secondary fracture decreases as intersection angle increases. Tong and Mohanty (2016) confirmed the results done by Li et al. (2016) for the intersection angle beyond 90°.

Wen et al. (2016) found out that there is an immediate sandbank height change right after the 90° intersection corner, which is more significant if the intersection is closer to wellbore injection location. Viscosity is identified as a dominant parameter for proppant transport in a secondary fracture closer to the injection location, while gravity plays a more important role for secondary fractures further away (Wen et al., 2016).

Alotaibi and Miskimins (2015) further extended the experiment made by Sahai and Moghanloo by considering the effect of particle surface roughness and concluded that angular sands have better transport characteristics.

Pan et al. (2018) confirmed that fluid flow rate dominates proppant transport in secondary fractures and the proppant settlement length in secondary fractures is inversely proportional to the intersection angle.

Kesireddy (2017) also showed how the fluid flow rate dominantly controls the proppant transport in secondary fractures and found that the sandbank height will significantly increase in secondary fractures with increasing primary fracture width.

2.3 Particle Agglomeration

Particle agglomeration and clustering have been predominately studied for better understanding suspensions in chemistry and chemical engineering fields. Although there are many experiments on this topic (Guala et al., 2008; Saw et al., 2008; Fiabane et al., 2012), numerical simulations prevail (Ho and Sommerfeld, 2002; Raiskinmäki et al., 2003; Bec et al., 2005; Gualtieri et al., 2009; Li et al, 2011; Gustavsson et al., 2014; Reeks, 2014).

Ho and Sommerfeld (2002) pointed out that particle agglomeration in turbulent flow according to numerical models is governed by stochastic collision model, collision efficiency due to particle geometry and size differences, and agglomeration efficiency determined by sticking potential due to the van der Waals forces.

Raiskinmäki (2003) studied shear flow of particulate suspension and found that clusters formed in the Couette flow can be divided into rotating chain-like clusters and layers of particles at the channel wall; the size distribution of the rotating clusters is scale invariant in the small-cluster regime and decreases rapidly above a characteristic length scale that diverges at a jamming transition; the behavior of cluster can be qualitatively divided into three categories according to Reynolds number.

Bec et al. (2005) studied clustering of heavy particles in smooth flow and concluded that inertia enhances collision rates by two ways, where its correlation with particle positions caused by carrying fluid flow is high and where corresponds to location that velocity field is not differentiable; a phenomenological model yields an estimate of collision rates for particle pairs with different sizes.

Guala et al. (2008) did experimental investigations and found that large particles tend to cluster in strain-dominated regions; preferential concentration (clusters and voids) occur on scales comparable with the Taylor microscale, a length scale that characterize a turbulent flow, which combines the effect of kinematic viscosity of fluid, root mean square of the velocity fluctuation, and the rate of energy dissipation.

Saw et al. (2008) observed experimental evidence of spatial clusters of dense particles in homogeneous, isotropic turbulent flow at high Reynolds numbers regime; the dissipation-scale clustering becomes stronger as the Stokes number increases and is found to exhibit similarity with respect to the droplet Stokes number over a range of experimental conditions (particle diameter and turbulent energy dissipation rate).

Gualtieri et al. (2009) did numerical simulations and concluded that the homogeneity of particle configurations is broken by interaction of local eddies; shear indirectly affects the geometry of the clusters by imprinting anisotropy on large-scale velocity fluctuation; anisotropic clustering may occur in the phase when isotropy is recovering depending on Stokes relaxation time of particle.

Fiabane et al. (2012) observed in experiments that neutrally buoyant particles do not have significant clustering phenomenon while heavy particles cluster a lot.

Gustavsson et al. (2014) did numerical simulation and find out that clustering of small particles in incompressible random velocity fields may be reduced or enhanced by the effect of gravity depending on Stokes number of the particles and may be strongly anisotropic.

In recent years, researchers in hydraulic fracturing and geo-energy industry noticed and have been actively studying particle agglomerations in proppant flow and transport. Investigations on effects of particle concentrations, fluid viscosity, fracture shape, fracture roughness and many other parameters have been done (Tomac and Gutierrez, 2014; Tomac and Gutierrez, 2015; Luo and Tomac, 2018a). Tomac and Gutierrez (2015) found that lubrication effect dramatically impacts particle motions when a combination of parameters is unfavorable. Lubrication forces in narrow fractures act upon particle-particle and particle-wall collisions and cause particle agglomerations by decreasing the post-impact kinetic energy of particles. Adjacent particles stay together and form clumps, while fluid flows around clusters. As fluid viscosity and/or proppant concentration increases, agglomerations are more frequently observed. Luo and Tomac (2018a) confirmed effects of lubrication forces experimentally, and showed that proppant concentration and fluid viscosity have dominantly positive effects on agglomeration. Furthermore, wall effects at low particle diameter to wall distance has a strong effect on agglomeration and wall effect is enhanced on rough surfaces than smooth surface.

2.4 Reynolds Number and Stokes Numbers

Particle Reynolds number is an important indicator showing how particles move in a suspension during the slurry transport and sediment process. The Reynolds number is the ratio of inertial forces to viscous forces within fluid, where the particle Reynolds number is used for motion of an object in fluid and characterizes the nature of the surrounding flow. It is a function of the particle diameter, the fluid density, the particle horizontal velocity and the fluid viscosity. Particle Reynolds number is defined in following equation (Reynolds, 1883, Rhodes 1989):

$$Re_p = \frac{\rho_f \cdot v \cdot d_s}{\mu_f} \tag{2.1}$$

where ρ_f is the fluid density, v is the particle velocity, d_s is the particle diameter, and μ_f is the fluid dynamic viscosity. A larger particle Reynolds number indicates the particle is flowing in a more turbulent environment. For particle Reynolds number up to 10, it is within laminar flow regime. For particle Reynolds number larger than 500, it is within turbulent flow regime.

Stokes Number was named by Gabriel Stokes, who set foundations of understanding of sphere motion in fluid (Stokes, 1851). Stokes number is defined as the ratio of the characteristic time of a particle to a characteristic time of the flow. It is a function of the particle density, the particle vertical velocity, the particle diameter, the fracture aperture, and the fluid dynamic viscosity. In the case of Stokes flow, when the particle Reynolds number is less than unity and the particle drag coefficient is inversely proportional to the Reynolds number, the Stokes number is defined by following equation:

$$St = \frac{\rho_s \cdot v_i \cdot d_s^2}{18 \cdot w \cdot \mu_f} \tag{2.2}$$

where, ρ_s is the particle density, v_i is the average particle settling velocity, d_s is the particle diameter, w is the fracture aperture, and μ_f is the fluid viscosity. A larger Stokes number indicates the particle is behaving less dependent on the fluid flow characteristics. As Stokes number approaches to infinity, particle behaves completely unrelated to fluid flow. A particle with a low Stokes number perfectly follows the fluid streamlines.

CHAPTER 3: EXPERIMENTAL SETUP AND METHODOLOGY

3.1 Introduction

This research uses experimental setup to investigate proppant flow and transport through two plexiglass fractures which contain two different intersecting angles. The intersecting angles are chosen as representative for the most common fracture intersections documented in hydraulic fracturing of granite. Proppant particles are injected into a fracture filled with slickwater solution at different flow rates and particle volumetric concentrations. Experiments are recorded with high resolution scientific video cameras, and the conclusions are drawn from visual observations, dune measurements and the GeoPIV video analysis.

3.2 Proppant Selection

Since the focus of this work is to investigate effects of fracture geometry configuration, only one type of original sand type is selected for all tests, so that sieved selected batches of Ottawa F65 sand are used at varied concentrations. Prior to mixing sand with water, the sand is sieved and washed to remove very fine dusts. This modified and selected Ottawa Sand then was used for all experiments. Figure 3.1 shows the physical appearance of test sands. The sand is round, light-colored, and fine graded and sieved between 60/100 mesh, which is a mesh size widely used in hydraulic fracturing. The mean particle diameter is 0.2 mm. Figure 3.2 below shows the general size distribution of Ottawa F65 Sands (El Ghoraiby et al., 2020) and the curve of the sieved batch used for the experiments. The No. 60 and No. 100 mesh boundaries are also highlighted in the figure.

Figure 3.1 Physical Appearance of Sand Used in the Experiment

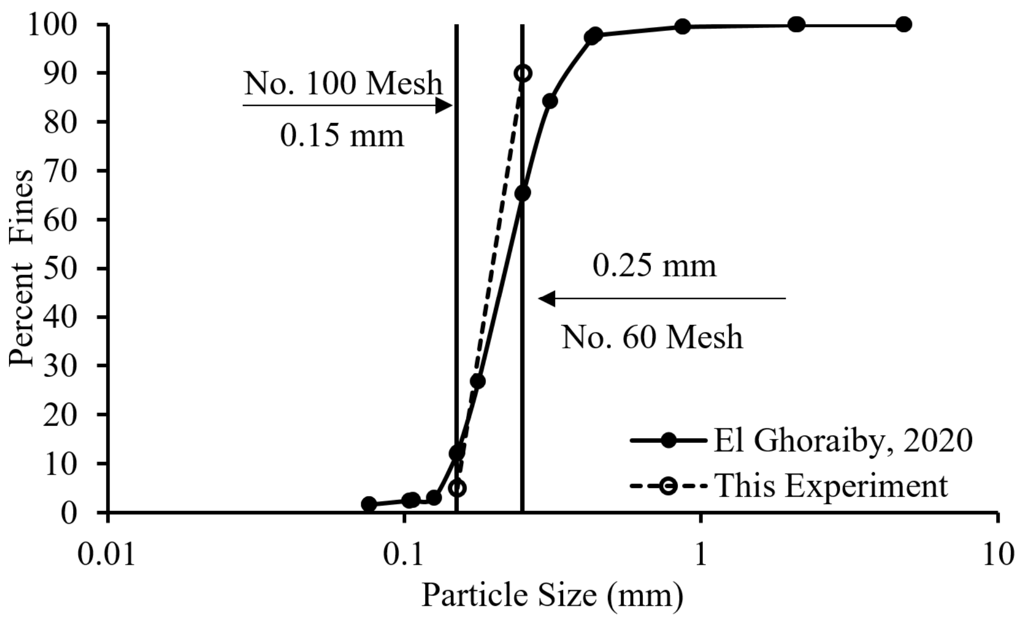

Figure 3.2 Size Distribution of Ottawa F65 Sands and Actual Distribution Range of Sand Particle Size for This Experiment Specifically

3.3 Fluid Selection and Flow Rate Design

Fluid dynamic viscosity is varied in several experiments, as it is considered as one of the important factors that affect proppant flow and transport in fractures. The following fluid viscosities are used: water with 0.001 Pa·s (1.0 cp), and glycerol-water mixes with 0.005 Pa·s (5.0 cp) and 0.01 Pa·s (10.0 cp). To make 0.005 Pa·s and 0.01 Pa·s Newtonian fluid, water is slowly mixed with glycerin. The dynamic viscosity of water-glycerin mixture is calculated by Cheng's Method (2008) using Eqns. 3.1 to 3.4, and further measured and verified in a rheometer before experiments. Equations 3.1 to 3.4 below describe the final dynamic viscosity of the mixture:

$$\mu = \mu_w^{\alpha} \cdot \mu_g^{1-\alpha} \tag{3.1}$$

$$\alpha = 1 - C_m + \frac{a \cdot b \cdot C_m \cdot (1 - C_m)}{a \cdot C_m + b \cdot (1 - C_m)} \tag{3.2}$$

$$a = 0.705 - 0.0017 \cdot T \tag{3.3}$$

$$b = (4.9 + 0.036 \cdot T) \cdot a^{2.5} \tag{3.4}$$

where, μ is the dynamic viscosity of the mixture, μ_w is the dynamic viscostiy of water, μ_g is the dynamic viscostiy of glycerin, and α is a weighting factor which is a function of the glycerin mass concentration (C_m) and the emprical coefficients *a* and *b*. To get empirical coefficients, Cheng (2008) further referred experimental results collected by Segur and Oberstar (1951), as shown in equations (3) and (4) above. Both *a* and *b* depend on temperature of the mixture. Temperature is assumed to be room temperature. A total of 21 L of mixture are required to perform a single test. Once total volume and overall mixture dynamic viscosity are known, volumes of water and pure glycerin could be back-calculated according to the the equations shown above. 11.7 L of water and 9.3 L of glycerin were used to make 0.005 Pa·s viscouse fluid. The density of final mixture is 1130 kg/m^3. 9.2 L of water and 11.8 L of glycerin were used to make 0.01 Pa·s viscous fluid and the corresponding density of final mixture is 1161 kg/m^3.

In this experiment, the fluid flow rate is primarily controlled by pump rotor frequency. Table 3.1 below shows the relationship between fluid flow rate and pump rotor frequency under each case.

Table 3.1 Pump Fluid Flow Rates

Viscosity (Pa·s)	**Volumetric Concentration (%)**	**Pump Rotor Frequency (Hz)**	**Flow Rate (L/min)**	**Flow Rate (m^3/s)**
0.001	10	10	3.90	6.5 ×10-5
0.001	10	20	4.55	7.6 ×10-5
0.001	20	10	3.30	5.5 ×10-5
0.001	20	20	3.70	6.2 ×10-5
0.005	10	10	3.35	5.6 ×10-5
0.005	10	20	3.68	6.1 ×10-5
0.005	20	10	2.55	4.3 ×10-5
0.005	20	20	3.50	5.8 ×10-5
0.010	10	10	2.50	4.2 ×10-5
0.010	10	20	3.20	5.3 ×10-5
0.010	20	10	2.65	4.4 ×10-5
0.010	20	20	3.13	5.2 ×10-5

According to equation stated in previous chapter, average particle Reynold numbers for all experiments are calculated and shown as in Table 3.2 below. To provide the spread of Reynolds number, standard deviation is also calculated. The only source that provides this spread is from particle velocities. Thus once particle velocity standard deviation is obtained, Reynolds number standard deviation could be calculated.

Table 3.2 Particle Reynolds Numbers for All Experiments, σ Stands for Standard Deviation

EXP	Fluid Density	Mean Particle Diameter	Fluid Viscosity	Mean Particle Velocity	Velocity: σ	Particle Reynolds Number	Reynolds Number: σ
	[g/cm^3]	[cm]	[g/cm·s]	[cm/s]	[cm/s]	[-]	[-]
01	1.00	0.02	0.01	7.24	2.00	14.47	4.00
02	1.00	0.02	0.01	5.26	1.18	10.52	2.37
03	1.00	0.02	0.01	4.77	2.46	9.53	4.92
04	1.00	0.02	0.01	4.55	2.49	9.09	4.98
05	1.00	0.02	0.01	7.98	3.54	15.96	7.09
06	1.00	0.02	0.01	5.97	2.79	11.93	5.59
07	1.00	0.02	0.01	9.40	2.20	18.80	4.39
08	1.00	0.02	0.01	8.80	3.25	17.61	6.50
09	1.13	0.02	0.05	1.84	0.58	0.83	0.26
10	1.13	0.02	0.05	1.38	0.72	0.63	0.32
11	1.13	0.02	0.05	2.52	0.81	1.14	0.37
12	1.13	0.02	0.05	1.55	0.60	0.70	0.27
13	1.13	0.02	0.05	1.10	0.47	0.50	0.21
14	1.13	0.02	0.05	1.33	1.14	0.60	0.51
15	1.13	0.02	0.05	1.91	1.19	0.86	0.54
16	1.13	0.02	0.05	1.46	1.27	0.66	0.57
17	1.16	0.02	0.10	1.89	0.30	0.44	0.07
18	1.16	0.02	0.10	1.50	0.33	0.35	0.08
19	1.16	0.02	0.10	2.64	0.30	0.61	0.07
20	1.16	0.02	0.10	1.89	0.28	0.44	0.06
21	1.16	0.02	0.10	1.80	0.26	0.42	0.06
22	1.16	0.02	0.10	1.35	0.25	0.31	0.06
23	1.16	0.02	0.10	2.17	0.34	0.50	0.08
24	1.16	0.02	0.10	1.54	0.24	0.36	0.06

According to the equation in previous chapter, an average particle Stokes number for all experiments are calculated and shown as in Table 3.3 below. To provide the spread of Stokes number, standard deviation is also calculated. The only source that provides this spread is from particle velocities, same as Reynolds number case. Thus once particle velocity standard deviation is obtained, Stokes number standard deviation could be calculated.

Table 3.3 Particle Stokes Numbers for All Experiments, σ Stands for Standard Deviation

EXP	Fluid Density [g/cm³]	Mean Particle Diameter [cm]	Particle Density [g/cm³]	Fracture Aperture [cm]	Fluid Viscosity [g/cm·s]	Mean Particle Velocity [cm/s]	Velocity: σ [cm/s]	Particle Stokes Number [-]	Stokes Number: σ [-]
01	1.00	0.02	2.65	0.60	0.01	2.27	1.23	0.0223	0.0120
02	1.00	0.02	2.65	0.60	0.01	1.11	0.40	0.0109	0.0039
03	1.00	0.02	2.65	0.60	0.01	1.39	1.09	0.0136	0.0107
04	1.00	0.02	2.65	0.60	0.01	1.57	0.90	0.0155	0.0088
05	1.00	0.02	2.65	0.60	0.01	1.51	1.19	0.0148	0.0117
06	1.00	0.02	2.65	0.60	0.01	1.32	1.04	0.0129	0.0102
07	1.00	0.02	2.65	0.60	0.01	2.26	0.91	0.0222	0.0089
08	1.00	0.02	2.65	0.60	0.01	1.36	1.09	0.0133	0.0107
09	1.13	0.02	2.65	0.60	0.05	0.20	0.25	0.0004	0.0005
10	1.13	0.02	2.65	0.60	0.05	0.07	0.27	0.0001	0.0005
11	1.13	0.02	2.65	0.60	0.05	0.18	0.30	0.0004	0.0006
12	1.13	0.02	2.65	0.60	0.05	0.10	0.29	0.0002	0.0006
13	1.13	0.02	2.65	0.60	0.05	0.09	0.22	0.0002	0.0004
14	1.13	0.02	2.65	0.60	0.05	0.10	0.29	0.0002	0.0006
15	1.13	0.02	2.65	0.60	0.05	0.02	0.32	0.0000	0.0006
16	1.13	0.02	2.65	0.60	0.05	0.17	0.38	0.0003	0.0007
17	1.16	0.02	2.65	0.60	0.10	0.07	0.21	0.0001	0.0002
18	1.16	0.02	2.65	0.60	0.10	0.09	0.19	0.0001	0.0002
19	1.16	0.02	2.65	0.60	0.10	0.14	0.20	0.0001	0.0002
20	1.16	0.02	2.65	0.60	0.10	0.13	0.22	0.0001	0.0002
21	1.16	0.02	2.65	0.60	0.10	0.18	0.19	0.0002	0.0002
22	1.16	0.02	2.65	0.60	0.10	0.12	0.20	0.0001	0.0002
23	1.16	0.02	2.65	0.60	0.10	0.06	0.23	0.0001	0.0002
24	1.16	0.02	2.65	0.60	0.10	0.16	0.24	0.0002	0.0002

3.4 Fracture Design

Two fractures are designed for the experiment. Figures 3.3a to 3.3f show the three views of fractures with intersecting angles at 30° and 45°, inspired by observations from Frash et al. (2019), Pan et al. (2018), and Li et al. (2016). The entire fracture system includes five parts: entrance funnel, entrance fracture, middle fracture, exit fracture, and exit funnel. Intersection angle is defined as the angle between the direction of fluid flow in entrance/exit fracture and the direction of fluid flow in middle fracture. The exit and entrance funnels have a slope of 5°. The entrance, middle, and exit fracture are 203mm high and 6 mm wide.

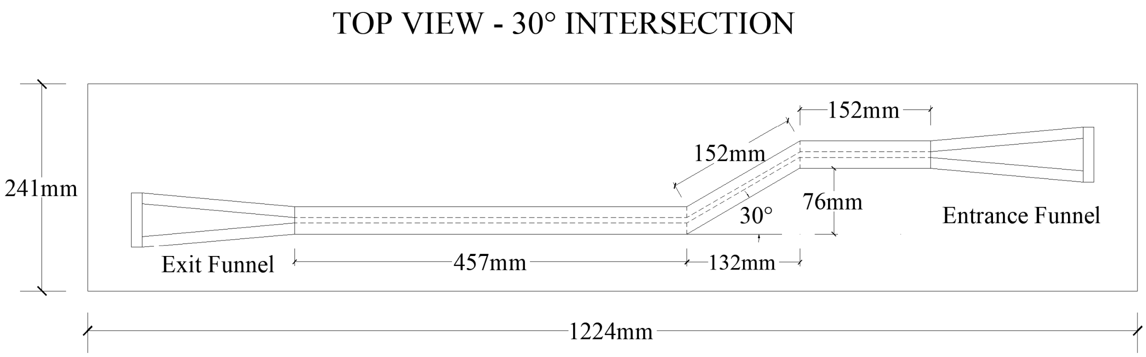

Figure 3.3a Plexiglass Fractures Top View for 30° Intersecting Angle

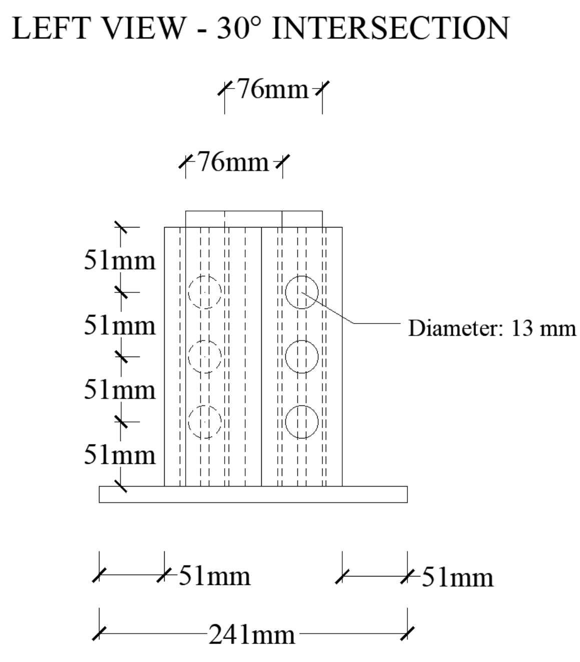

Figure 3.3b Plexiglass Fractures Left View for 30° Intersecting Angle

FRONT VIEW - 30° INTERSECTION

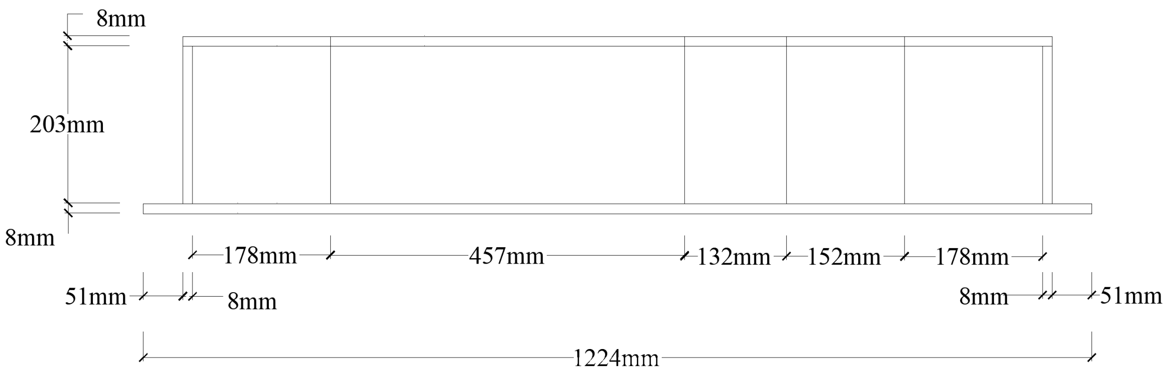

Figure 3.3c Plexiglass Fractures Front View for 30° Intersecting Angle

TOP VIEW - 45° INTERSECTION

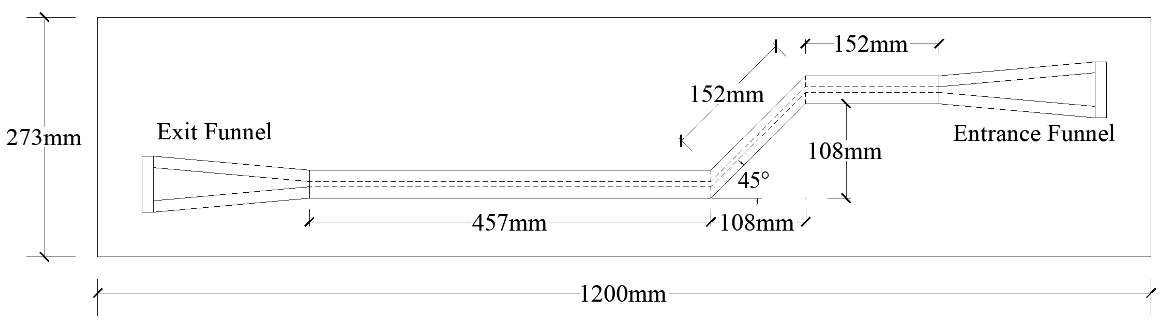

Figure 3.3d Plexiglass Fractures Top View for 45° Intersecting Angle

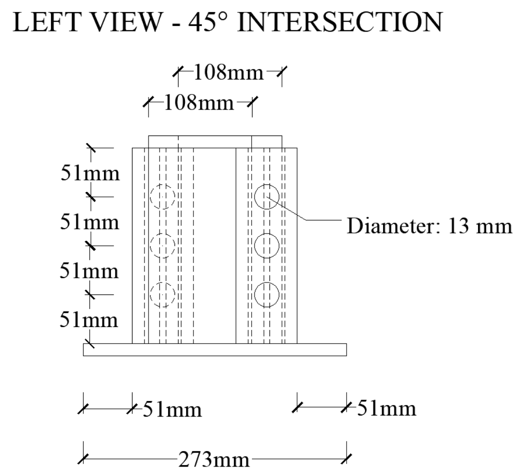

Figure 3.3e Plexiglass Fractures Left View for 45° Intersecting Angle

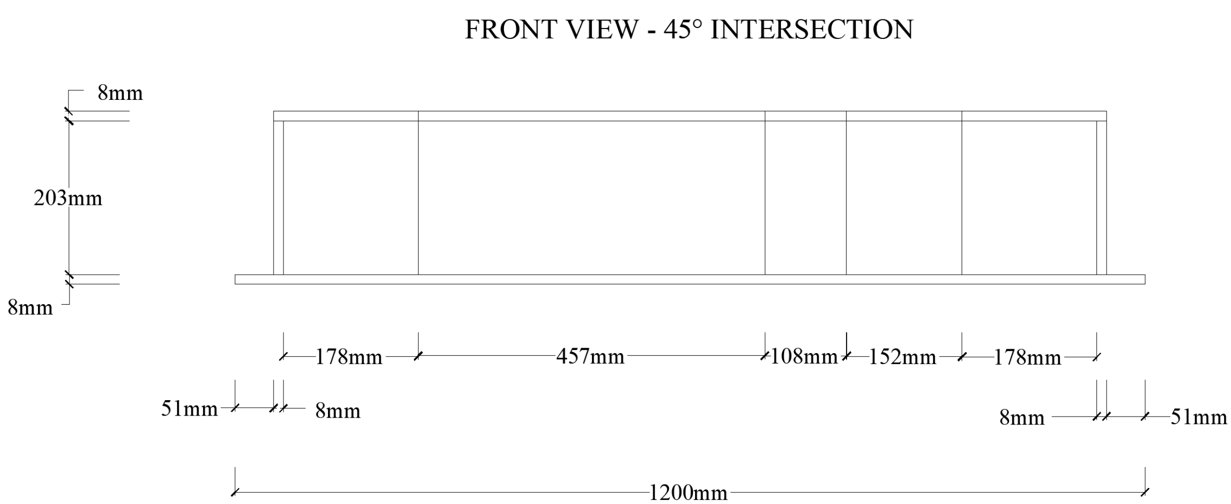

Figure 3.3f Plexiglass Fractures Front View for 45° Intersecting Angle

Figure 3.4 shows the physical appearance of the 30° designed fracture. Most of the acrylic plates are completely glued with each other, except the removable top covers of entrance and exit funnels. Rubber bands are used for sealing. There are three holes on each side of the fracture. Fluids were injected into the middle level and expelled from the upper level.

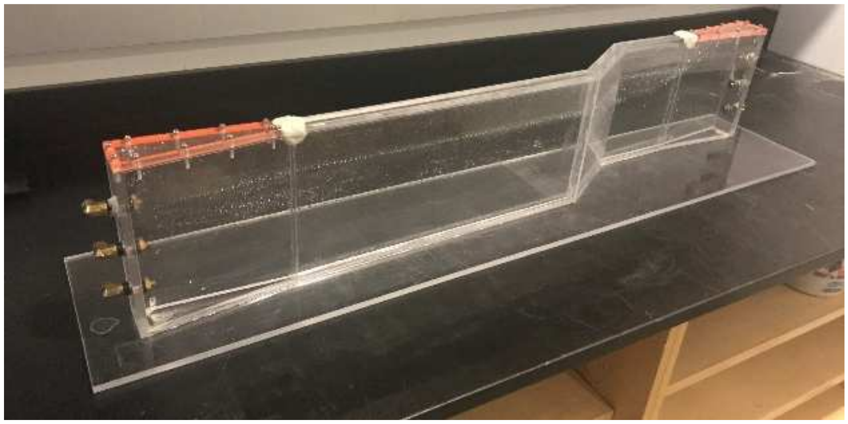

Figure 3.4 Physical Appearance of the Designed Fracture

3.5 Camera and Video Quality

Three cameras are used to record each test. A SONY DSC-RX10M3 Digital Still Camera is used to record particle flow process in entrance funnel and entrance fracture part of the fracture system. Videos were shot at 1920x1080 60 FPS. A Nikon D160 Digital Camera was used to record particle flow process in entire exit fracture part of the fracture system. Videos were shot at 1280x720 60 FPS. A third High-Speed Phantom C320 Camera was used to record first half of the exit fracture part and further analyzed by GeoPIV Method. All videos were shot 1280x1024 900 FPS.

3.6 System Setup

The sand and fluid are continuously mixed in a bucket at the very top using electrical mixer at sufficiently high rate to keep proppant particles suspended in fluid. Then, the slurry is pumped and injected into the fracture from the mid-level hole of the entrance funnel. All exiting fluids are collected into the bucket on the table from the top-level hole of the exit funnel. To better record the sand flow in the fracture, black background paper is put on the back of the fracture, from the entrance part to middle and exit part, not including the funnels. Cameras are placed in front of the fracture. To get the best video quality, the distance between the camera lenses and the fracture face is generally around 140 cm. Figures 3.5 and 3.6 show the profile and plan view of the experimental setup respectively. Figure 3.7 shows the configuration of the entire experiment system.

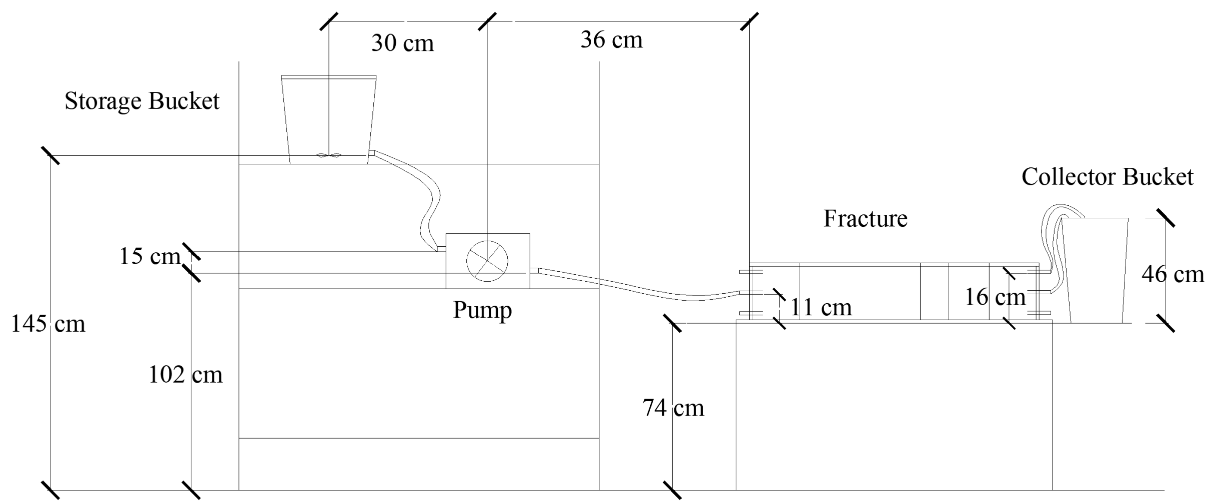

Figure 3.5 Experimental Setup Schematic, Profile View

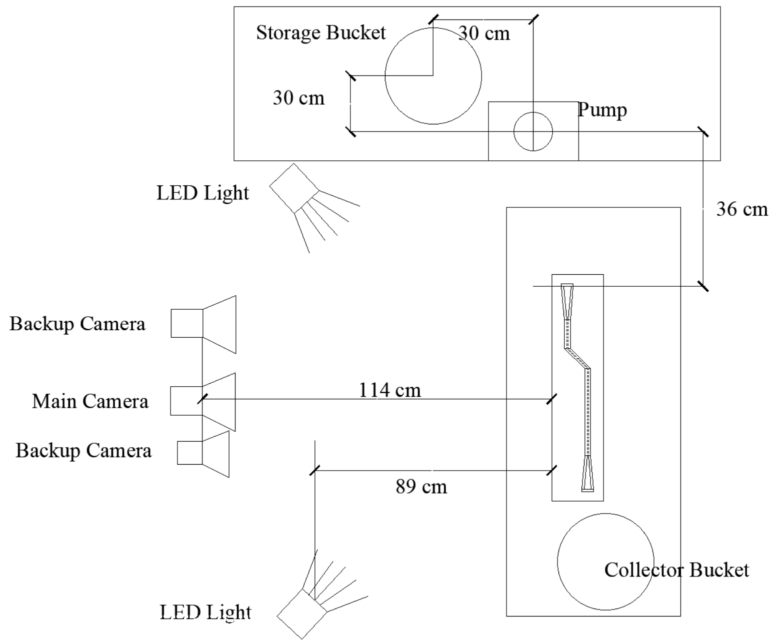

Figure 3.6 Experimental Setup Schematic, Plan View

Figure 3.7 Physical Configuration of the Experiment System

3.7 Experiment Schedule

Beside the main investigation parameter of fracture intersection angle, the experiments also consider the following factors: fluid viscosity, volumetric concentration of sand, and fluid flow rate. Table 3.4 below shows all tests conducted in terms of combinations of different factors. Fluid flow rate is a function of pump rotor frequency, fluid viscosity and volumetric concentration of sand, obtained by during pump calibrations.

Table 3.4 Experimental Cases

Test	Fluid Viscosity (Pa-s)	Volumetric Concentration of Sand (%)	Pump Rotor Frequency (Hz)	Fluid Flow Rate (L/min)	Fracture Intersection Angle
1	0.001	10	10	3.90	30
2	0.001	10	10	3.90	45
3	0.001	10	20	4.55	30
4	0.001	10	20	4.55	45
5	0.001	20	10	3.30	30
6	0.001	20	10	3.30	45
7	0.001	20	20	3.70	30
8	0.001	20	20	3.70	45
9	0.005	10	10	3.35	30
10	0.005	10	10	3.35	45
11	0.005	10	20	3.68	30
12	0.005	10	20	3.68	45
13	0.005	20	10	2.55	30
14	0.005	20	10	2.55	45
15	0.005	20	20	3.50	30
16	0.005	20	20	3.50	45
17	0.010	10	10	2.50	30
18	0.010	10	10	2.50	45
19	0.010	10	20	3.20	30
20	0.010	10	20	3.20	45
21	0.010	20	10	2.65	30
22	0.010	20	10	2.65	45
23	0.010	20	20	3.13	30
24	0.010	20	20	3.13	45

3.8 Video Footage Analysis

Advanced Particle Image Velocimetry (PIV) method, adopted for studying particulate materials, is used to analyze the videos recorded by Phantom Camera. The main software is GeoPIV-RG, a Matlab module developed by Stanier et al. (2015), previously called GeoPIV by White and Take (2002). Figure 3.8 below describes the GeoPIV-RG flow chart. Before launching the main process code, it is required to select and decide the frames/pictures to be analyzed, to choose the corresponding regions of interest, and to decide the size and spacing of meshes. The main code tracks particle movements among images by comparing the reference and subsequent images at the point in time of interest. The leapfrog method (diagram shown in Figure 3.9) retains the initial image as a reference image after every computation, which is suggested if there is no control point in the experiment. However, if too many wild results occur, GeoPIV-RG uses a sequential scheme (diagram shown in Figure 3.10), which updates reference images after every computation. GeoPIV-RG generates displacement vector field and displacement contours for selected region of interest and the output has a unit of pixels per frame. Since the scientific cameras secure a high-precision relationship between video/image pixels and length, as well as the relationship between time and frame recording rate, a velocity field is obtained by conversion from the displacement.

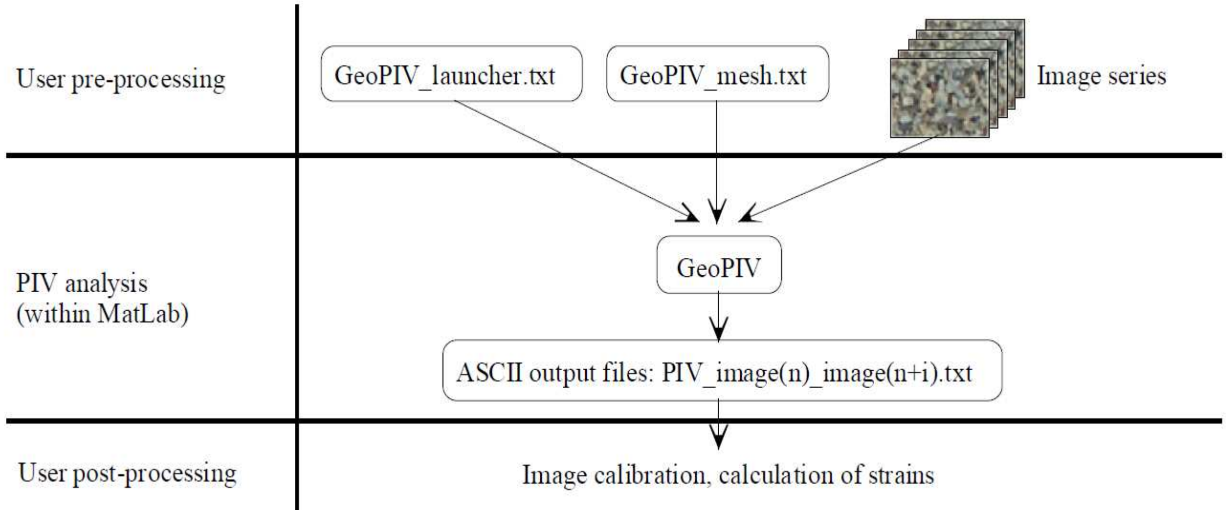

Figure 3.8 Flow chart of GeoPIV-RG software (White and Take, 2002)

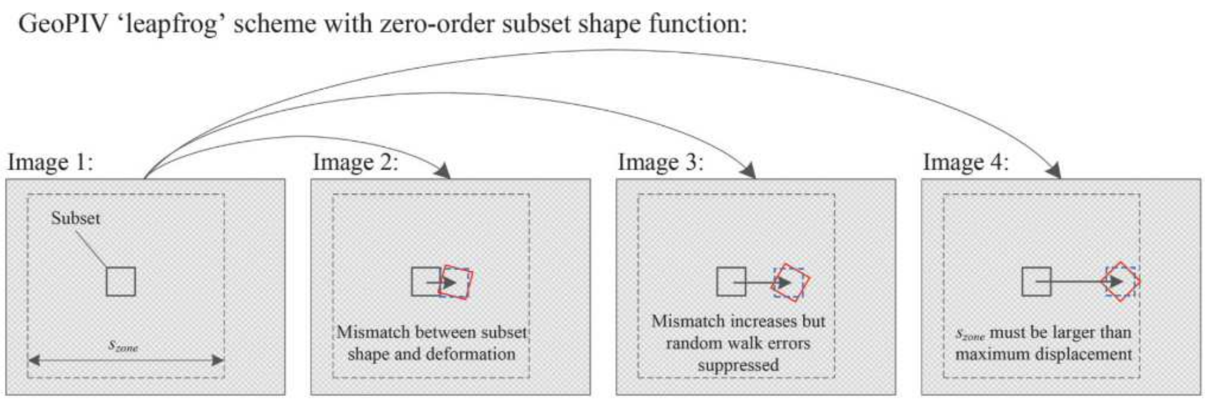

Figure 3.9 Diagram of Leapfrog Schematic (Stanier et al., 2015)

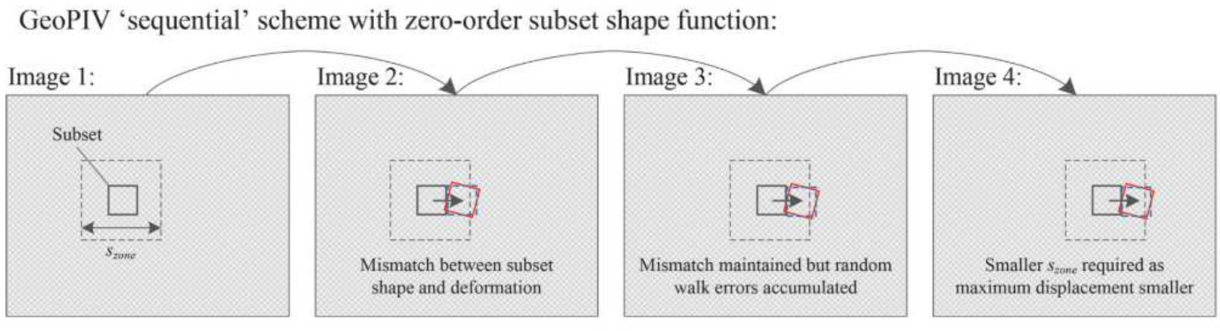

Figure 3.10 Diagram of Sequential Schematic (Stanier et al., 2015)

3.9 Accuracy and Error

Sources of errors in the GeoPIV-RG analysis can originate from the camera performance, image and video setups, lighting environments, the experiment components setup and the GeoPIV-RG software post-processing. In our experiments, the Phantom camera recorded high-resolution high-frame-rate videos. Two LED lights with 12,000 lumens were placed on both sides of the experiment to enhance lighting conditions and to minimize shadows. To avoid image distortions, the camera lens was set to be in same level and perpendicular to fracture face, and the camera's position was secured with a tripod. Therefore, the GeoPIV-RG analysis remains the major uncertainty source in the experiments. To conclude, a good understanding and use of the GeoPIV-RG analysis will largely ensure the accuracy of results.

The input parameters causing errors of GeoPIV-RG software depend on image quality, lighting changes, image-particle diameter, spatial variation, recording angles and mesh sizes (White and Take, 2002; Stanier et al., 2015; Luo and Tomac, 2018b; Fjaestad and Tomac, 2019). Given experiment conditions stated previously, all hardware-related input parameters, except the mesh sizes, have been controlled by fixing position and ensuring accuracy. It has been previously found that smaller mesh sizes will provide more local information while larger mesh size will provide better precision (Stanier et al., 2015; Luo and Tomac, 2018b; Fjaestad and Tomac, 2019). To verify what mesh size will be the best for our experiment analysis, four different sizes were analyzed: 10×10, 20×20, 30×30, and 40×40 pixels. In addition, two neighboring area with similar velocities were also selected for comparison. Different combinations are shown in Table 3.5. Mean velocities of each region and mesh size were computed, as highlighted in yellow color in Table 3.5. Tables 3.6 and 3.7 summarized the results for accuracy analysis for GeoPIV software. For both selected regions, the percent difference of results between 10-pixel and 20-pixel mesh are above 10%. However, for both regions, the percent difference for results between 20-pixel and 30-pixel mesh, and 30-pixel and 40-pixel mesh are less than 2%. This indicates that 20-pixel mesh and above will provide more consistent results for the range of experimental conditions in this research. When viewing 10-pixel mesh only, the percent differences between two regions is above 10%. For mesh sizes with 20-pixel and above, the percent differences between two regions is less than 5%. This is another indicator which suggests 20-pixels and above provide more accurate result. It is important to remember that local details were observed during the error analysis.

Table 3.5 Accuracy Analysis: Combined Cases with Respect to Mesh Size and Mesh Location

<table>
<tr><th></th><th>Region Left</th><th></th><th>Region Right</th><th></th></tr>
<tr><td>10 × 10</td><td>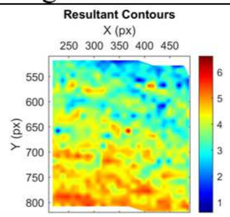
</td><td>Max:
13.59
Mean:
8.08
Middle Range:
6.87-9.42</td><td>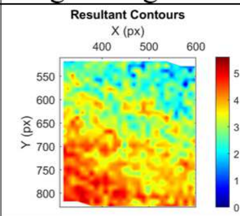
</td><td>Max:
11.68
Mean:
7.06
Middle Range:
5.92-8.34</td></tr>
<tr><td>20 × 20</td><td>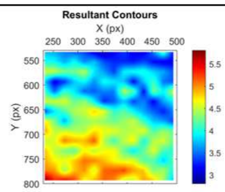
</td><td>Max:
12.49
Mean:
9.26
Middle Range:
8.30-10.16</td><td>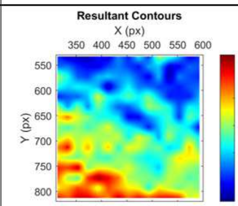
</td><td>Max:
12.08
Mean:
8.93
Middle Range:
7.98-9.64</td></tr>
<tr><td>30 × 30</td><td>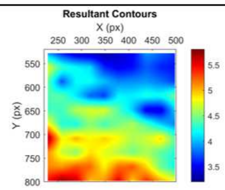
</td><td>Max:
12.01
Mean:
9.15
Middle Range:
8.14-10.07</td><td>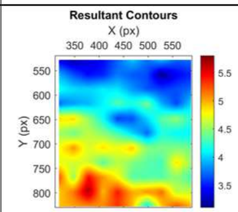
</td><td>Max:
11.92
Mean:
9.00
Middle Range:
8.00-9.94</td></tr>
<tr><td>40 × 40</td><td>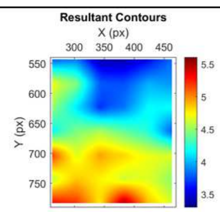
</td><td>Max:
11.53
Mean:
9.12
Middle Range:
8.04-9.83</td><td>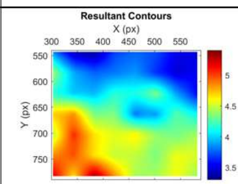
</td><td>Max:
11.13
Mean:
8.83
Middle Range:
7.97-9.52</td></tr>
</table>

Table 3.6 Accuracy Analysis: Results for Mesh Sizes

	Region Left	Region Right
10 × 10 vs. 20 × 20	Δ = 1.18 (14.6% wrt10)(12.7% wrt20)	Δ = 1.87 (26.5% wrt10)(20.9% wrt20)
20 × 20 vs. 30 × 30	Δ = 0.11 (1.2% wrt20)(1.2% wrt30)	Δ = 0.07 (0.8% wrt20)(0.8% wrt30)
30 × 30 vs. 40 × 40	Δ = 0.03 (0.3% wrt30)(0.3% wrt40)	Δ = 0.17 (1.9% wrt30)(1.9% wrt40)

Table 3.7 Accuracy Analysis: Results for Mesh Location

	(Left – Right) / Left
10 × 10	12.6%
20 × 20	3.6%
30 × 30	1.6%
40 × 40	3.2%

CHAPTER 4 RESULTS AND ANALYSIS

4.1 General Description

This section describes the visual inspections of proppant settlements, displacement and velocities from GeoPIV analysis. Then, direct and processed PIV results will be shown after direct observations. In addition, a correlation between proppant settlement and proppant velocities is investigated considering effects of fracture intersection angles, proppant volumetric concentration, carrying flow rate and dynamic viscosities.

4.2 Visual Observations of All Experiments

4.2.1 For 0.001 Pa·s Viscosity

In 0.001 Pa·s fluid, the 45° intersecting fracture has a steeper and more various overall dune shape than a 30° fracture for all of the observed particle concentrations and flow rates in Experiments 01 to 08, as shown in Figures 4.2a and 4.2b. For example, the 45° fracture dune angles are measured between 9.6° and 16°; while for 30° fracture, the dune angles are between 6.8° and 9° from horizontal as in Figure 4.1. The slope steepness and variety are more clearly observed further down the fracture, in the middle and exit branches. Additionally, the 45° intersecting fracture has a more convex curved slope (see all exit branches in Figure 4.2a and Figure 4.2b), which indicates a more rapid settlement right after exiting the intersected fractures, while the 30° intersecting fracture causes a flatter slope. Specifically, 45° intersection fracture causes a small localized 'hump' just at the beginning part of the exit branch for a high volumetric concentration of sands, as shown in circled parts in Figure 4.3.

While maintaining at 10% volumetric proppant concentration in the slurry (experiments 01-04), intersecting angle effect on dune shape angle is slightly less significant than that caused by flow rate. For example, the slope angles are 8.5° and 6.8° for 30° intersecting fractures, 11° and 9.6° for 45° intersecting fractures. The differences in the dune angle are 2.5° and 2.8° for low and high flow rate cases. As sand volumetric concentration maintains at 20% (experiments 05-08), the intersection angle starts dominating the shape formation of the dune slope. The differences in dune angles are 4° and 7° for low and high flow rate cases.

At both lower flow rate in the slurry (experiments 01, 02, 05, 06) and higher flow rate in the slurry (experiments 03, 04, 07, 08), higher proppant volumetric concentration will help to create a more sloped settlement but not very significantly, especially for the middle branch. As flow rate increases, the significance of the combined effect of the volumetric proppant concentration and the intersection angle ramps up producing increasingly steep dune angles. For lower flow rate conditions, the differences in settlement slopes (30° vs. 45° intersection angle) are 2.5° and 5°. For higher flow rate conditions, the differences in dune slope are 2.2° and 7°.

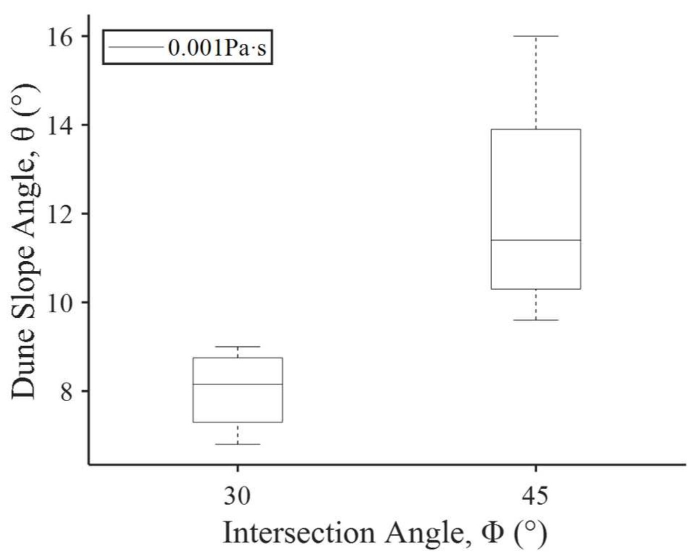

Figure 4.1 Effect of Intersection Angle on Dune Slope for 0.001 Pa·s

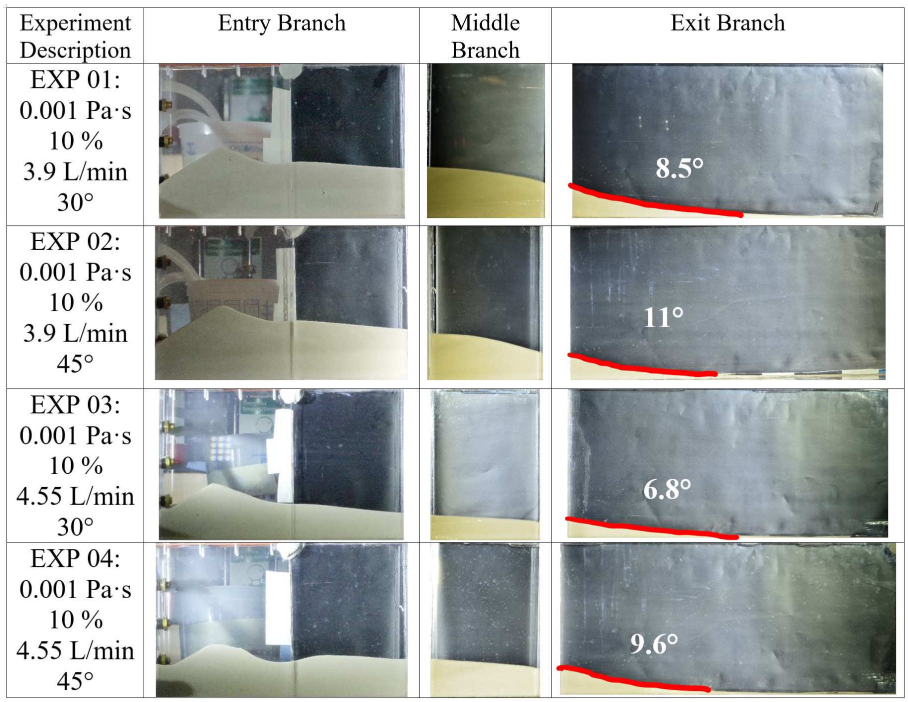

Figure 4.2a Exit Branch Dune Slope Observations for 0.001 Pa·s

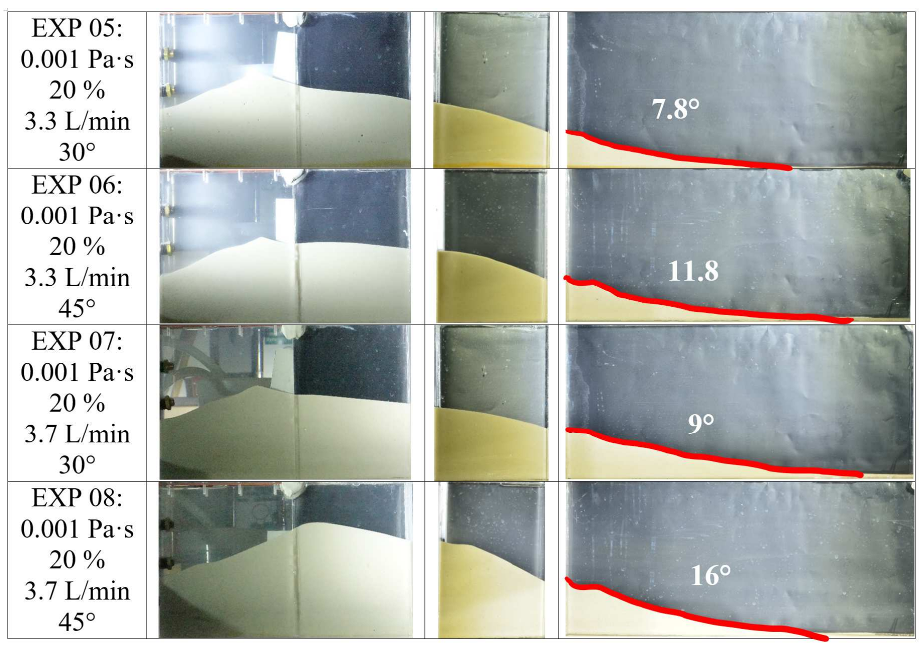

Figure 4.2b Exit Branch Dune Slope Observations for 0.001 Pa·s, continued

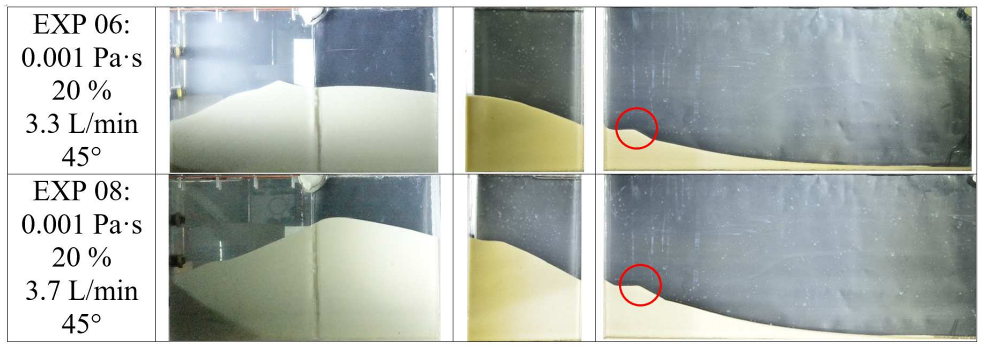

Figure 4.3 Exit Branch Dune with Localized Hump for Experiments 06 and 08

4.2.2 For 0.005 Pa·s Viscosity

In general, for all 0.005 Pa·s carrying fluid experiments for all flow rates and proppant volumetric concentrations (experiments 09-16), 45° intersecting fractures also have a slightly steeper settlement slope as shown in Figure 4.5a and 4.5b, compared with 30° intersecting fractures. For example, the 45° fracture dune angles are measured between 6° and 7.5°; while for 30° fracture, the dune angles are between 5° and 7° from horizontal as in Figure 4.4. However, this effect is not as significant as in pure water condition, 0.001 Pa·s carrying fluid (comparing Figure 4.2a vs. Figure 4.5a, or Figure 4.2b vs. Figure 4.5b), confirming that the increase of carrying fluid dynamic viscosity contributes to better flow and transport. As shown in Figures 4.5a and 4.5b, even though the tests have stopped for a while, there are still sands flowing in the fluid.

For both 10% (experiments 09-12) and 20% proppant volumetric concentrations (experiments 13-16), the role of flow rate is not as strong as that of intersecting angle, which dominates the formation of the dune slope. At low proppant volumetric concentrations, the dune slope difference is 1° for a lower flow rate and 0° for a higher flow rate. At high proppant volumetric concentrations, the dune slope difference is 2° for a lower flow rate and 0.5° for a higher flow rate.

For both low (experiments 09, 10, 13, 14) and high (experiments 11, 12, 15, 16) flow rate conditions, higher proppant volumetric concentrations help to shape a slightly steeper dune, combined with the effect of intersecting angle. Under low flow rate conditions, the dune angle difference is 1° for lower sand ratio and 2° for higher sand ratio. As for the high flow rate cases, the dune angle difference is 0° for lower sand ratio and 0.5° for higher sand ratio. Higher proppant volumetric concentration also helps to create a more various settlement shapes in the entrance branch (see Figures 9a and 9b). The sand dune is flat in the entrance and middle branches for lower sand ratio conditions.

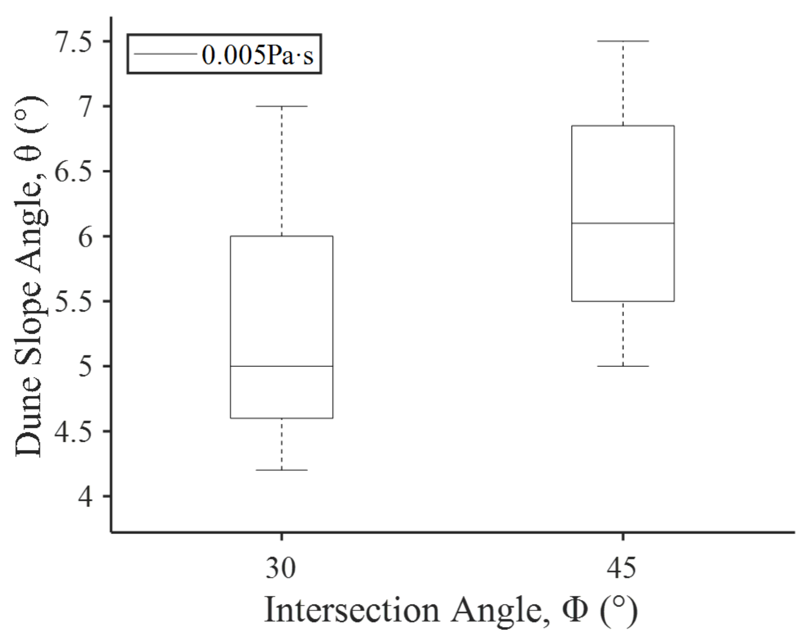

Figure 4.4 Effect of Intersection Angle on Dune Slope for 0.005 Pa·s

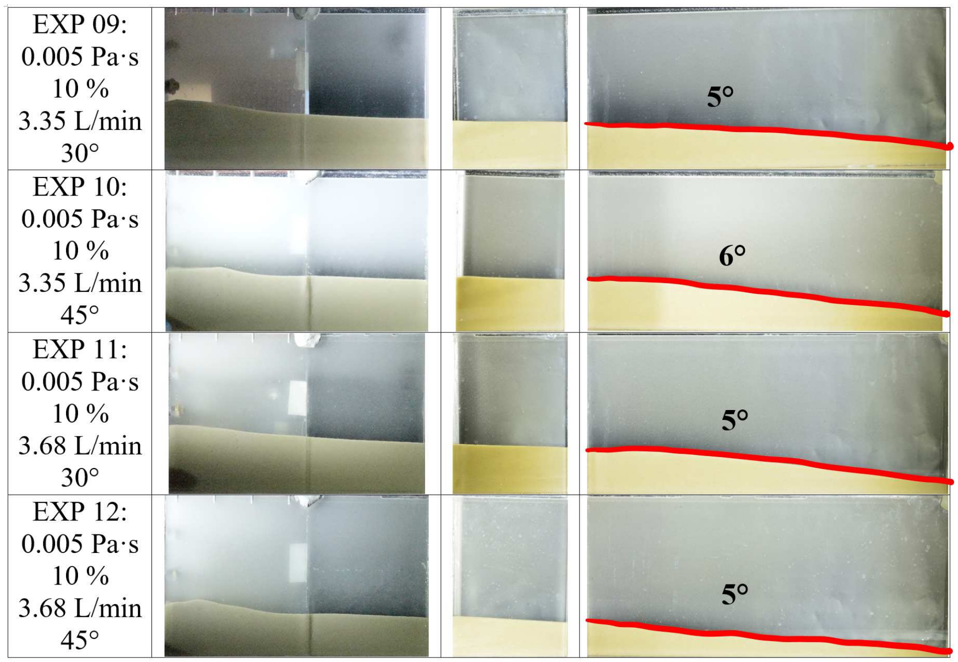

Figure 4.5a Exit Branch Dune Slope Observations for 0.005 Pa·s

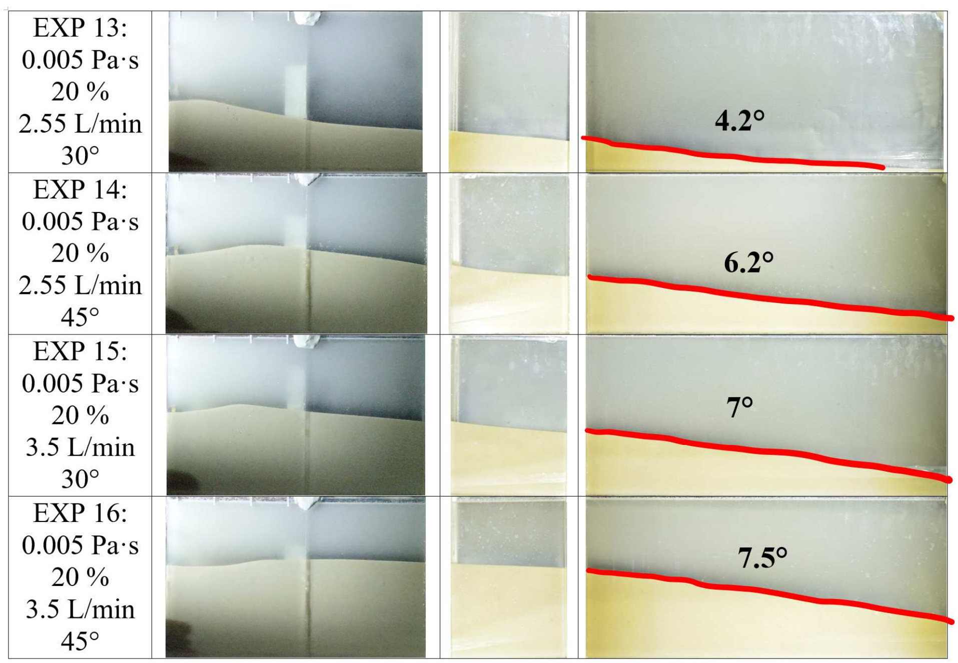

Figure 4.5b Exit Branch Dune Slope Observations for 0.005 Pa·s, continued

4.2.3 For 0.01 Pa·s Viscosity

Results under 0.01 Pa·s carrying fluid (experiments 17-24) are alike that of 0.005 Pa·s carrying fluid. General settlement slope shape characterizations are all preserved while considering the effect of sand ratio, flow rate, and most importantly intersecting angles. The only major difference is that the slopes of all 8 cases are further flattened, as shown in Figures 4.7a and 4.7b. The 45° fracture dune angles are measured between 1.2° and 3.1°; while for 30° fracture, the dune angles are between 0.3° and 1.3° from horizontal as in Figure 4.6.

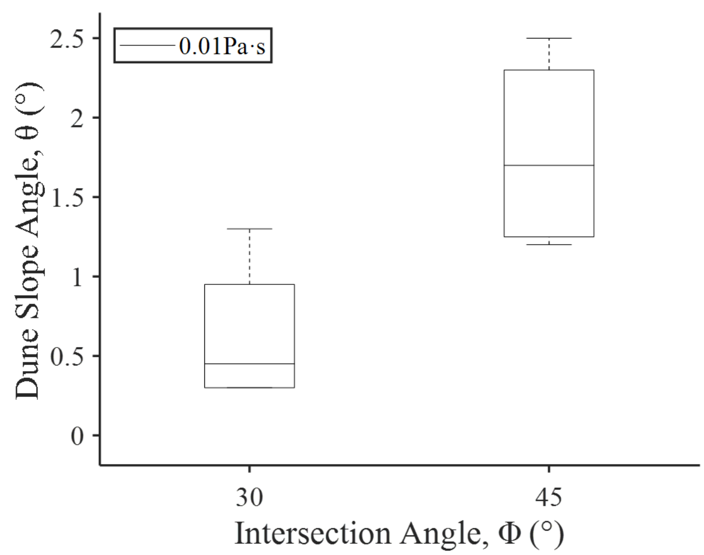

Figure 4.6 Effect of Intersection Angle on Dune Slope for 0.01 Pa·s

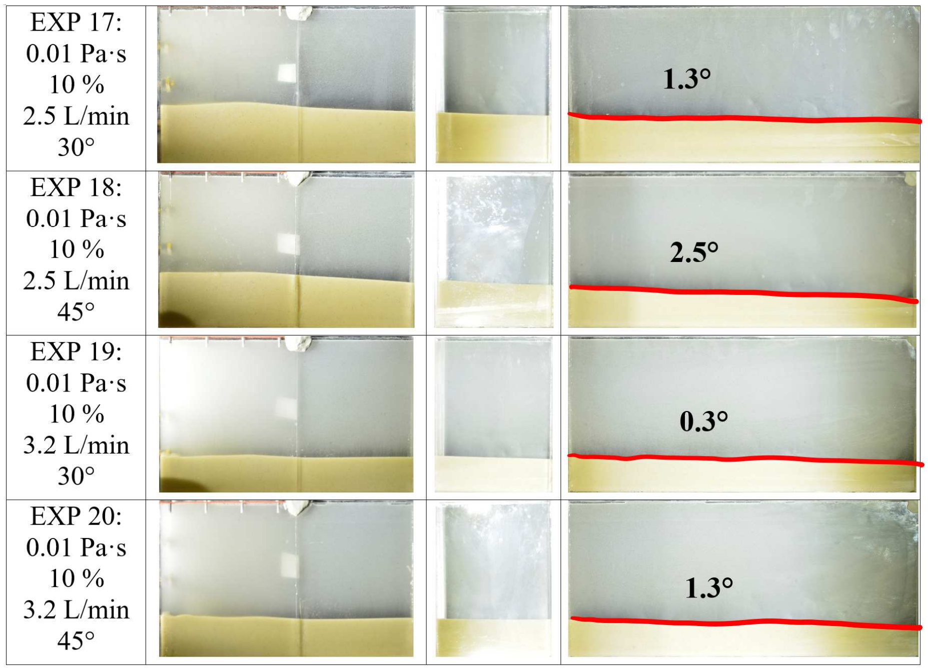

Figure 4.7a Exit Branch Dune Slope Observations for 0.01 Pa·s

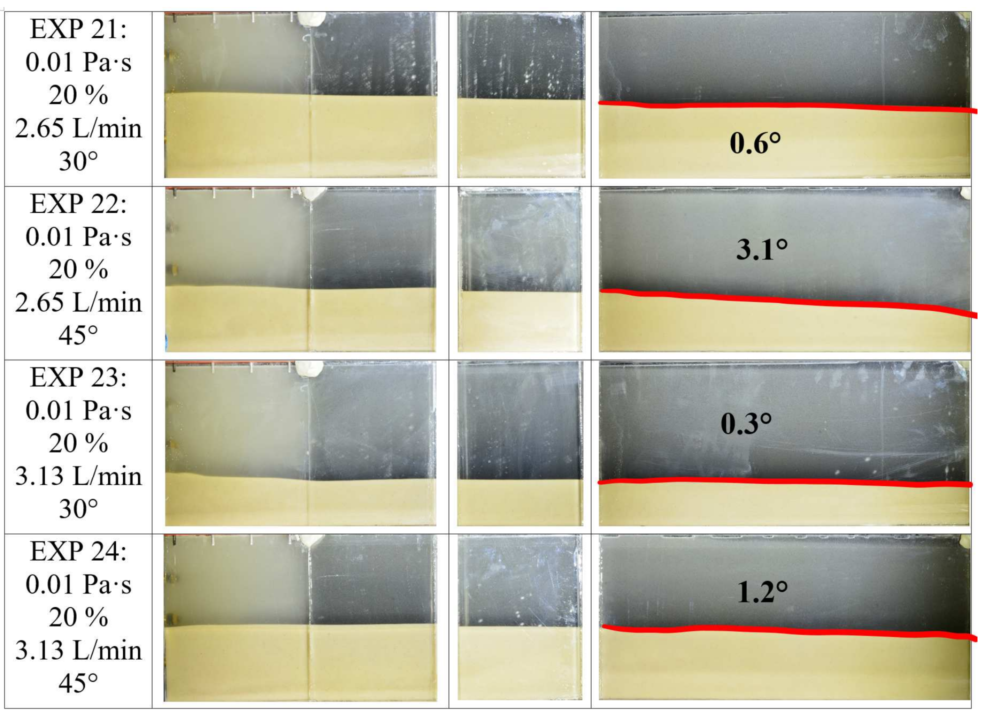

Figure 4.7b Exit Branch Dune Slope Observations for 0.01 Pa·s, continued

4.2.4 General Comparison

While ignoring all other factors, an increase in carrying fluid dynamic viscosity progressively flattens the dune in the exit branch, increases the horizontal sand transport, improves proppant transport efficiency, and reduces gravity effects as shown in Figure 4.11. The multiphase flow remains conserved from the injection point to the collection point, and sand particles remained floating after pumping stops. If considering effect of intersection angle only as shown in Figure 4.8, ignoring all other factors, 45° intersection angle generally provides wider range of proppant settlement slope angle. If considering effect of proppant concentration only (Figure 4.9) or fluid flow rate (Figure 4.10), those effects has a relatively weak effect on dune slope comparing with other factors.

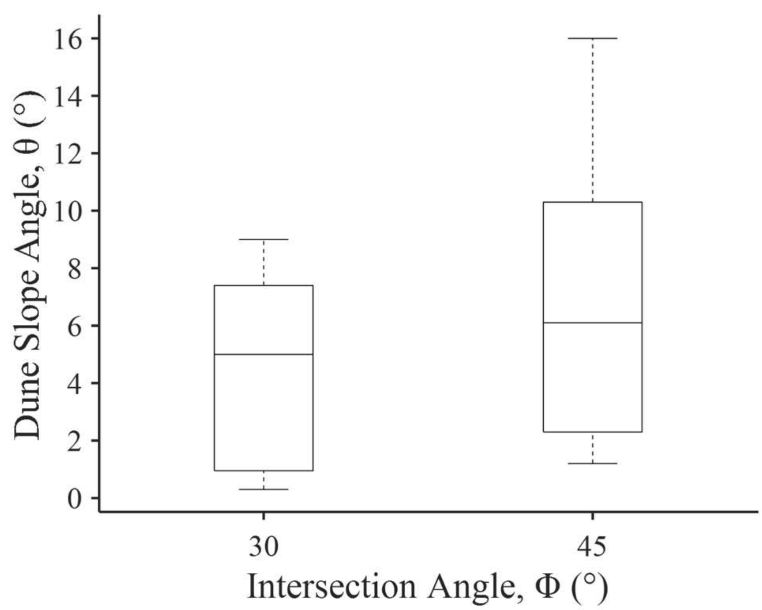

Figure 4.8 Effect of Intersection Angles on Dune Slope for All Experiments

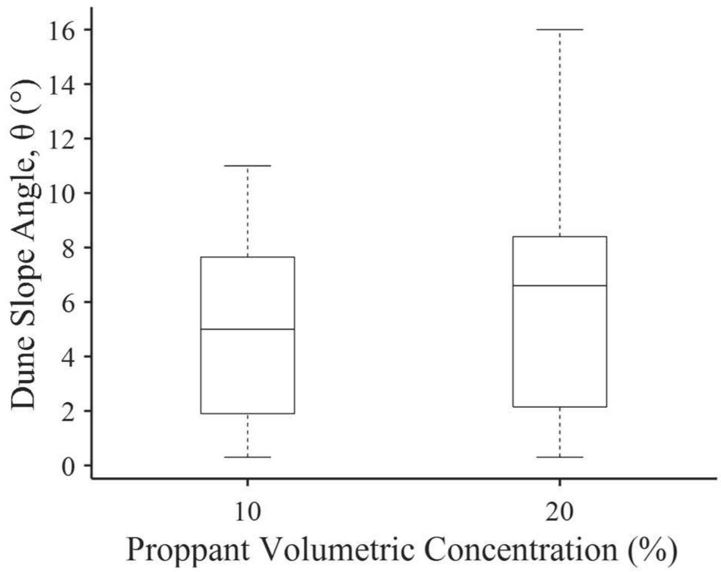

Figure 4.9 Effect of Proppant Volumetric Concentration on Dune Slope for All Experiments

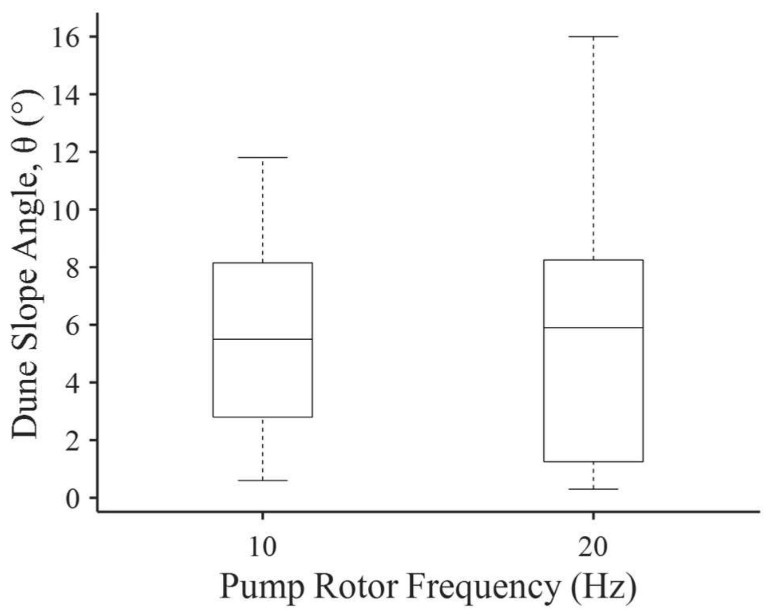

Figure 4.10 Effect of Fluid Flow Rate Controlled by Pump Rotor Frequency on Dune Slop for All Experiments

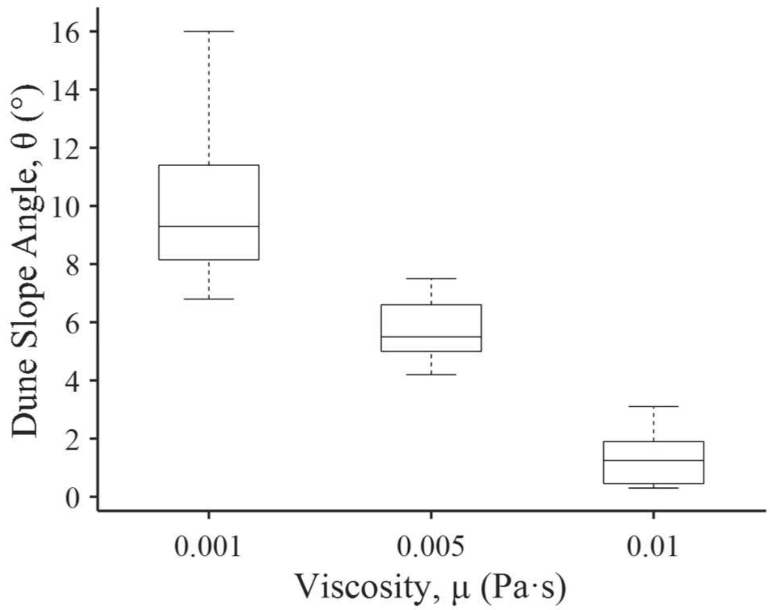

Figure 4.11 Effect of Fluid Viscosities on Dune Slope for All Experiments

4.2.5 Particle Agglomeration

Particle agglomerations are generally very hard to observe by eyes, especially for this current set of experiments with fine sands. Following figures show particle agglomeration shapes for selected experiments which have the most obvious possible agglomerations from snap shots. Different from table shown previously, which was visual observation of dynamic media, this section has slightly fewer results.

There are generally three categories observed. In the first type, only clear clusters are observed (see Figures 4.12a to 4.12c below). In the second type, only layers are observed while clusters are extremely hard to see (see Figure 4.13 below). In the last type, both particle clusters and layers are observed clearly (see Figures 4.14a to 4.14i). Highlighted regions for particle clusters are shown in red and highlighted regions for layer boundaries are shown in blue.

There are several different shapes observed. Nearly round and slightly eclipse are the most frequently observed shapes. New moon shape is observed in EXP 16, 21. Long eclipse shape is observed in EXP 06, 07, 19. Inverted water drop shape is observed in EXP 15. Nearly rhombus shape is observed in EXP 18. Under low viscosity condition, parallel lines pattern was observed in the end.

Figure 4.12a Type A of Particle Agglomerations: Clusters-Only for Experiment 06

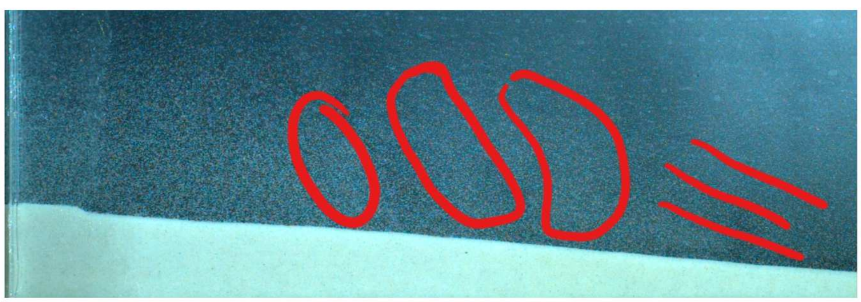

Figure 4.12b Type A of Particle Agglomerations: Clusters-Only for Experiment 07

Figure 4.12c Type A of Particle Agglomerations: Clusters-Only for Experiment 08

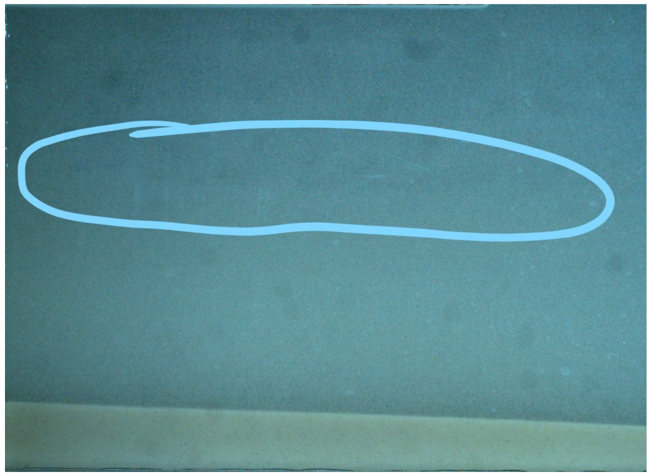

Figure 4.13 Type B of Particle Agglomeration: Layers-Only for Experiment 14

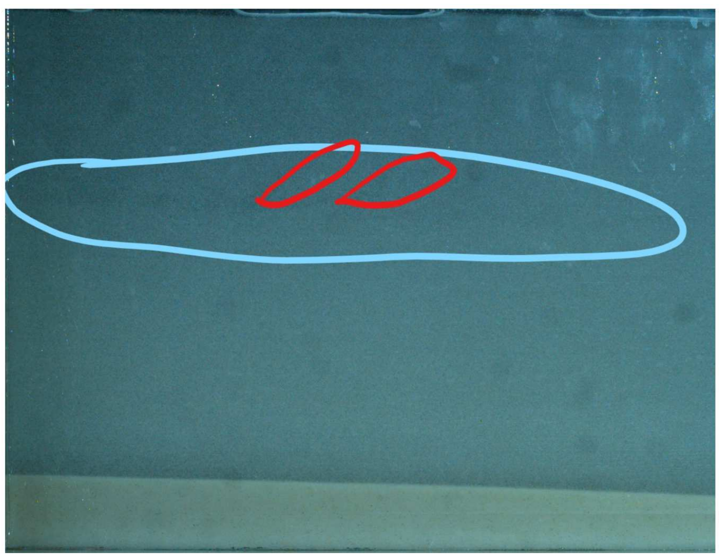

Figure 4.14a Type C of Particle Agglomeration: Clusters and Layers Combined for Experiment 15

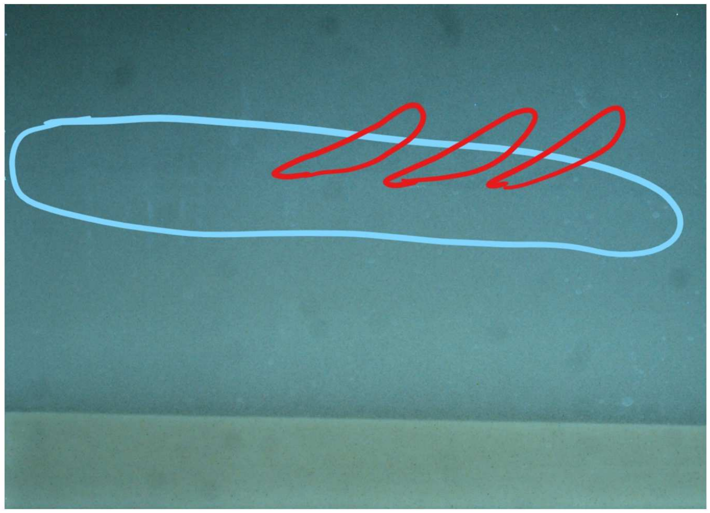

Figure 4.14b Type C of Particle Agglomeration: Clusters and Layers Combined for Experiment 16

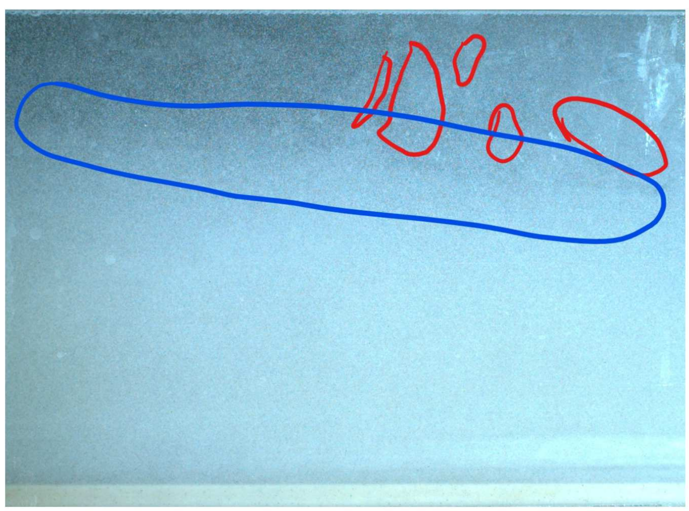

Figure 4.14c Type C of Particle Agglomeration: Clusters and Layers Combined for Experiment 17

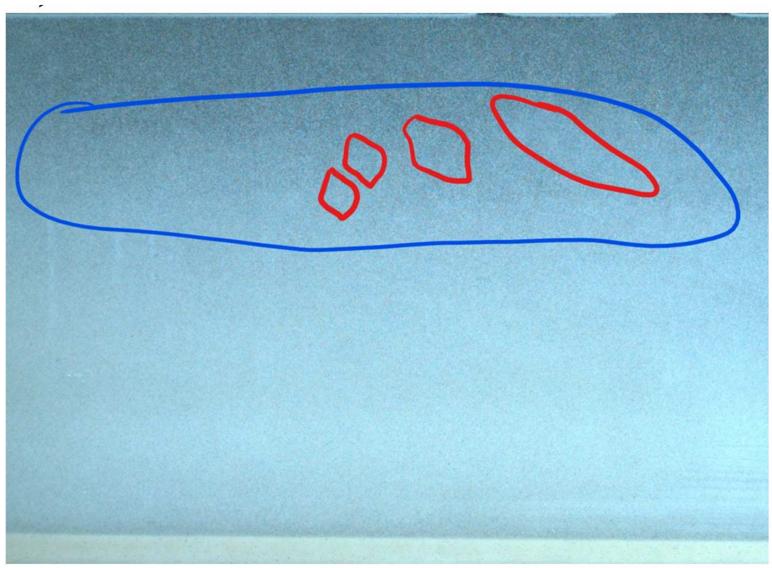

Figure 4.14d Type C of Particle Agglomeration: Clusters and Layers Combined for Experiment 18

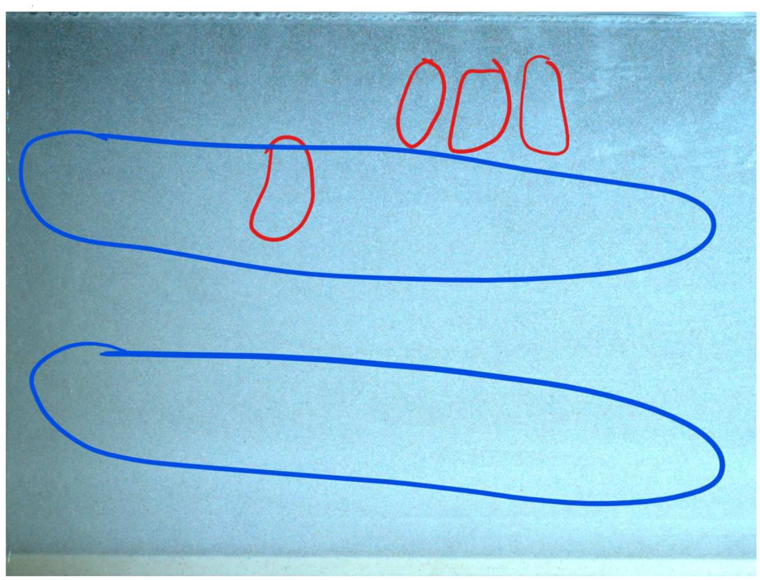

Figure 4.14e Type C of Particle Agglomeration: Clusters and Layers Combined for Experiment 19

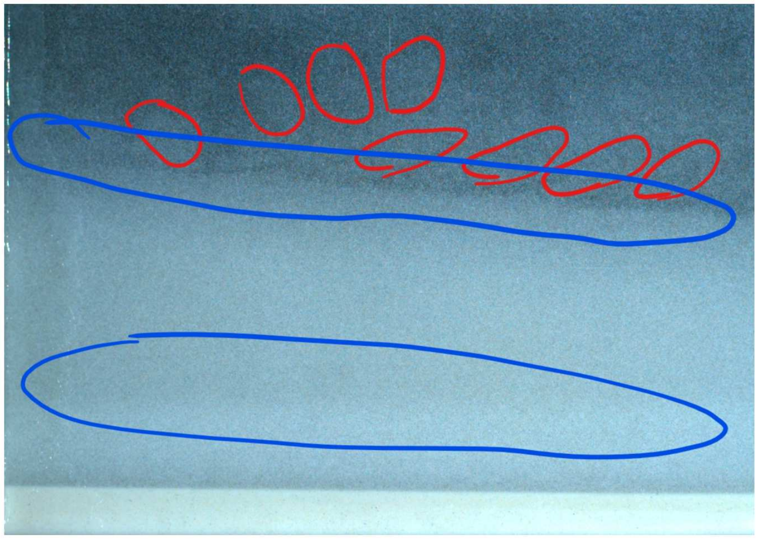

Figure 4.14f Type C of Particle Agglomeration: Clusters and Layers Combined for Experiment 21

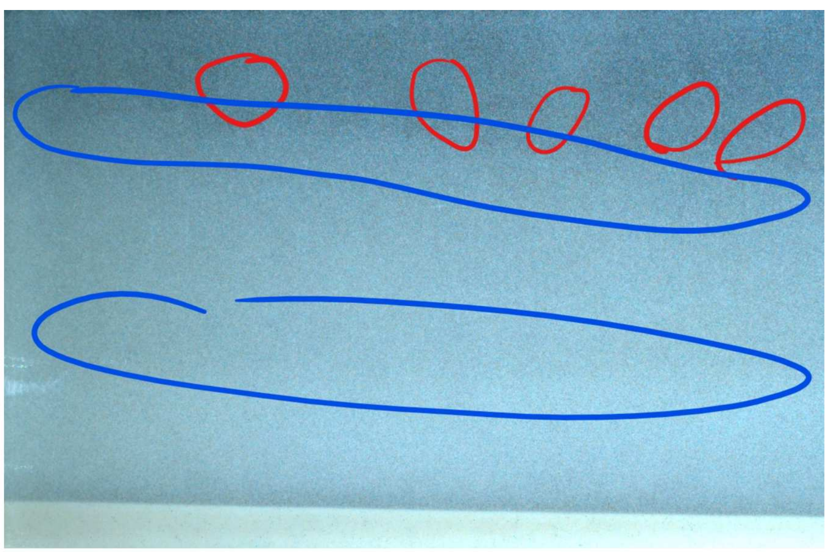

Figure 4.14g Type C of Particle Agglomeration: Clusters and Layers Combined for Experiment 22

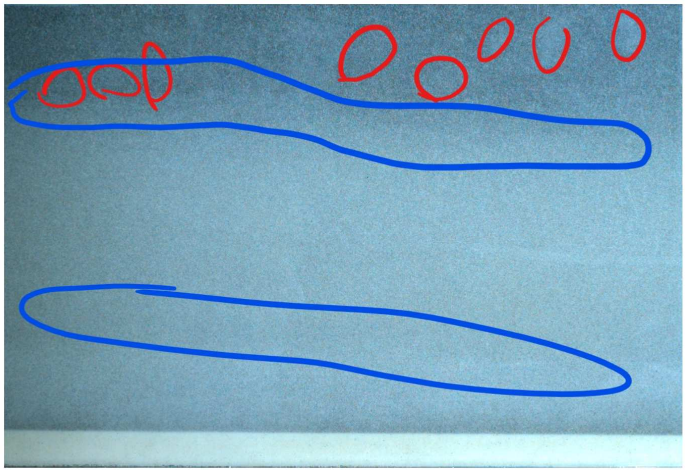

Figure 4.14h Type C of Particle Agglomeration: Clusters and Layers Combined for Experiment 23

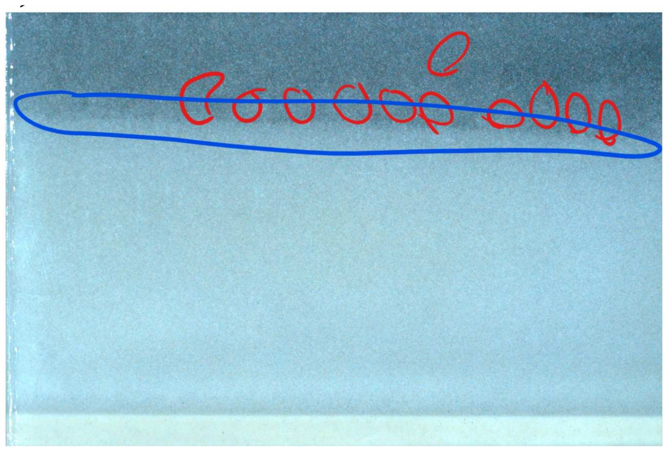

Figure 4.14i Type C of Particle Agglomeration: Clusters and Layers Combined for Experiment 24

4.3 Results from GeoPIV Analysis

4.3.1 Horizontal Displacement Plots

This section summarizes particle horizontal displacements for all experiments considering effect of fracture intersection angle, fluid viscosity, fluid flow rate, and proppant volumetric concentration as shown in Figure 4.15. One clear observed trend is as fluid viscosity increases (EXP 01-08 vs. 09-16 vs. 17-24), the particle horizontal displacement decreases. It is also observed that more horizontal particle clustering presents as fluid viscosity increases. Those are shown in the figures where local regions have same velocity and different from surrounding regions.

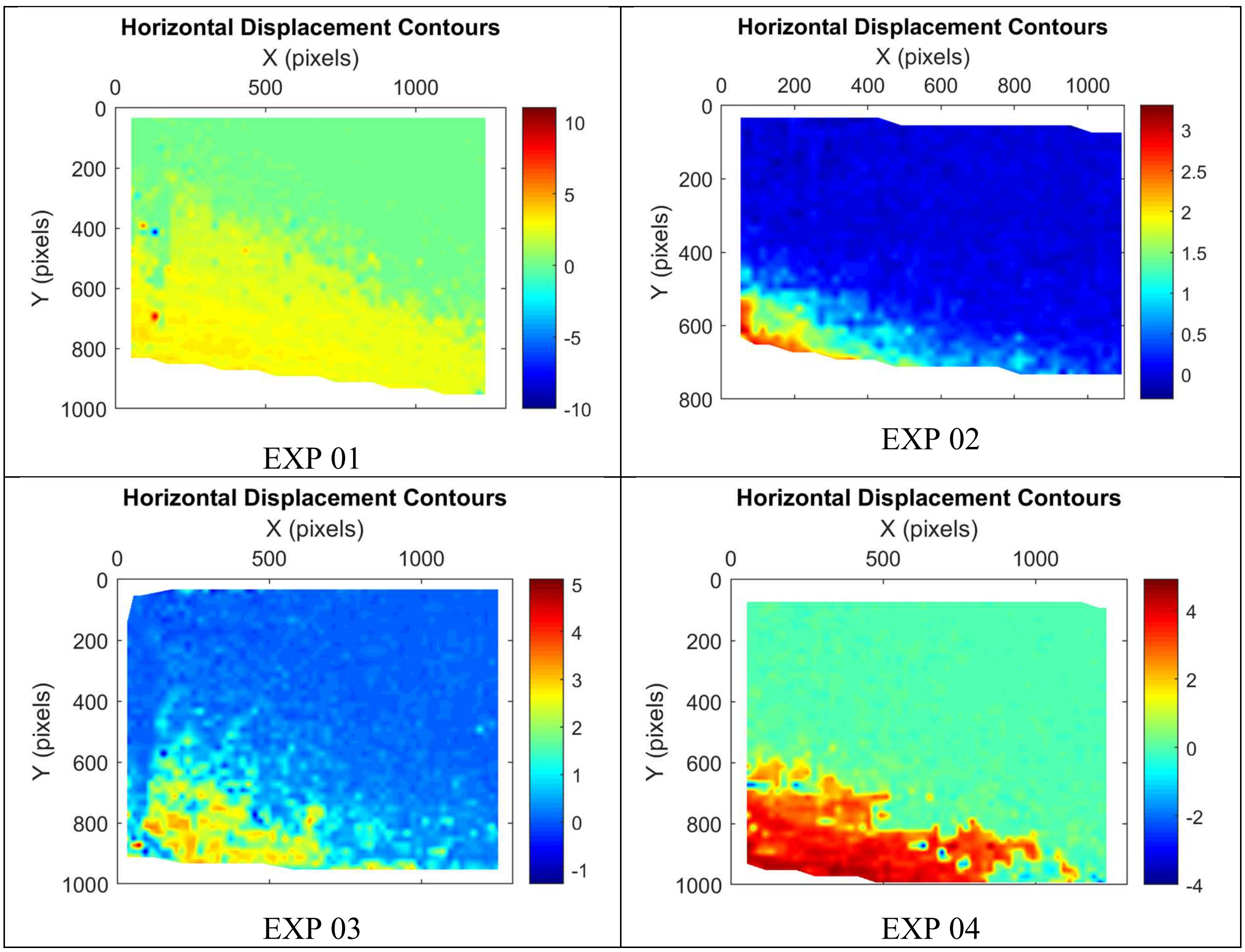

Figure 4.15 Horizontal Displacement Contours by PIV Analysis for All Experiments

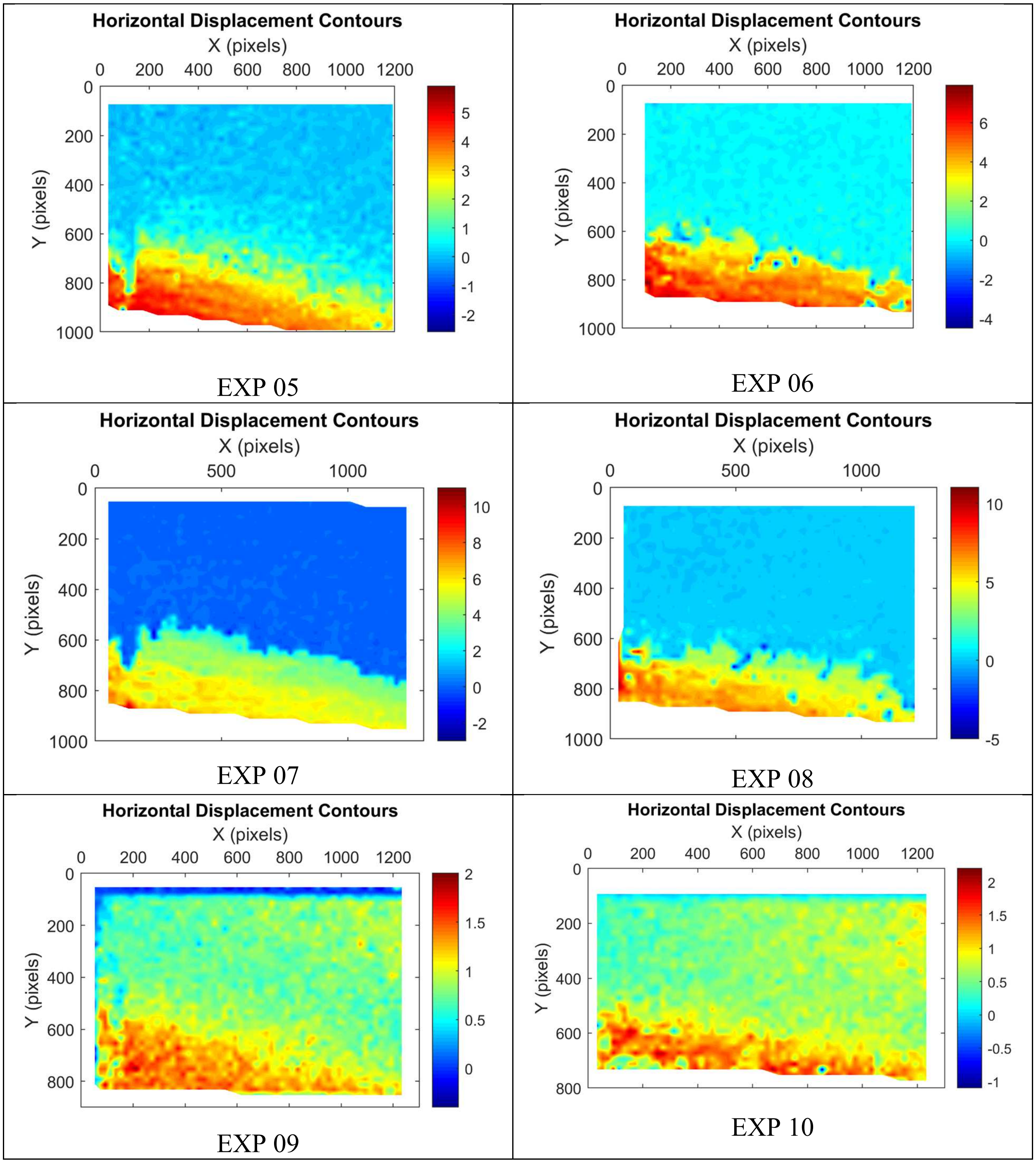

Figure 4.15 continued

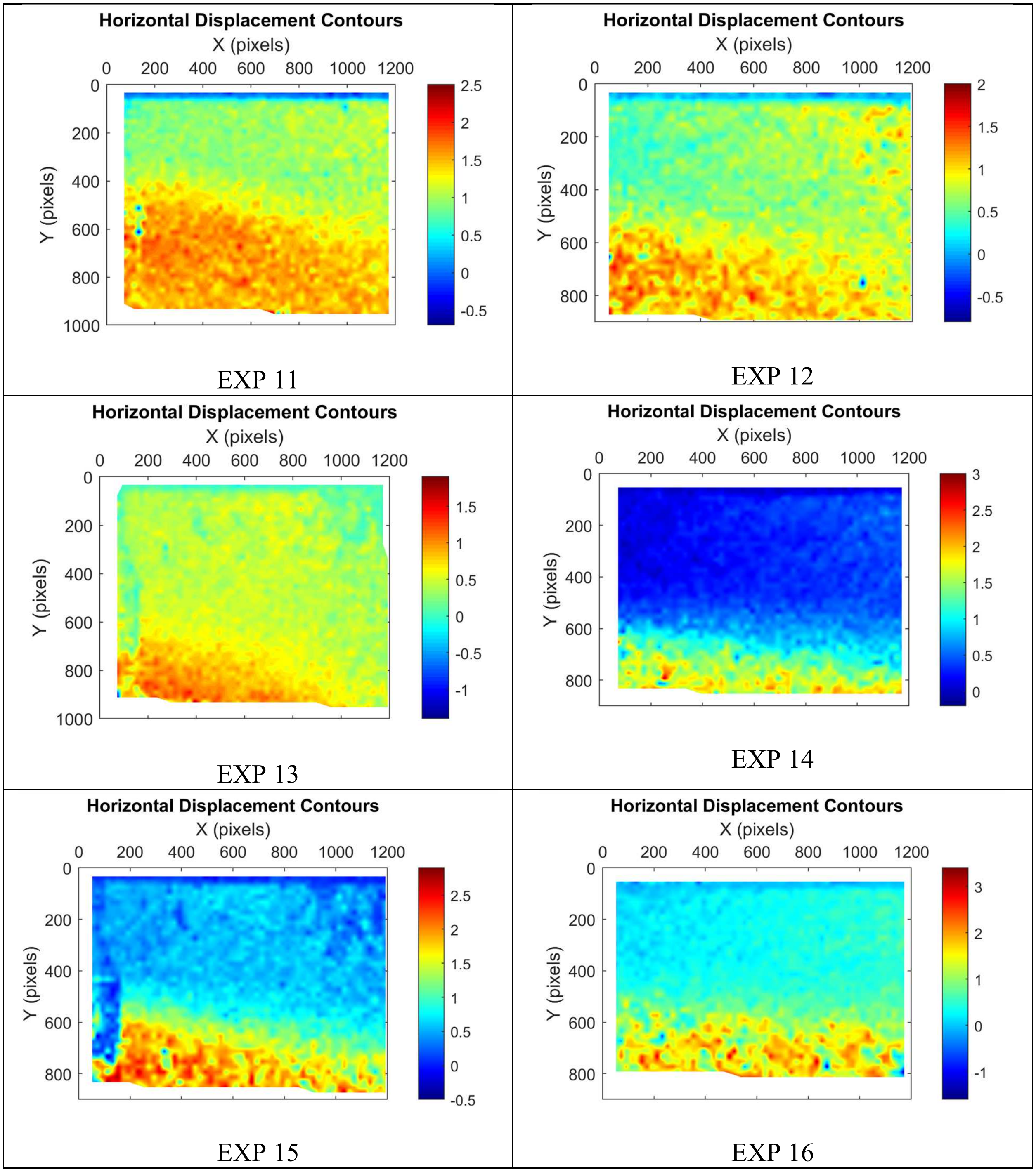

Figure 4.15 continued

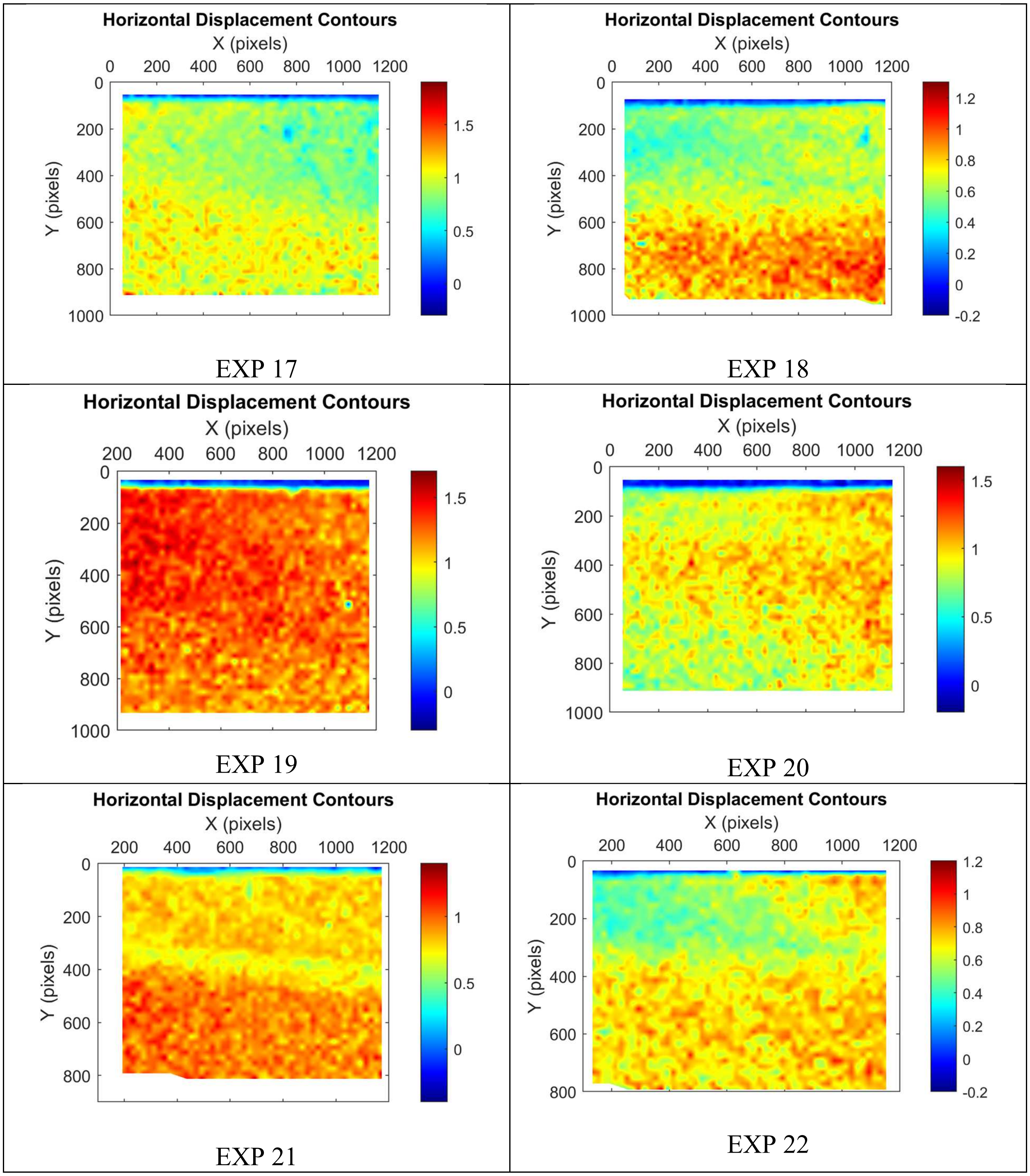

Figure 4.15 continued

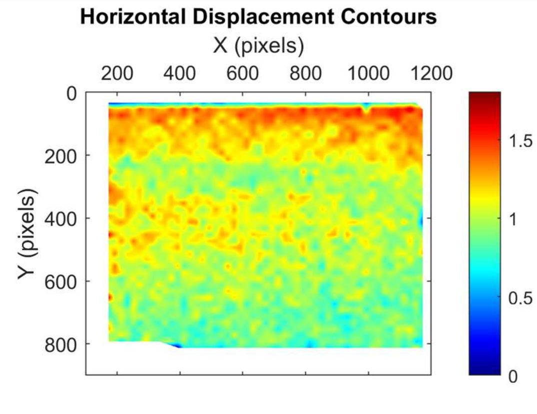

EXP 23

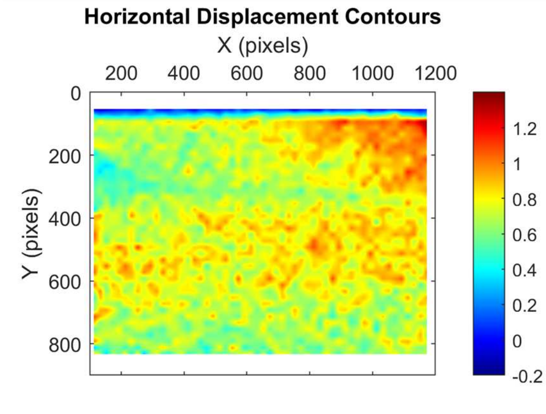

EXP 24

Figure 4.15 continued

4.3.2 Vertical Displacements Plots

This section summarizes particle vertical displacement contour for all experiments considering effect of fracture intersection angle, fluid viscosity, fluid flow rate, and proppant volumetric concentration as shown in Figure 4.16. Unlike horizontal displacement, vertical displacement does not have clear decreasing trend yet still observable as fluid viscosity increase (EXP 01-08 vs. 09-16 vs. 17-24). Under lower viscosity, gravitational force dominates particle settlement motion. While under higher viscosity, gravitational force has weaker effect on particle settlement. It is also observed that more vertical particle clustering presents as fluid viscosity increases. Those are shown in the figures where local regions have same velocity and different from surrounding regions. As fluid viscosity increase, vertical particle clustering becomes more obvious.

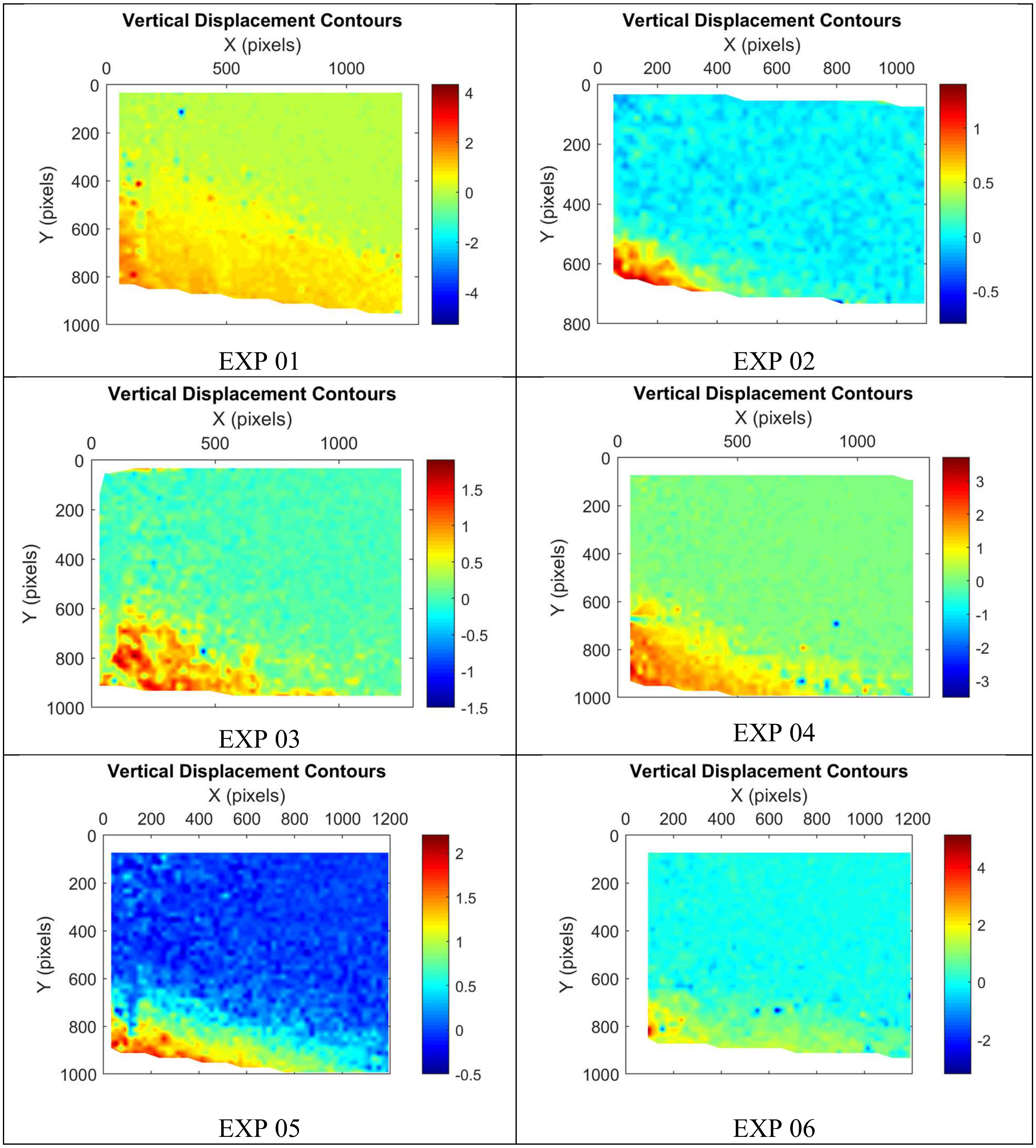

Figure 4.16 Vertical Displacement Contours by PIV Analysis for All Experiments

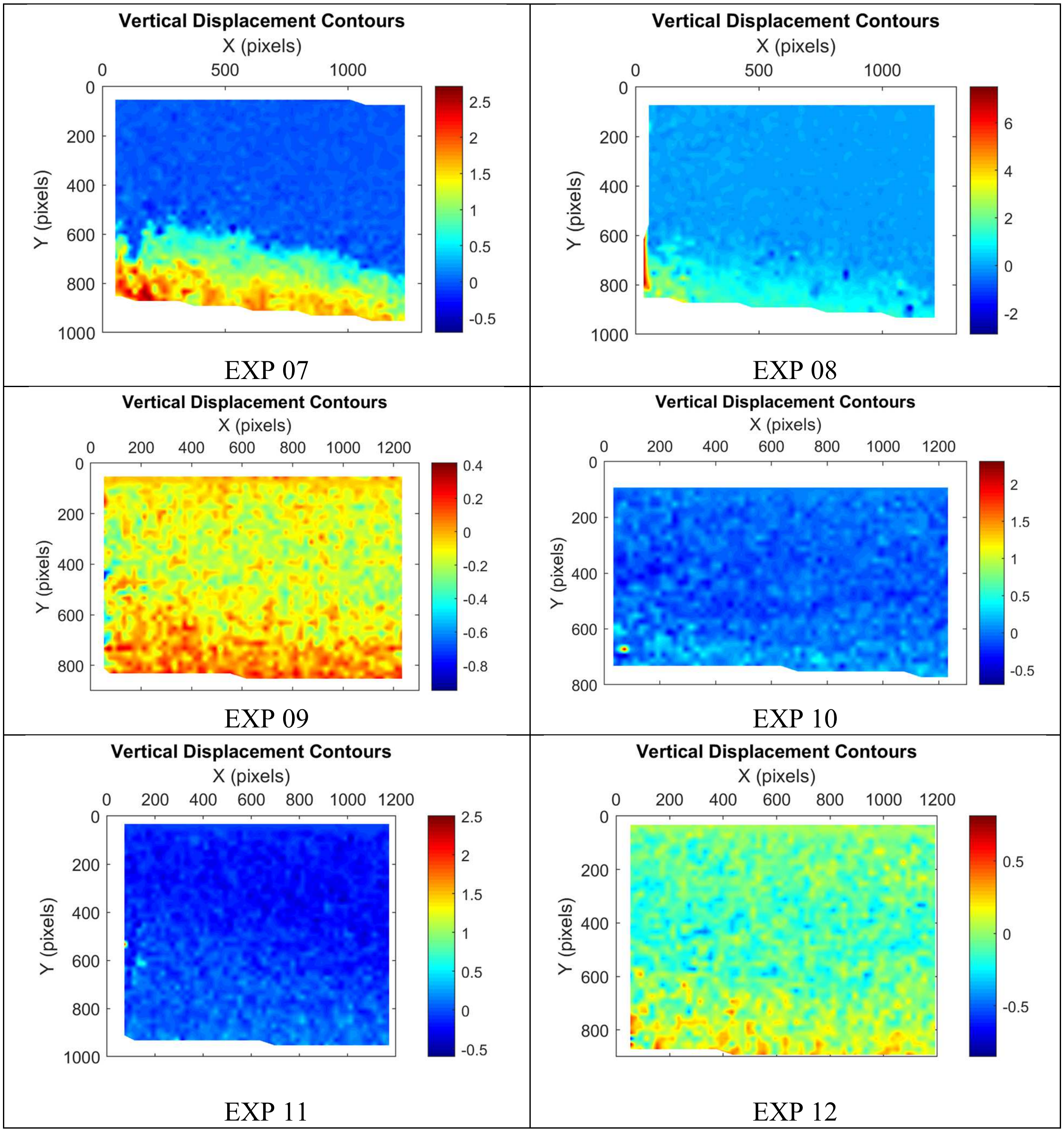

Figure 4.16 continued

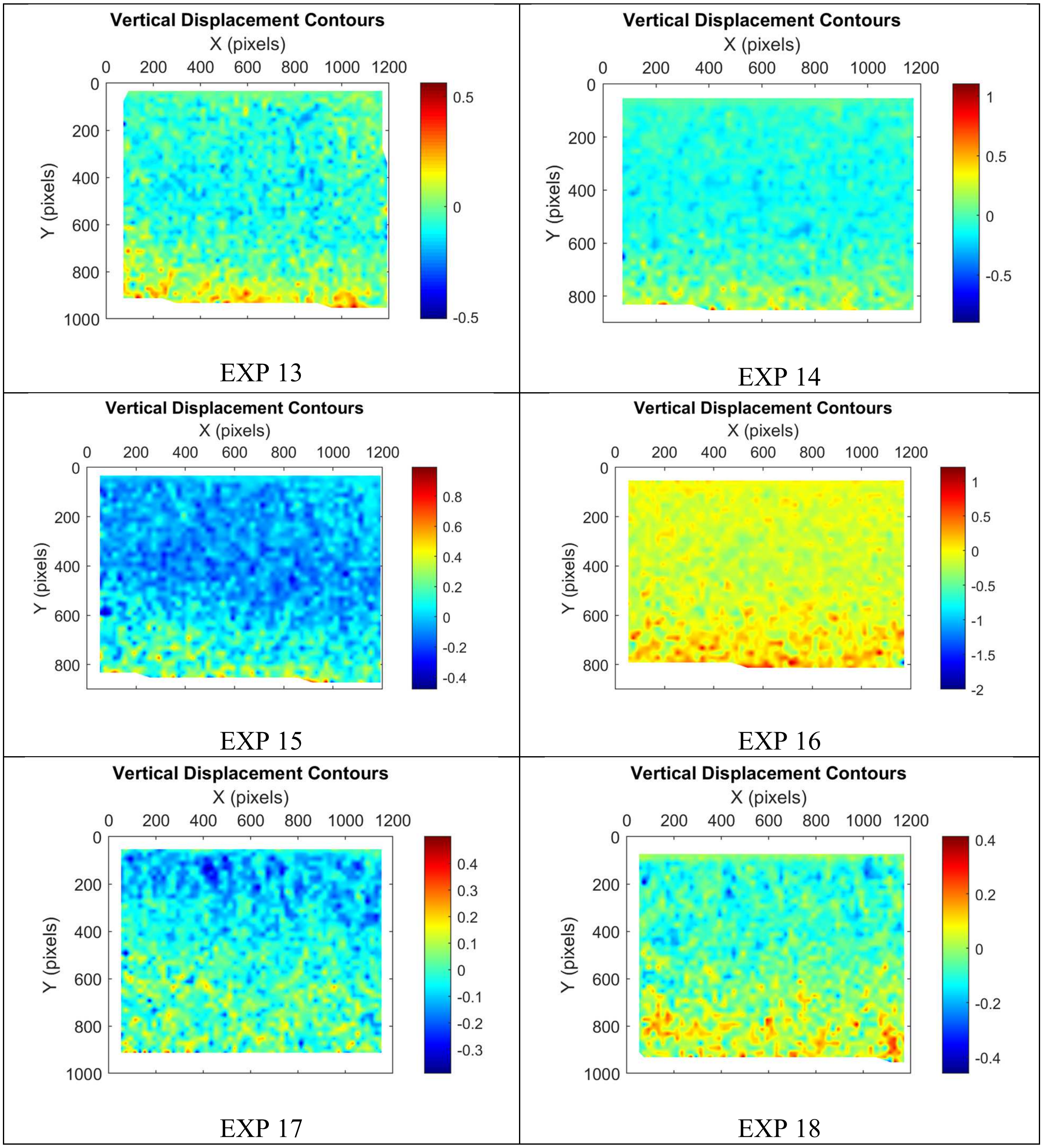

Figure 4.16 continued

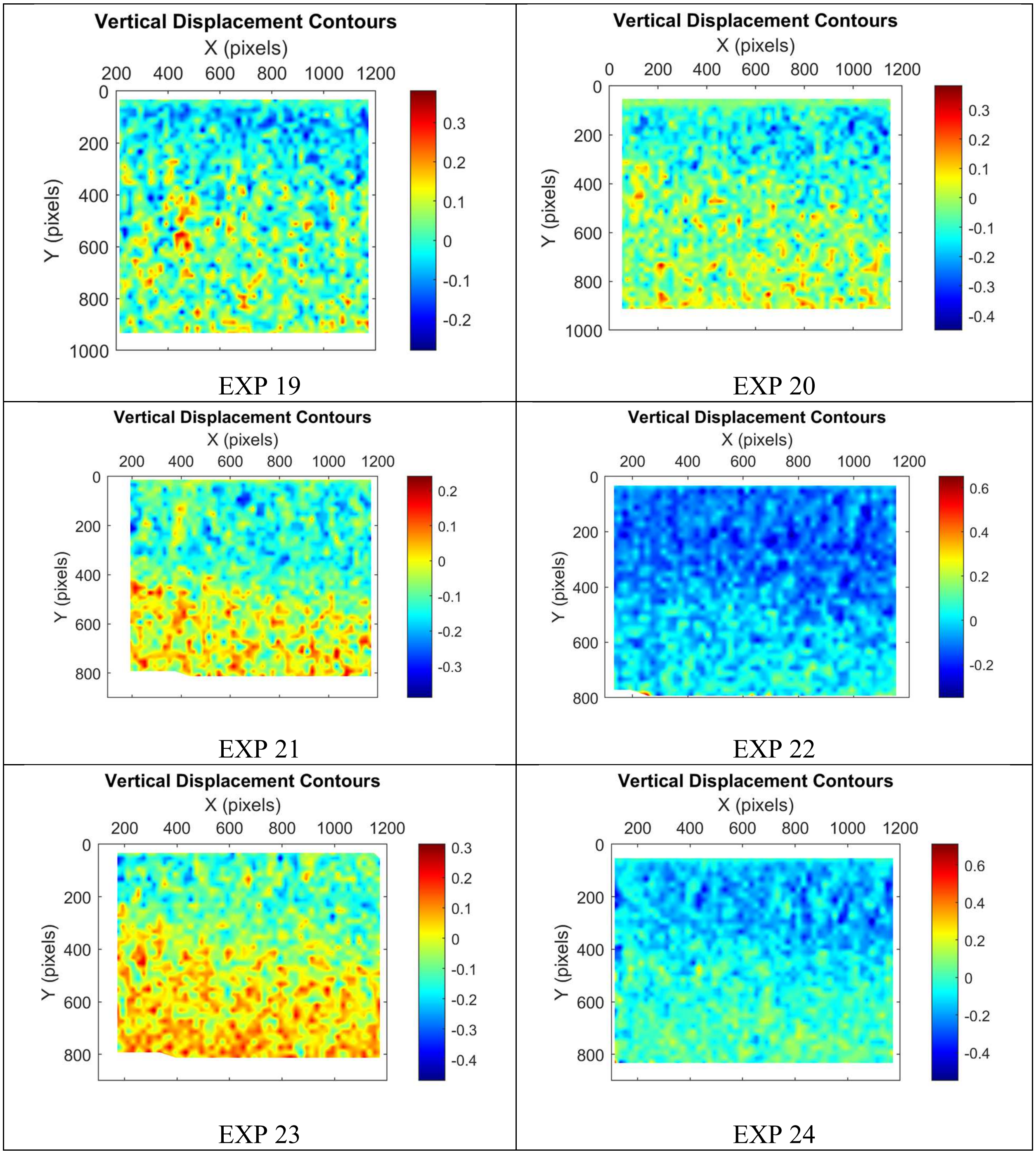

Figure 4.16 continued

4.3.3 Resultant Displacement Plots

This section summarizes particle resultant displacement contour for all experiments considering effect of fracture intersection angle, fluid viscosity, fluid flow rate, and proppant volumetric concentration as shown in Figure 4.17. One clear observed trend is as fluid viscosity increases (EXP 01-08 vs. 09-16 vs. 17-24), the particle resultant displacement decreases same as particle horizontal displacement. It is also observed that more resultant particle clustering presents as fluid viscosity increases. Those are shown in the figures where local regions have same velocity and different from surrounding regions.

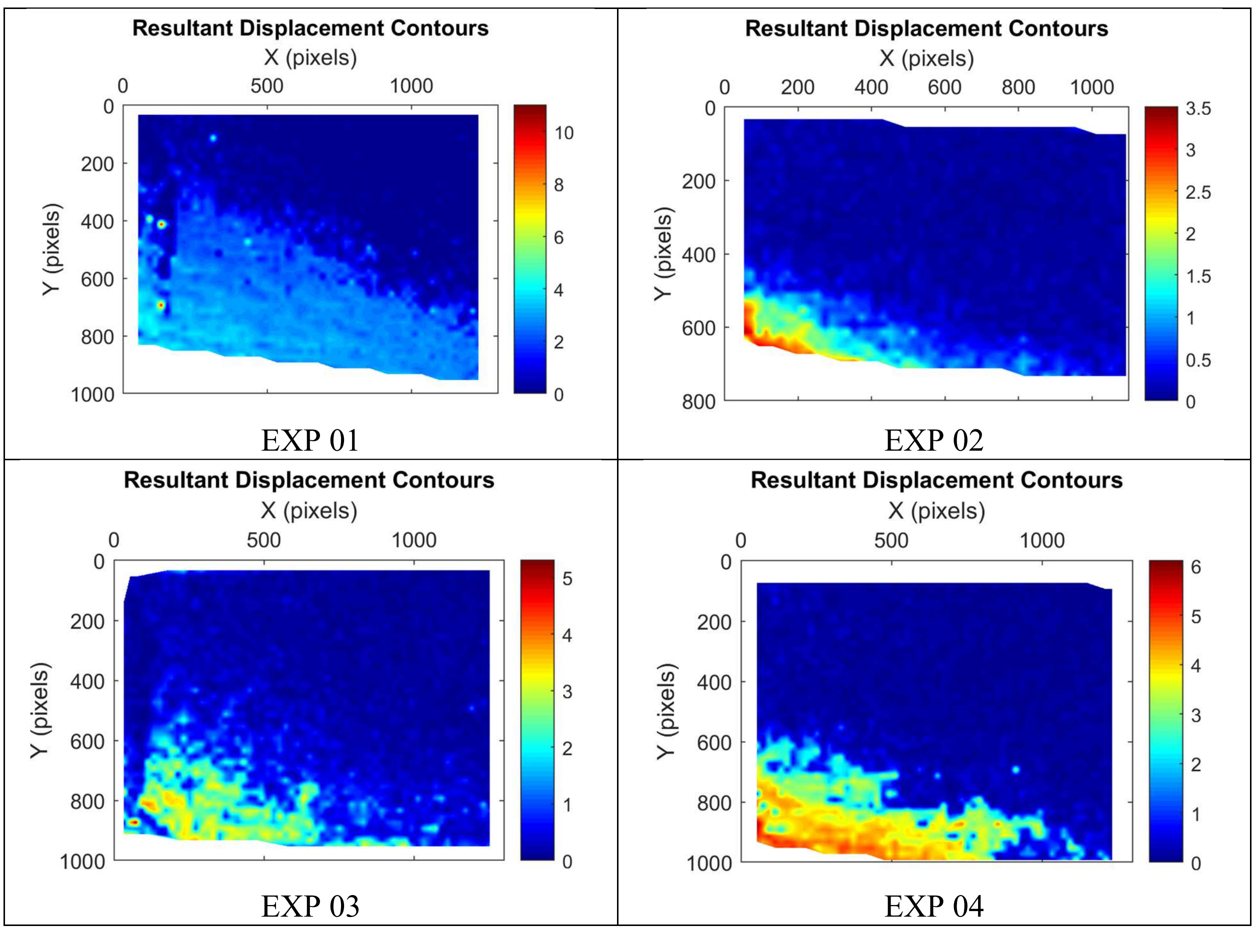

Figure 4.17 Resultant Displacement Contours by PIV Analysis for All Experiments

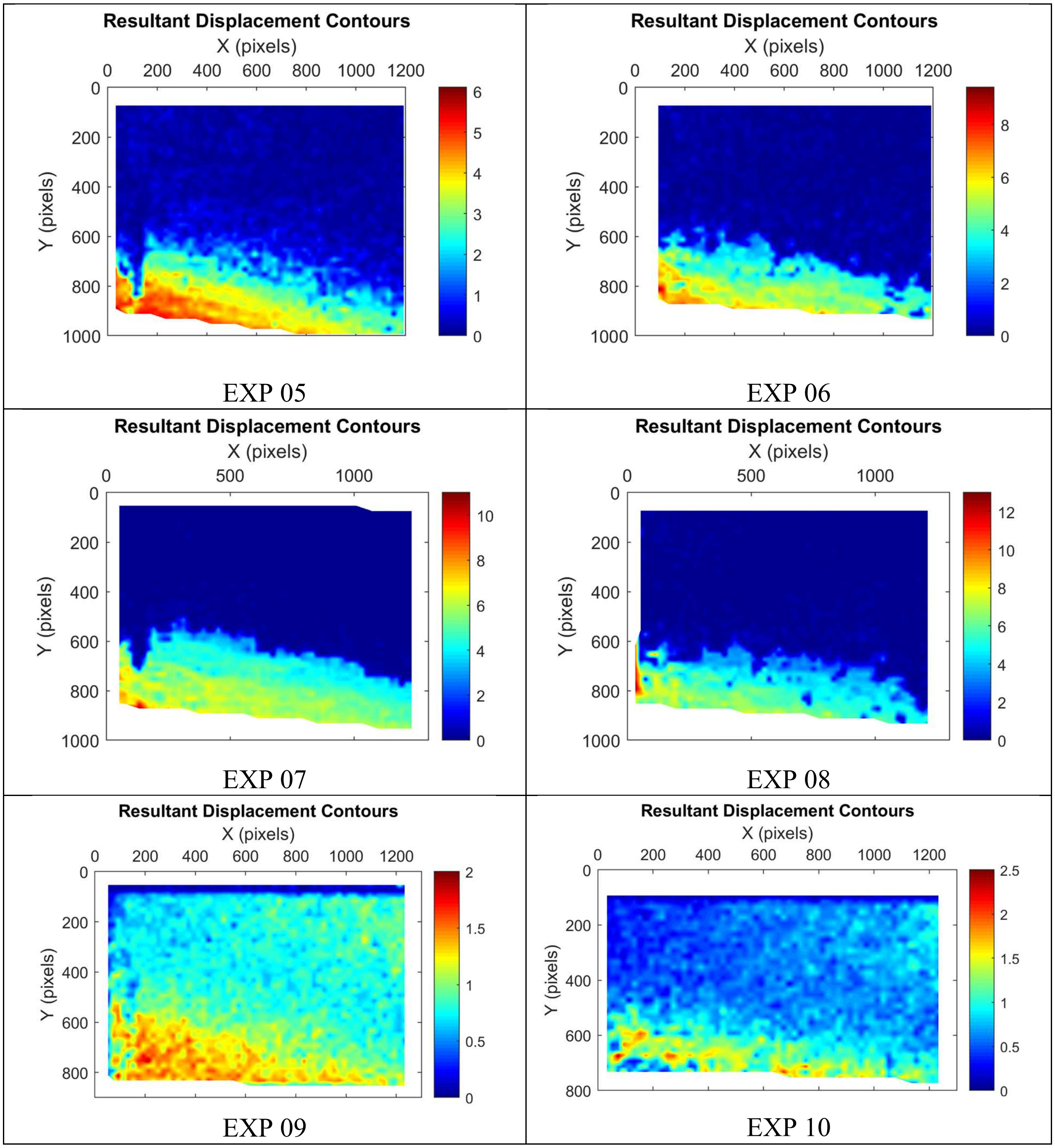

Figure 4.17 continued

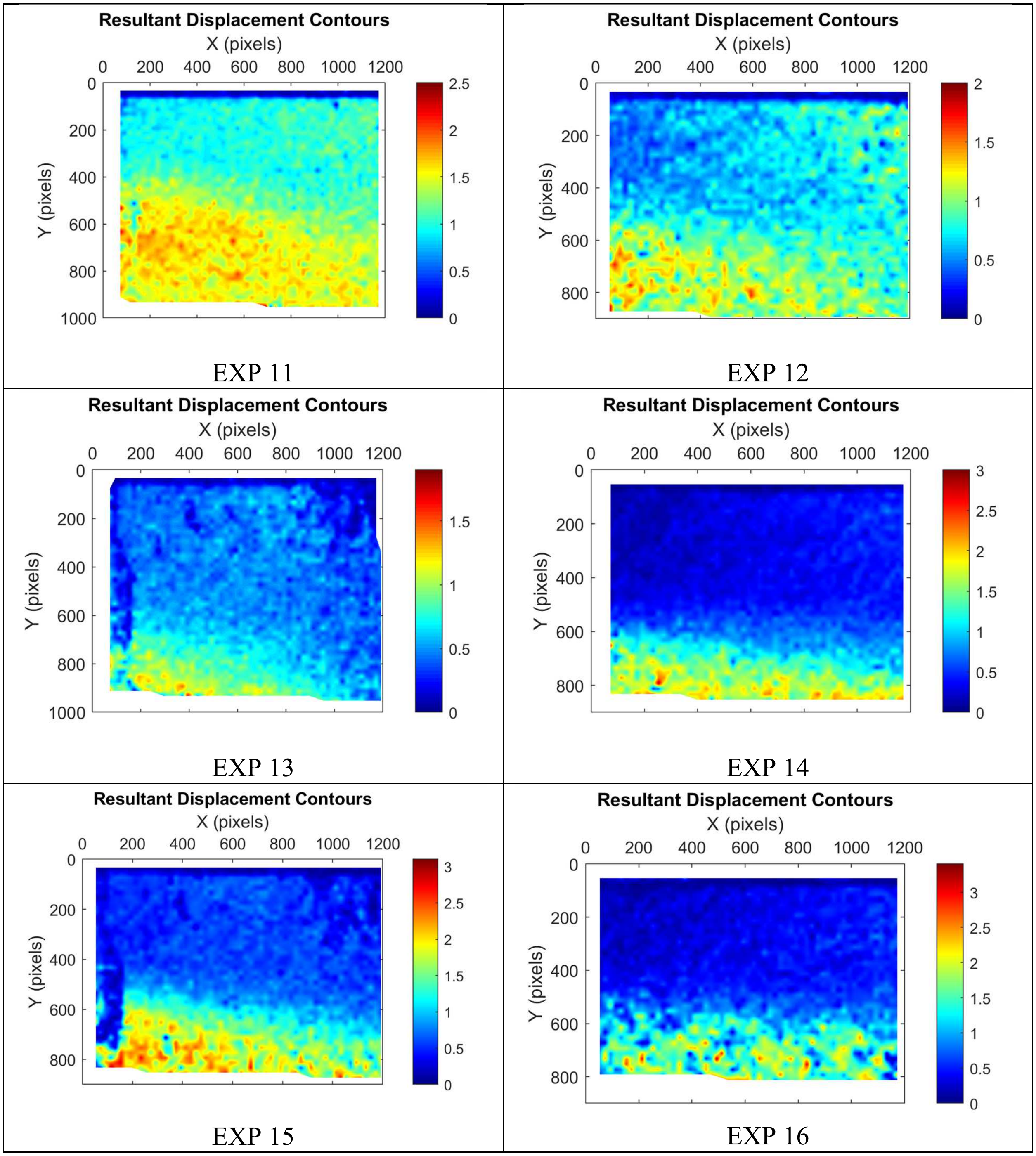

Figure 4.17 continued

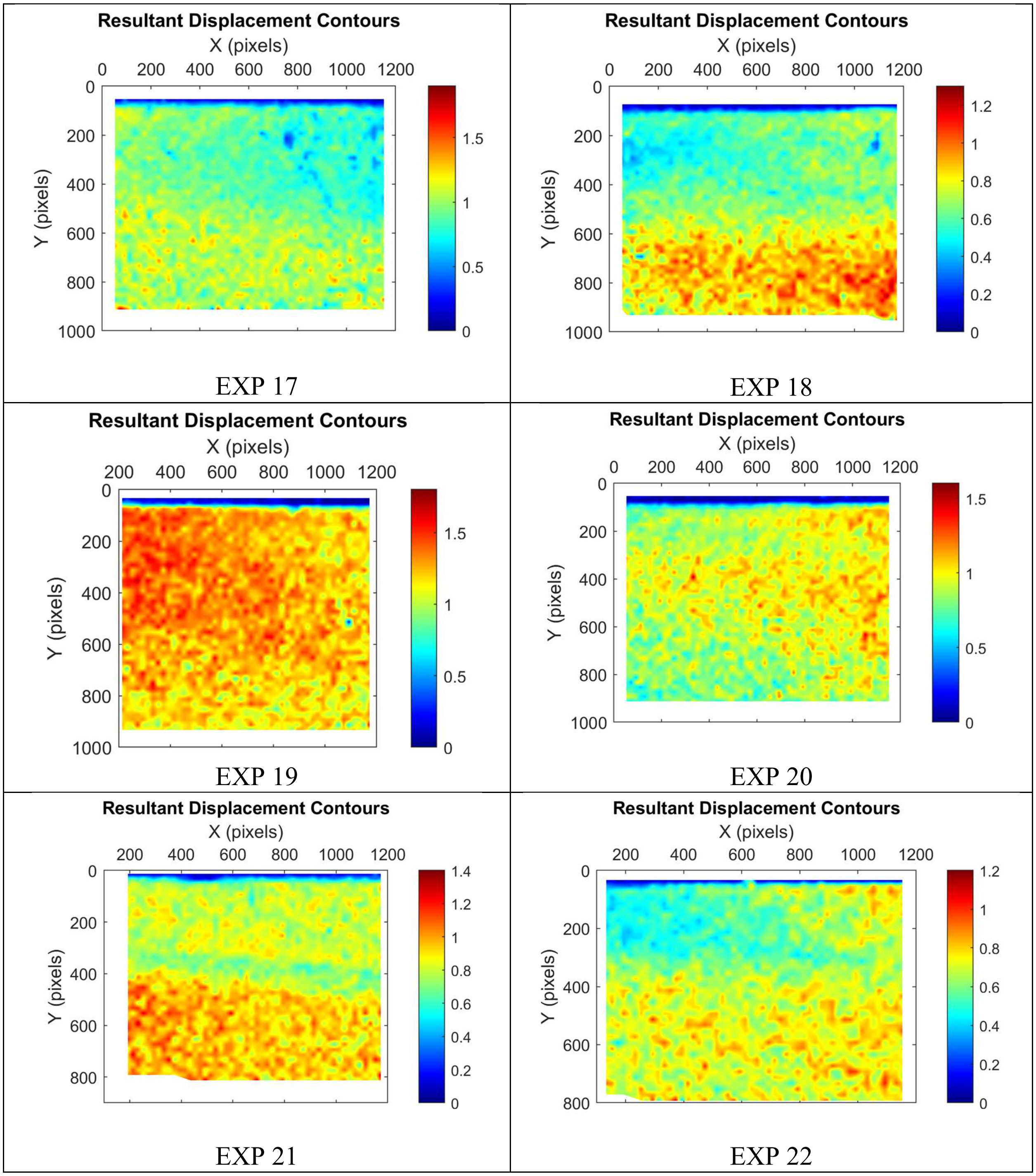

Figure 4.17 continued

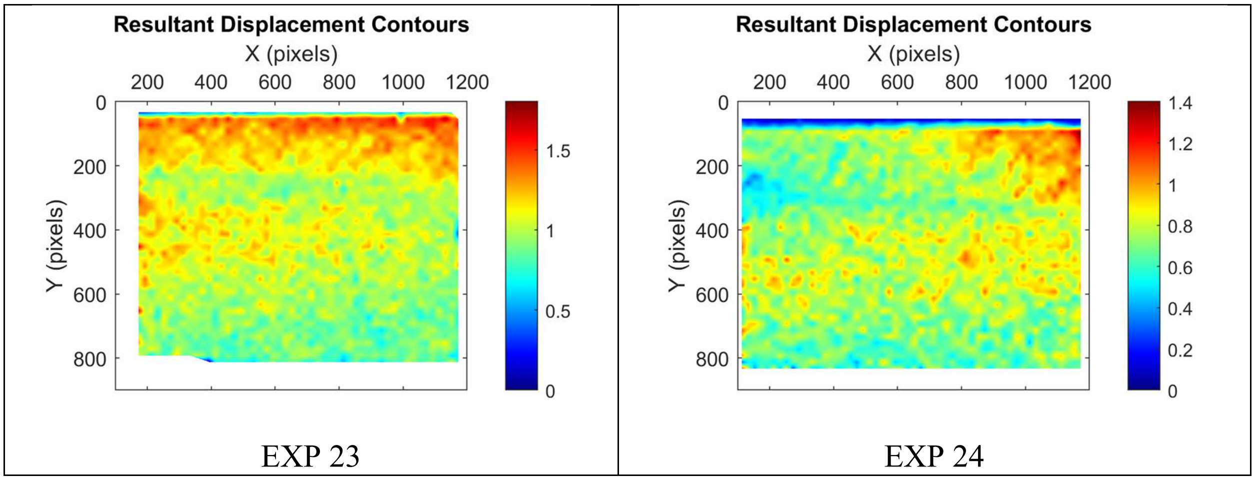

Figure 4.17 continued

4.3.4 Displacement Vector Field

This section summarizes particle displacement vector fields for all experiments considering effect of fracture intersection angle, fluid viscosity, fluid flow rate, and proppant volumetric concentration as shown in Figure 4.18. One clear observed trend is as fluid viscosity increases (EXP 01-08 vs. 09-16 vs. 17-24), the particle velocities are decreasing clearly.

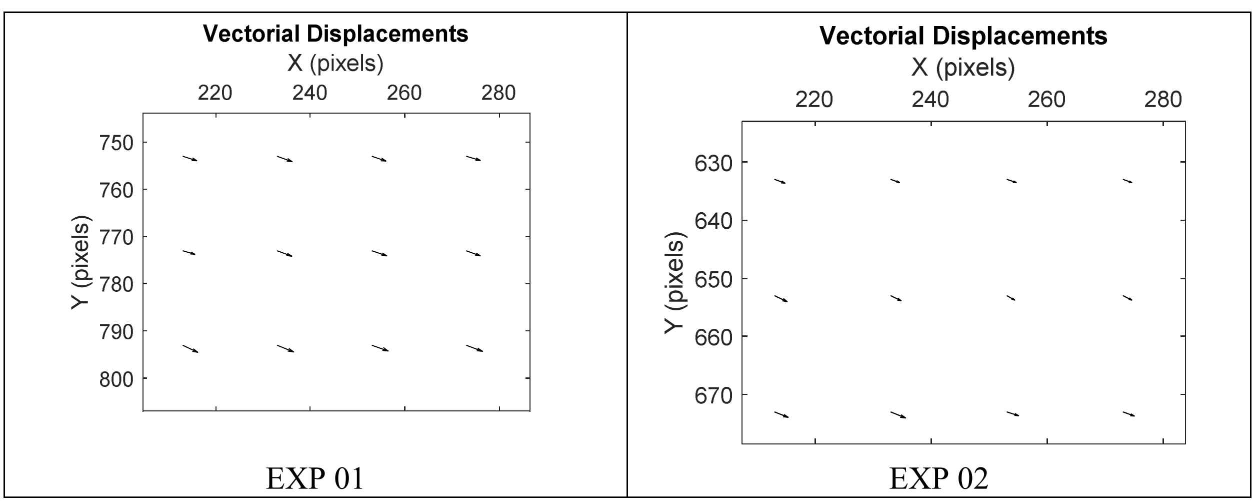

Figure 4.18 Displacement Vector Field by PIV Analysis for All Experiments

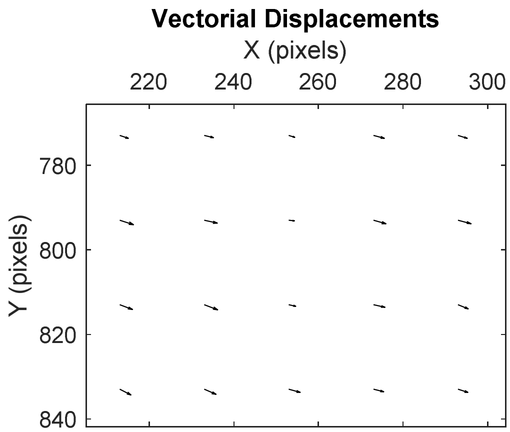

EXP 03

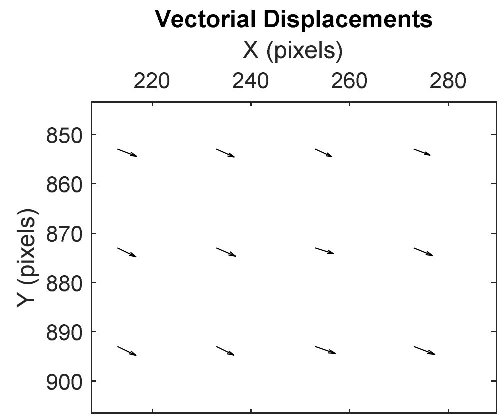

EXP 04

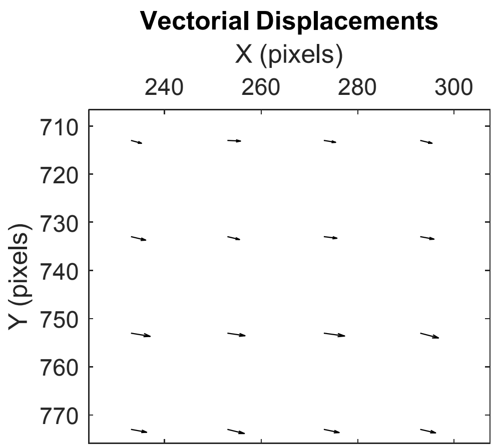

EXP 05

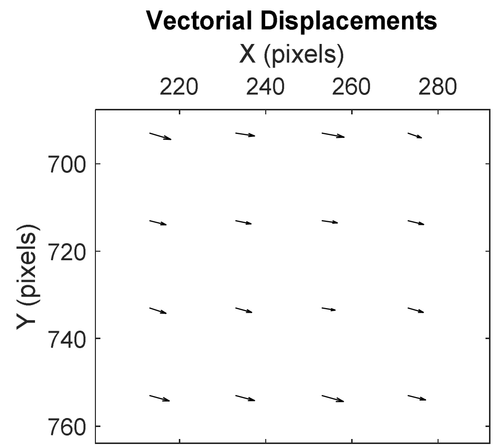

EXP 06

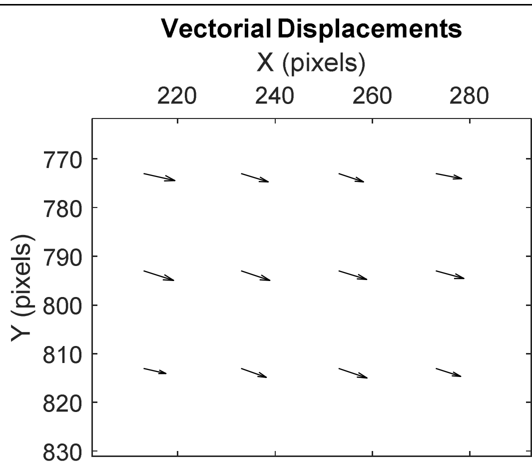

EXP 07

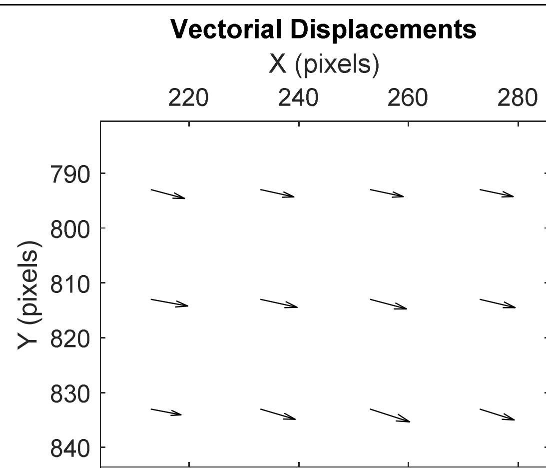

EXP 08

Figure 4.18 continued

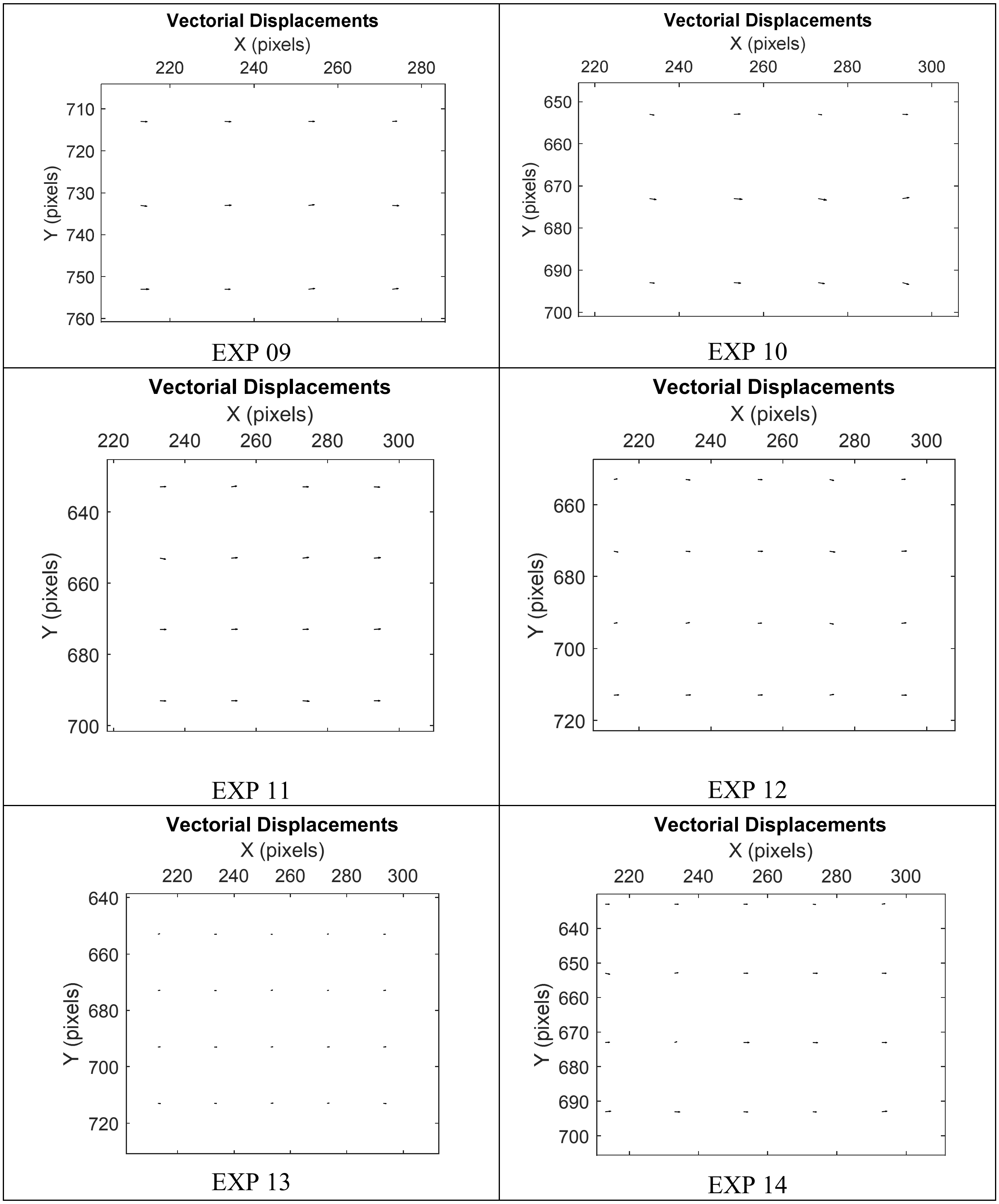

Figure 4.18 continued

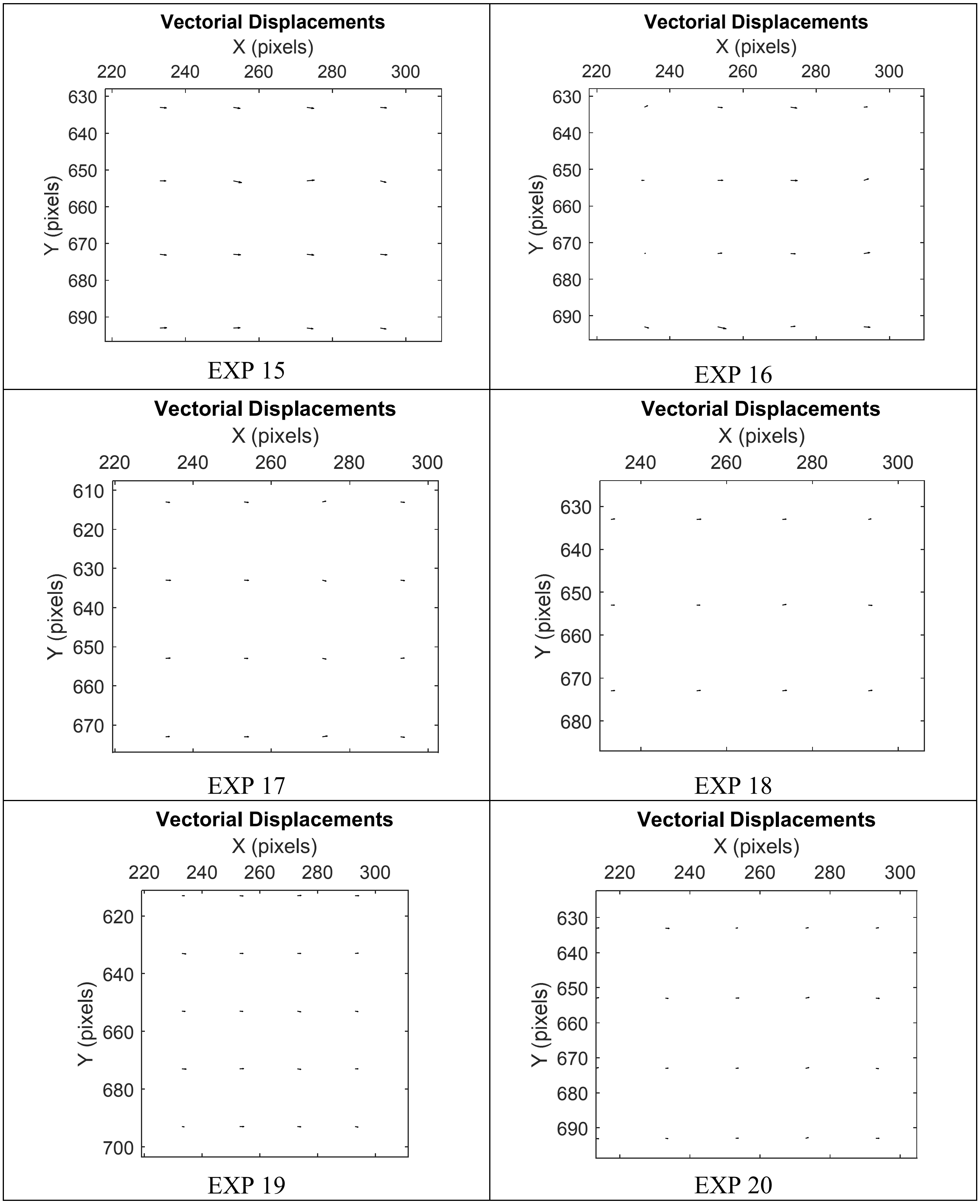

Figure 4.18 continued

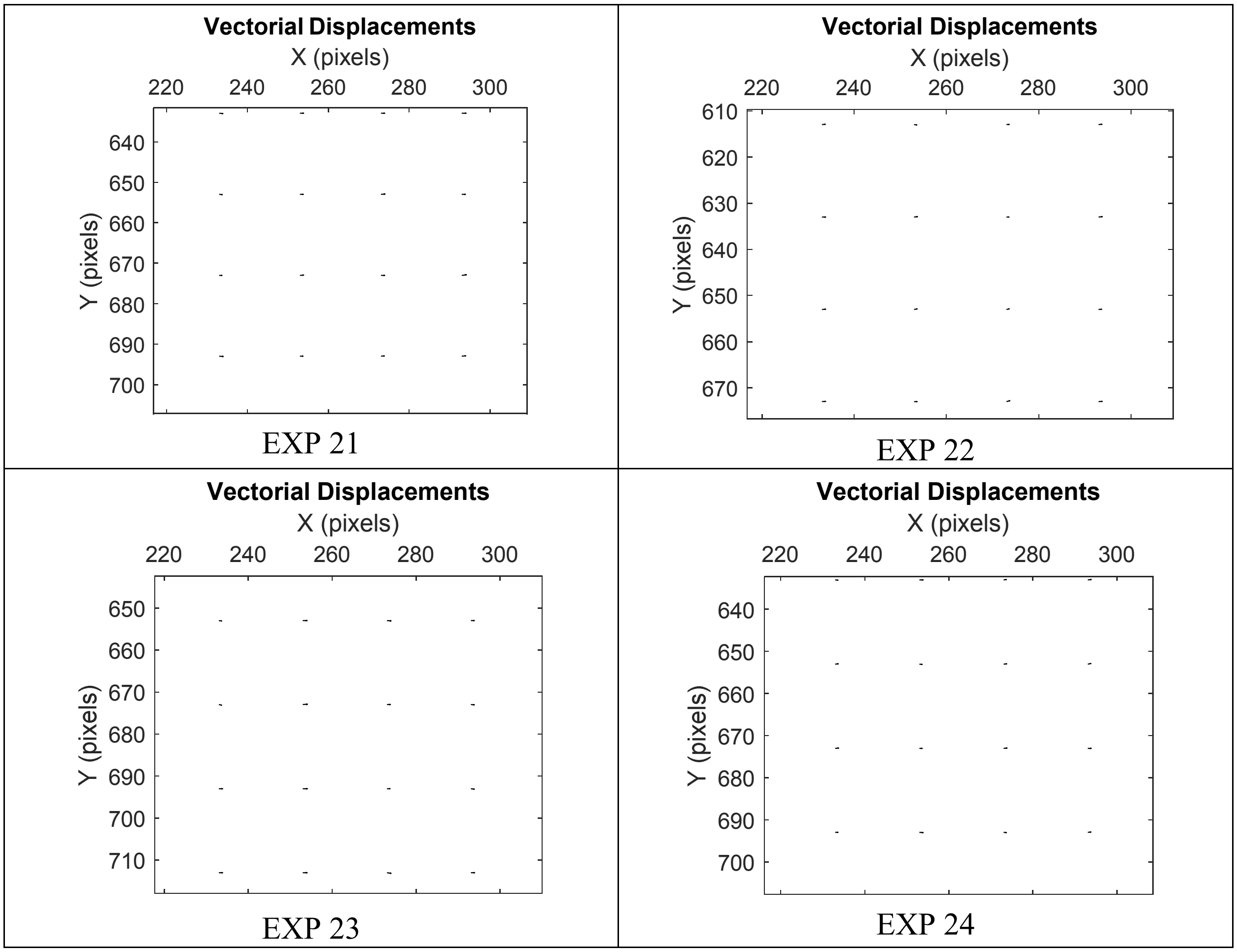

Figure 4.18 continued

4.4 Processed GeoPIV Results

4.4.1 Velocity Vector Field

This section summarizes particle velocity vector fields for all experiments considering effect of fracture intersection angle, fluid viscosity, fluid flow rate, and proppant volumetric concentration as shown in Figure 4.19.

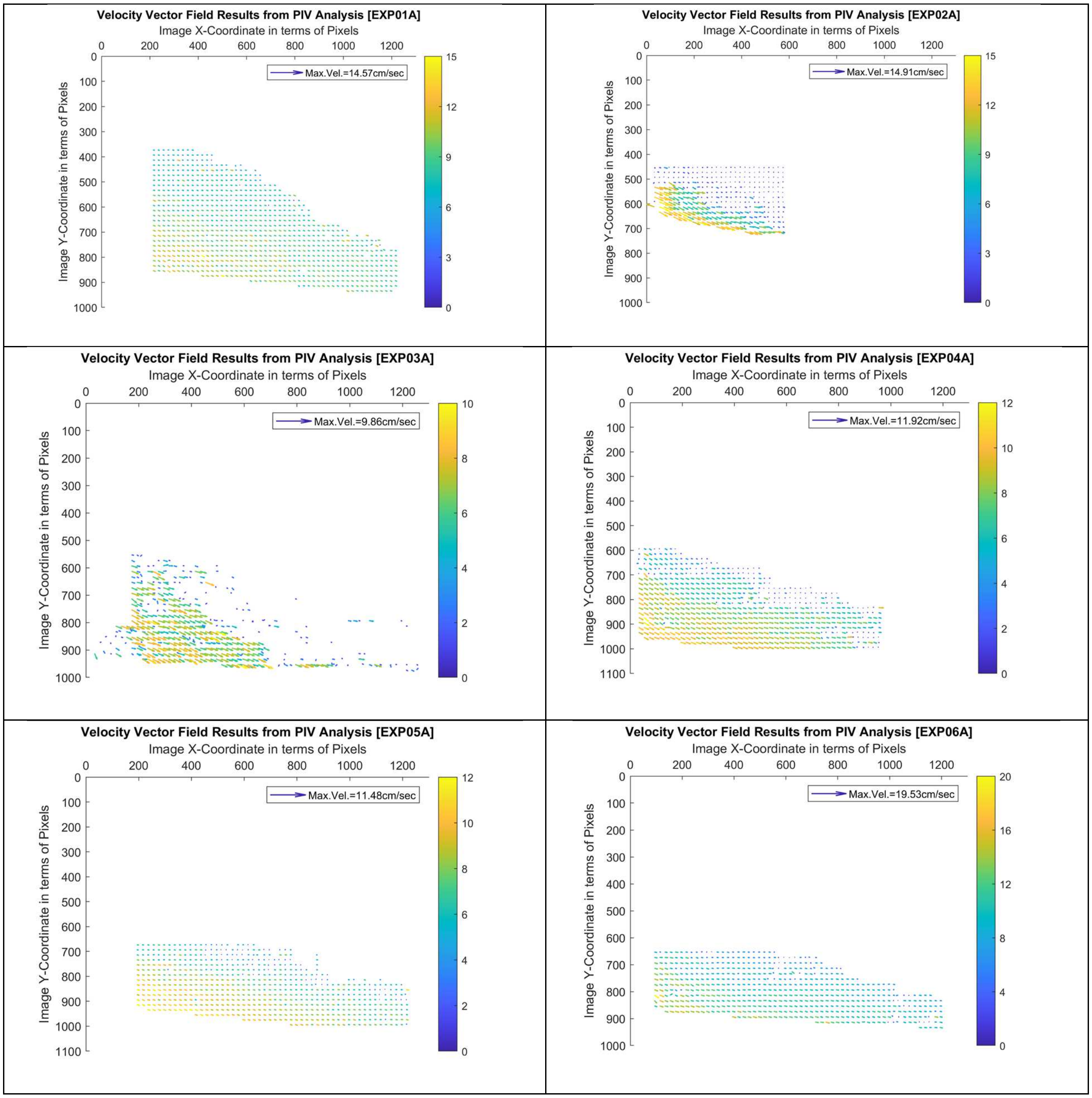

Figure 4.19 Velocity Vector Fields for Selected Regions by GeoPIV Analysis for All Experiments

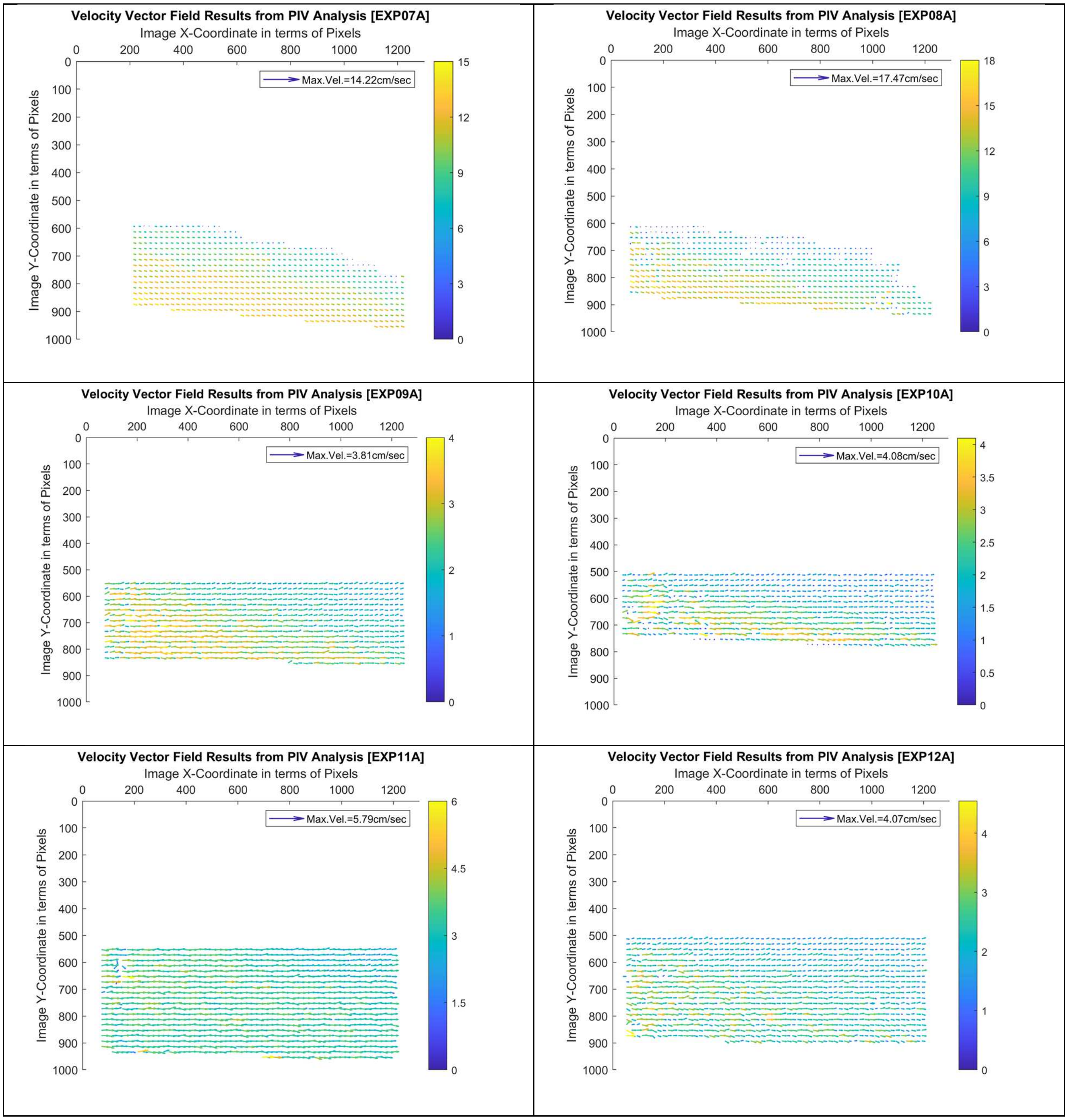

Figure 4.19 continued

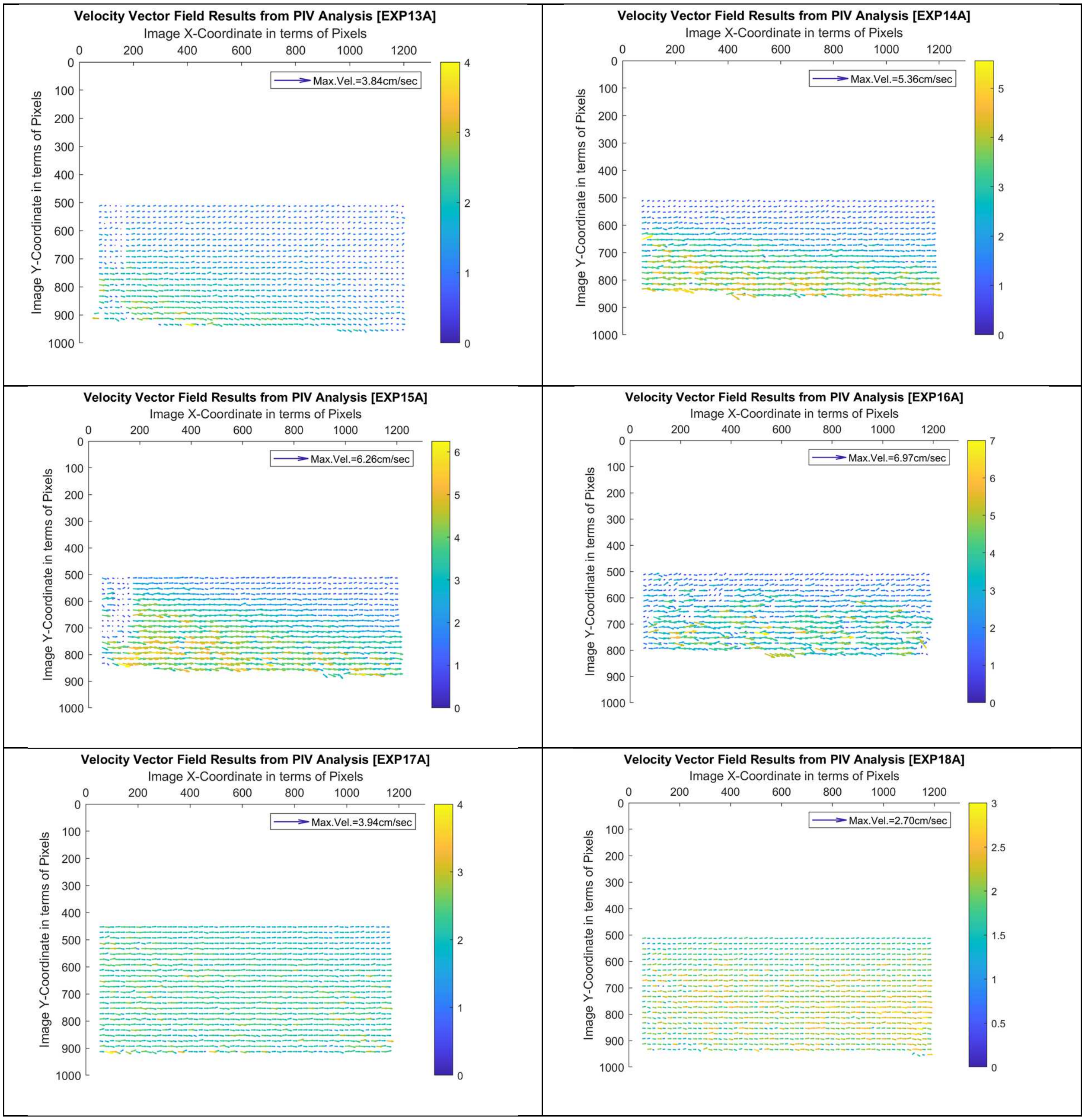

Figure 4.19 continued

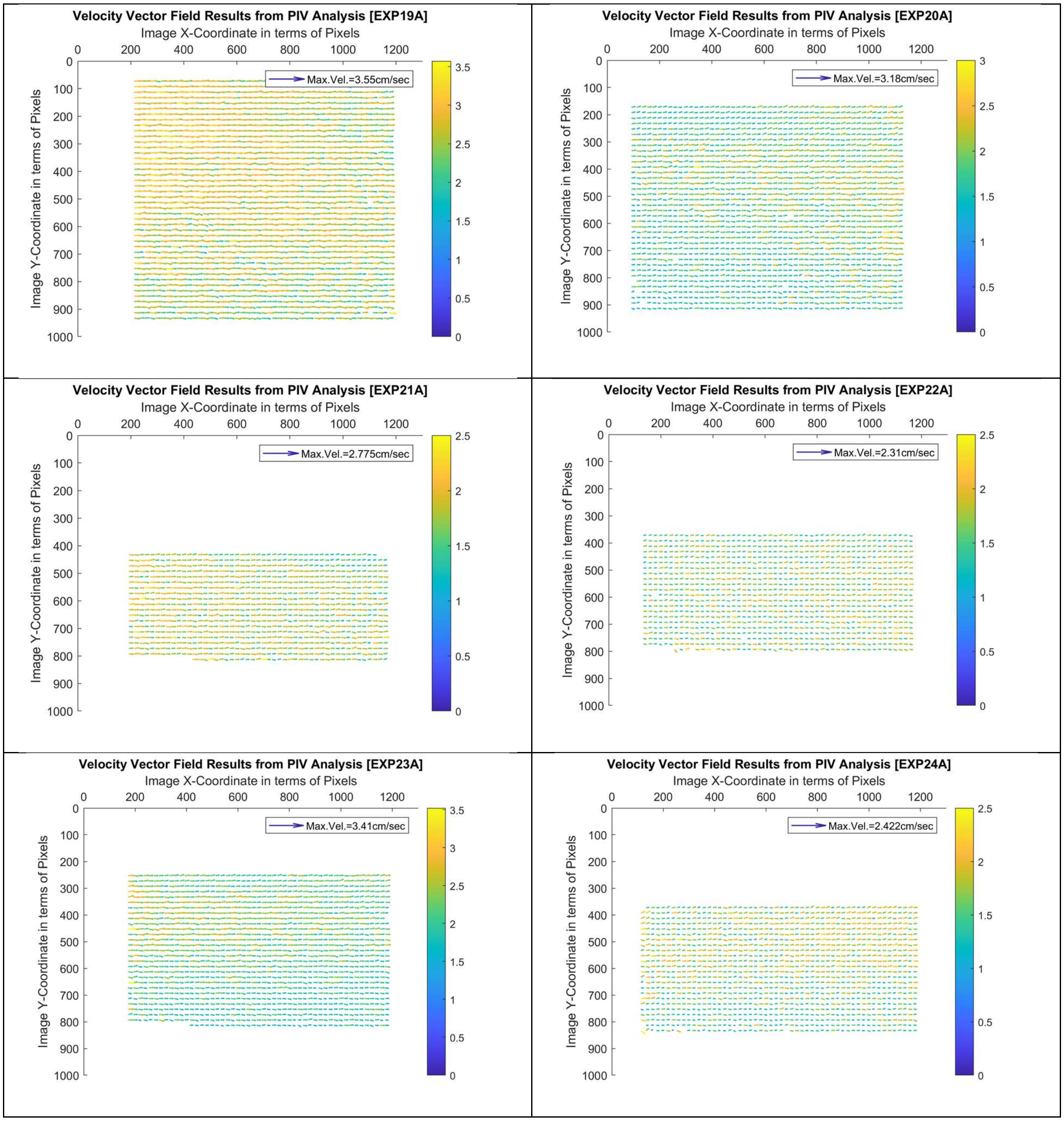

Figure 4.19 continued

4.4.2 Histograms of Velocity Vector Direction

This section summarizes histogram distribution of particle velocity vector directions relative to horizontal level for all experiments considering effect of fracture intersection angle, fluid viscosity, fluid flow rate, and proppant volumetric concentration as shown in Figure 4.20.

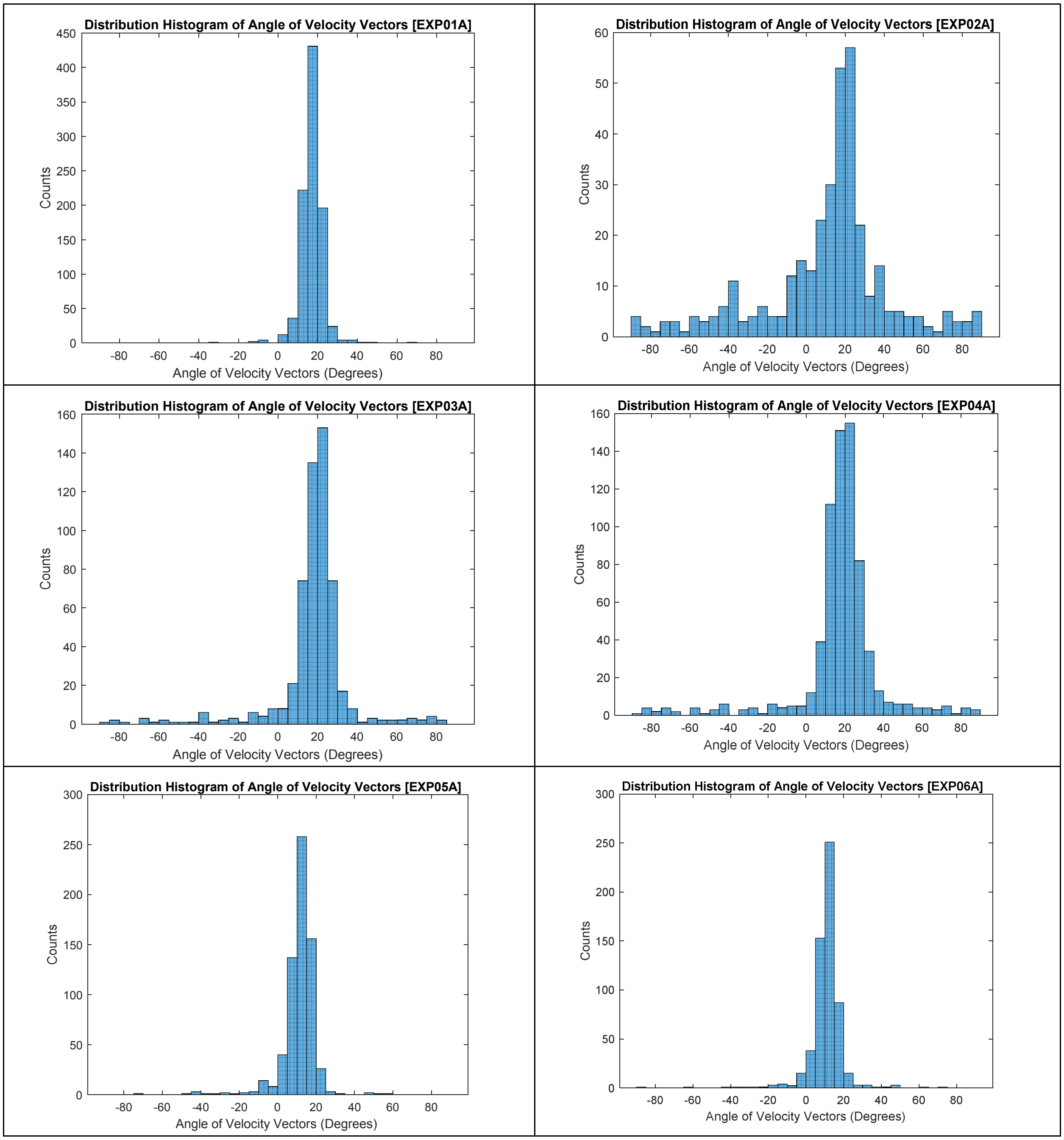

Figure 4.20 Histogram of Velocity Vector Direction Angles for Selected Regions by GeoPIV Analysis for All Experiments

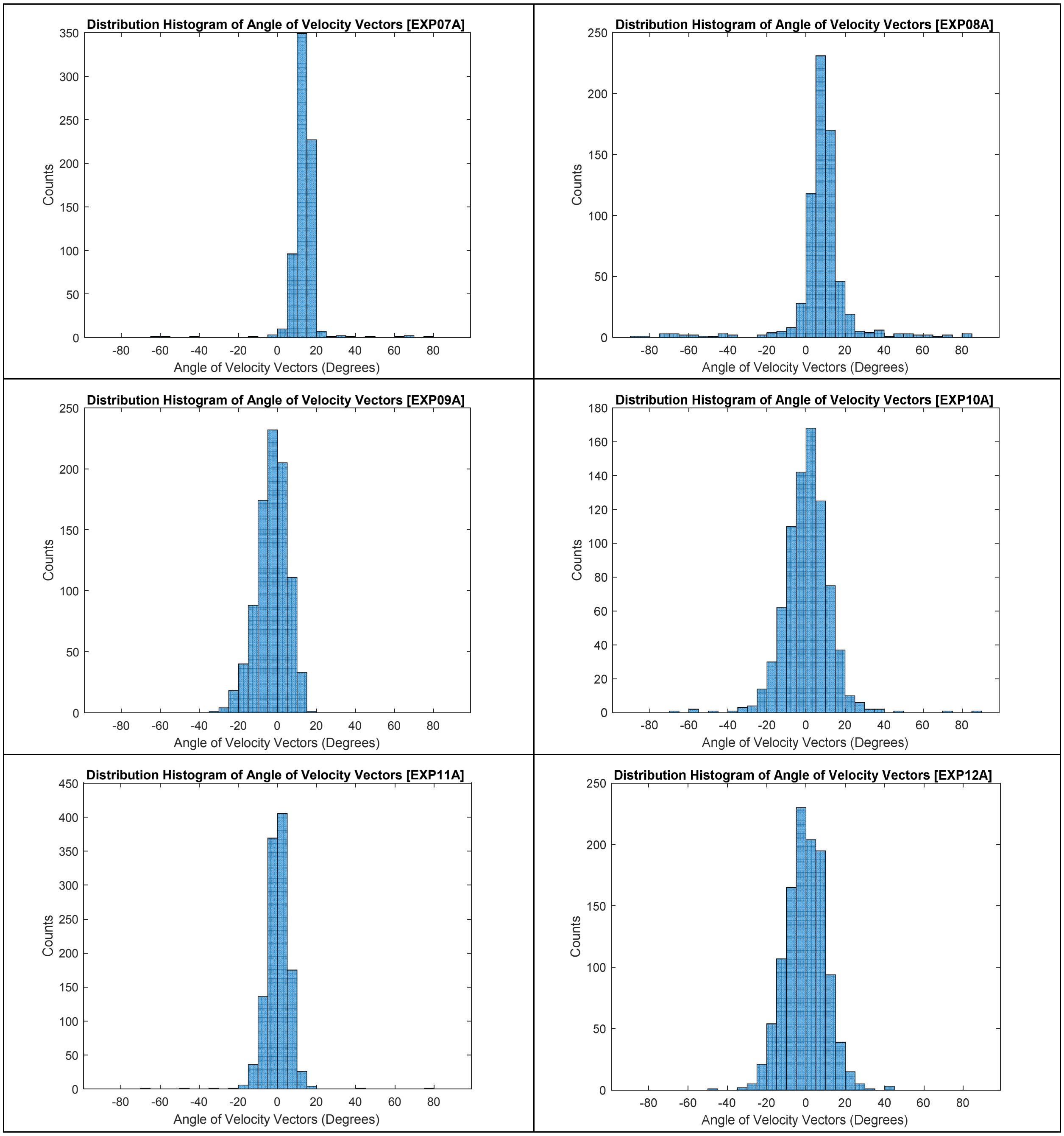

Figure 4.20 continued

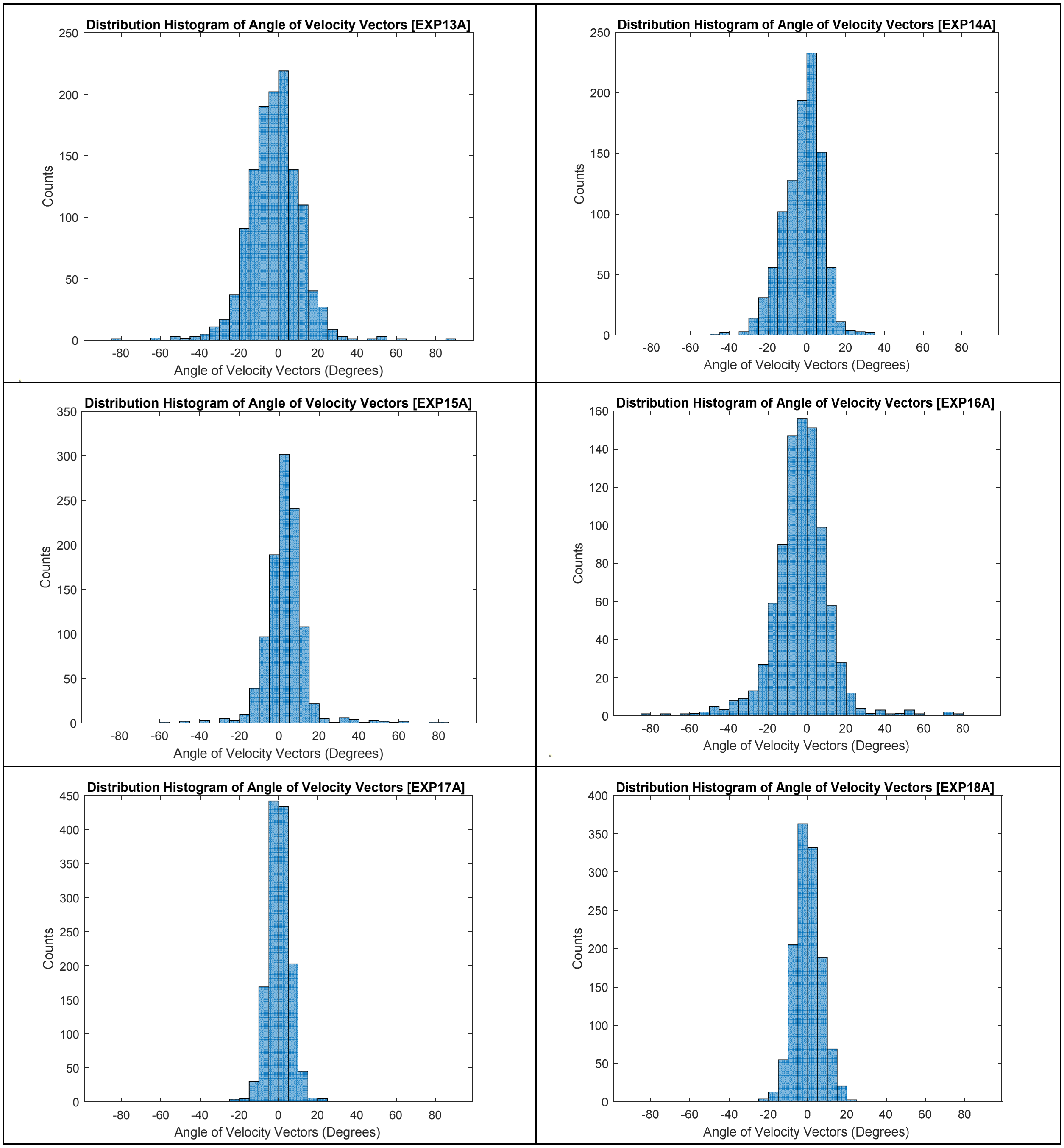

Figure 4.20 continued

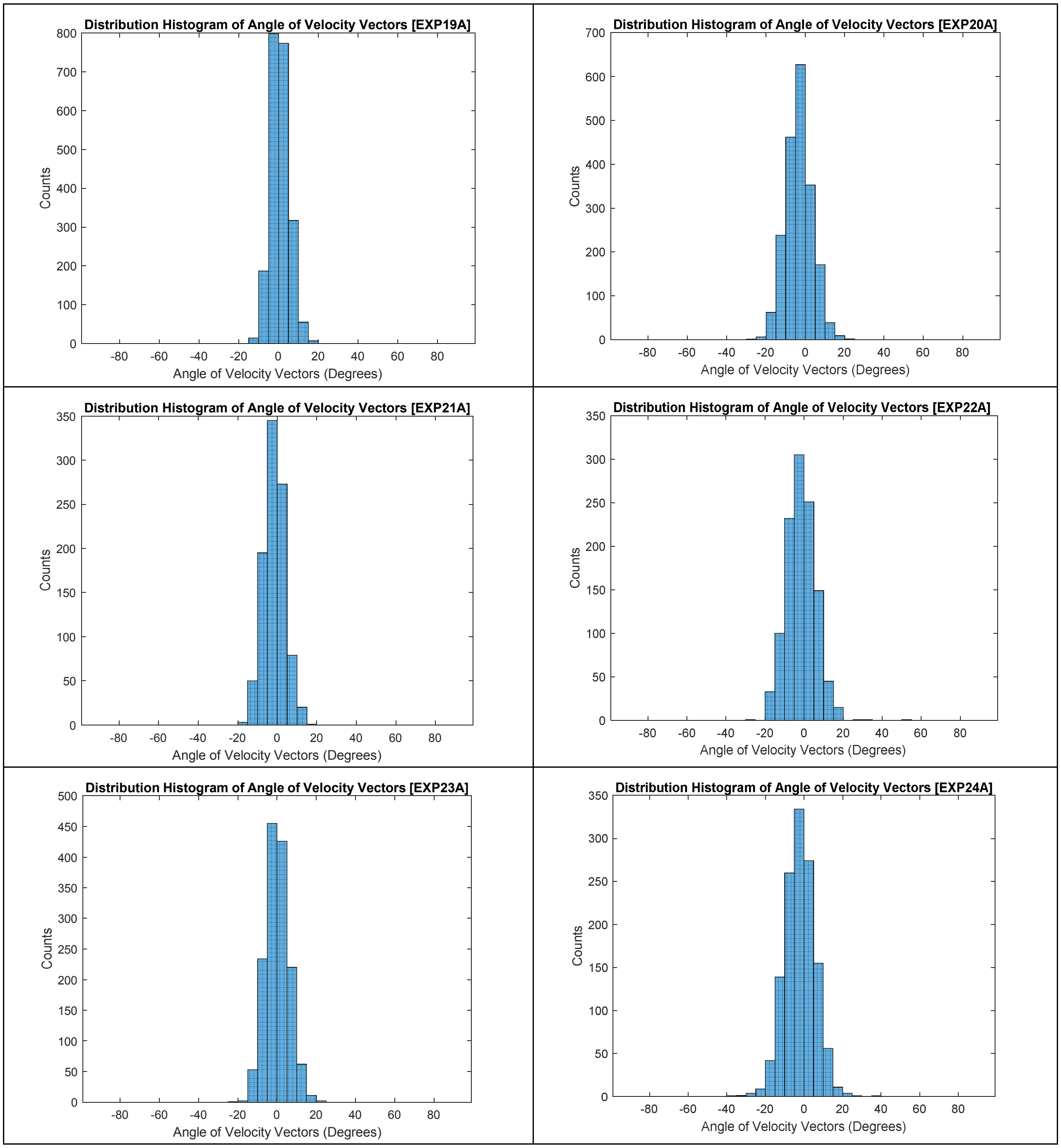

Figure 4.20 continued

4.4.3 Boxplot of Particle Velocity Range

This section summarizes boxplots of particle velocity magnitudes for all experiments considering effect of fracture intersection angle, fluid viscosity, fluid flow rate, and proppant volumetric concentration as shown in Figure 4.21.

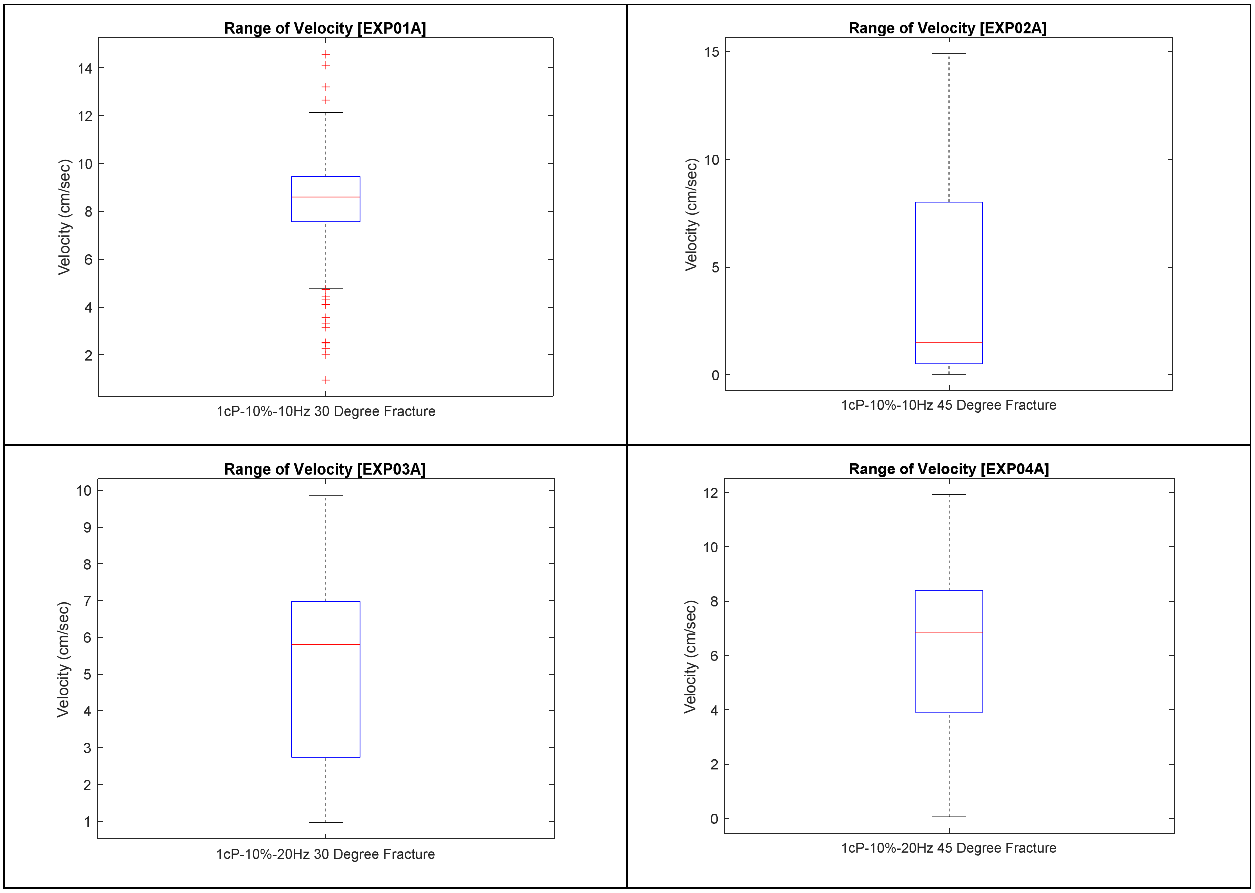

Figure 4.21 Boxplot of Velocity Magnitudes for Selected Regions by PIV Analysis for All Experiments

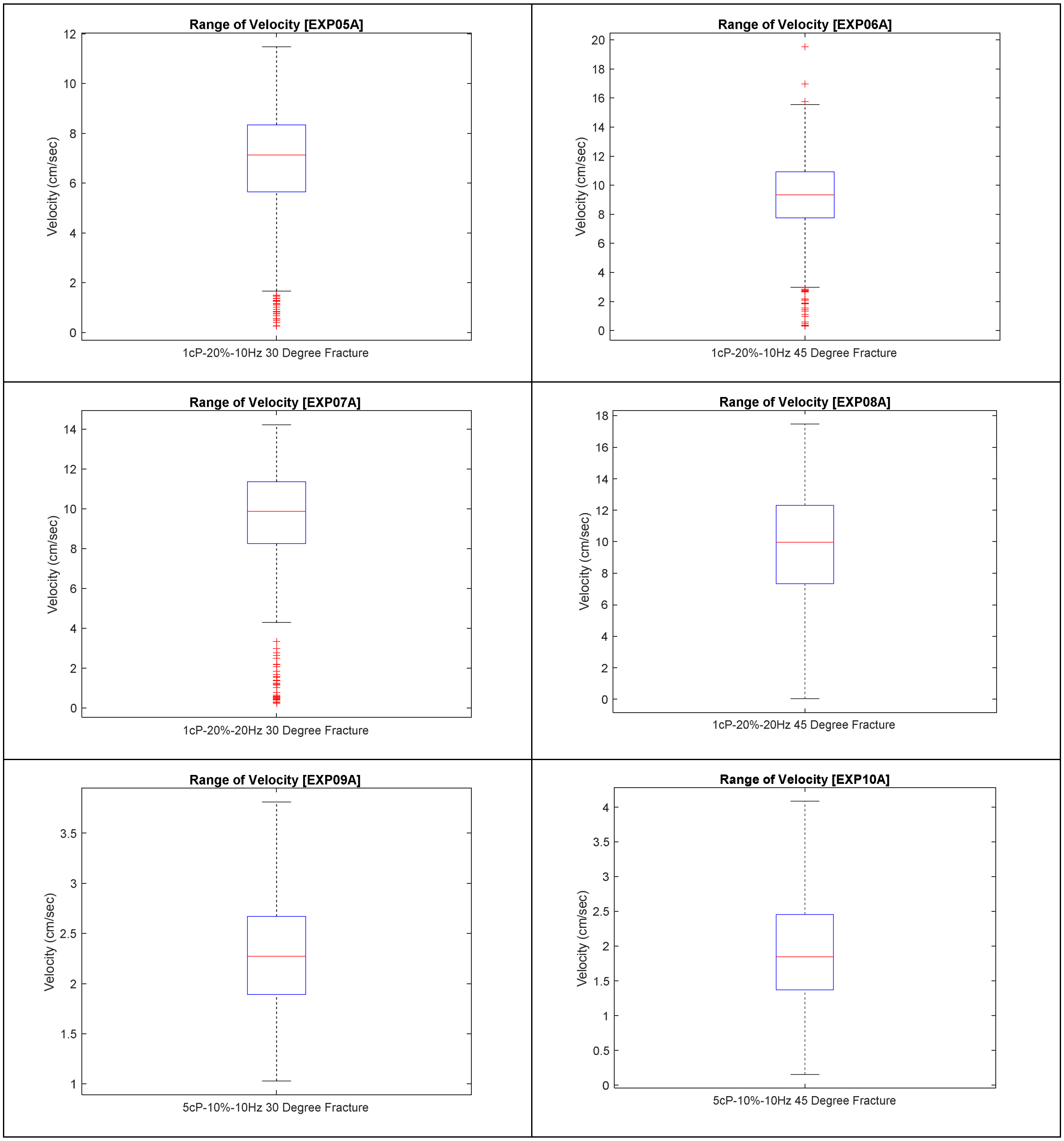

Figure 4.21 continued

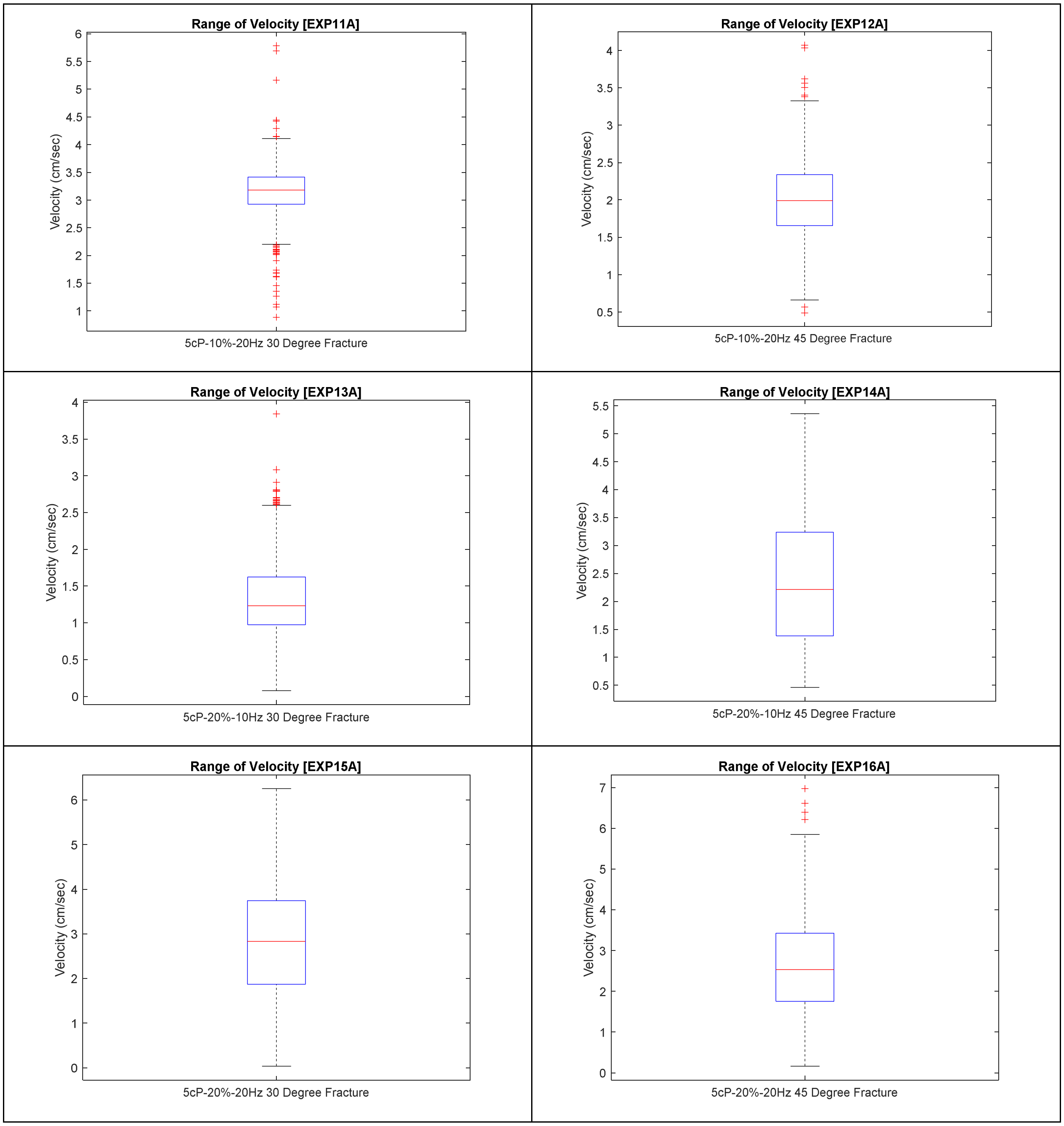

Figure 4.21 continued

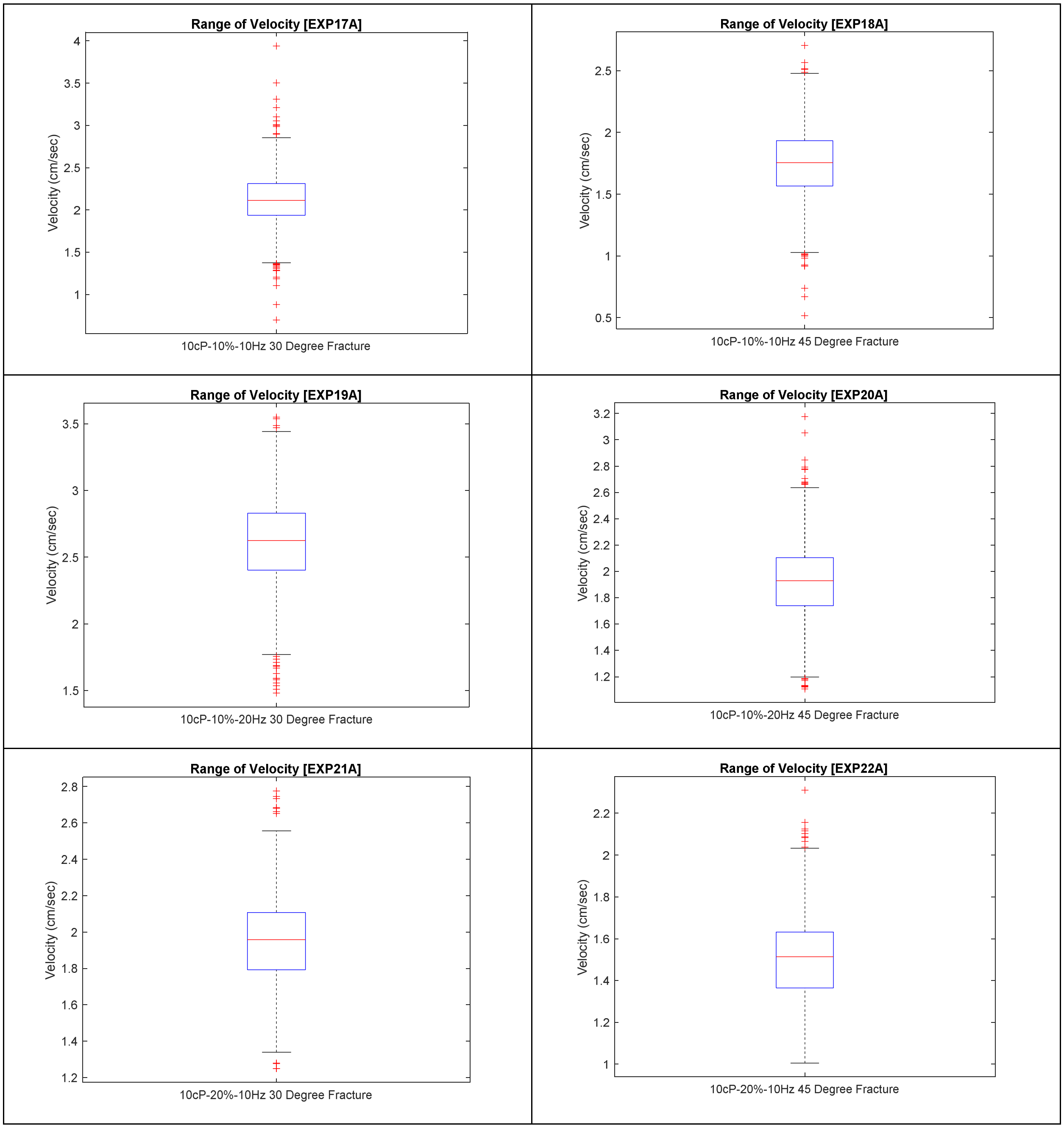

Figure 4.21 continued

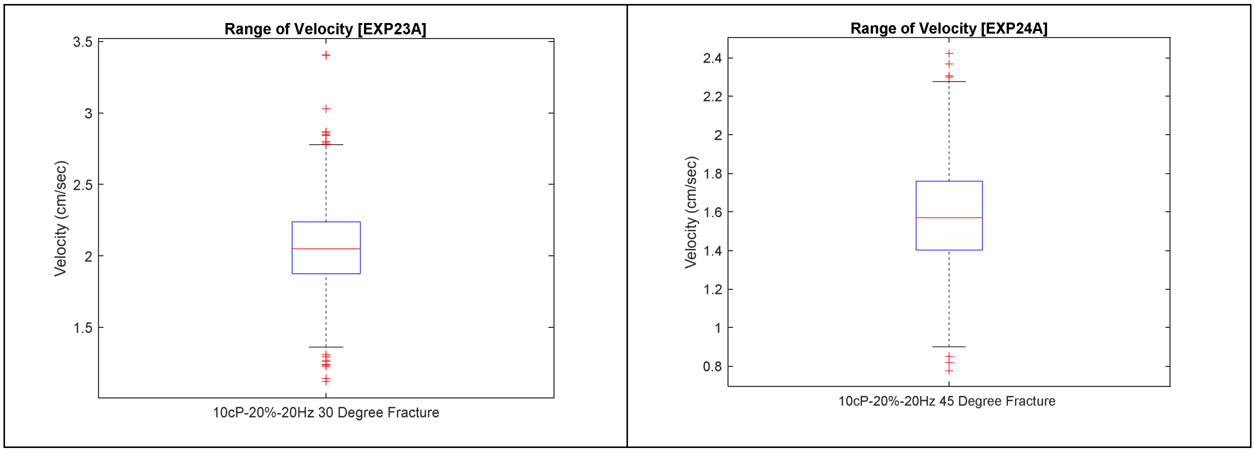

Figure 4.21 continued

4.5 Effect of Intersection Angle

4.5.1 Effect on Dune Slope

Fracture intersection angle has a strong effect on the linear fit slope across different fluid viscosities as shown in Figure 4.22. For 45° intersection, an increase of 0.001 Pa·s of fluid viscosity will cause an 1108° decrease in the linear fit slope. For 30° intersection, an increase of 0.001 Pa·s of fluid viscosity will cause an 827° decrease in the linear fit slope. Although this difference looks very close, 1108° versus 827°, it is pretty significant compared with the case considering the effect of the fracture intersection angle shown below. Also, an increasing in intersection angle from 30° to 45° will generally cause an increase of 2.1° in slope settlement angle.

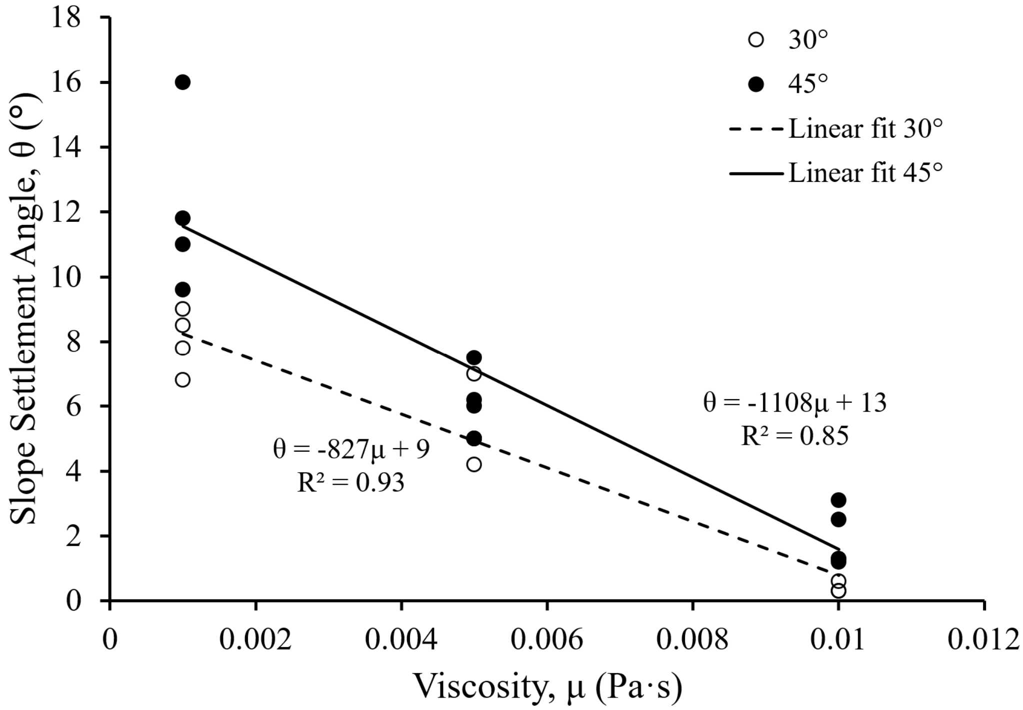

Figure 4.22 Effect of Fracture Intersection Angle under Different Fluid Viscosities

4.5.2 Effect on Particle Velocities

An increase in fracture intersection angles effectively reduces mean and median particle velocities after the intersection region, as shown in Table 4.1 and Figure 4.23. Generally, increasing intersection angle from 30° to 45° causes a decrease of mean and median particle velocities for about 20% to 30%, which is significant. However, the intersection angle increase causes local swirl effects by observing maximum velocity changes, since maximum velocities could increase up to 60% while it may also decrease to about 40%.

Table 4.1 Effect of Fracture Intersection Angle on Maximum, Mean and Median Velocity

	Max Velocity		Mean Velocity		Median Velocity	
	cm/sec	**% Difference**	**cm/sec**	**% Difference**	**cm/sec**	**% Difference**
01	15.82	-9.92%	7.76	-33.49%	7.92	-49.37%
02	14.25		5.16		4.01	
03	9.84	0.00%	5.79	-25.91%	6.80	-20.59%
04	9.84		4.29		5.40	
05	11.38	36.73%	8.43	-25.50%	8.87	-20.74%
06	15.56		6.28		7.03	
07	14.22	9.21%	9.69	-6.47%	10.11	-5.10%
08	15.53		9.07		9.59	
09	3.81	12.60%	1.87	-23.83%	1.75	-28.29%
10	4.29		1.42		1.26	
11	5.69	-38.31%	2.56	-37.77%	2.54	-40.04%
12	3.51		1.59		1.52	
13	3.84	60.68%	1.34	-14.93%	1.08	-23.26%
14	6.17		1.14		0.83	
15	5.87	18.91%	1.93	-19.66%	1.41	-27.30%
16	6.98		1.55		1.03	
17	3.50	-28.29%	1.98	-23.16%	1.96	-26.79%
18	2.51		1.52		1.44	
19	3.55	-10.42%	2.65	-28.05%	2.67	-29.03%
20	3.18		1.91		1.90	
21	2.78	-16.91%	1.82	-24.66%	1.80	-24.79%
22	2.31		1.37		1.35	
23	3.40	-24.71%	2.18	-28.01%	2.16	-29.17%
24	2.56		1.57		1.53	
Average		0.80%		-24.29%		-27.04%

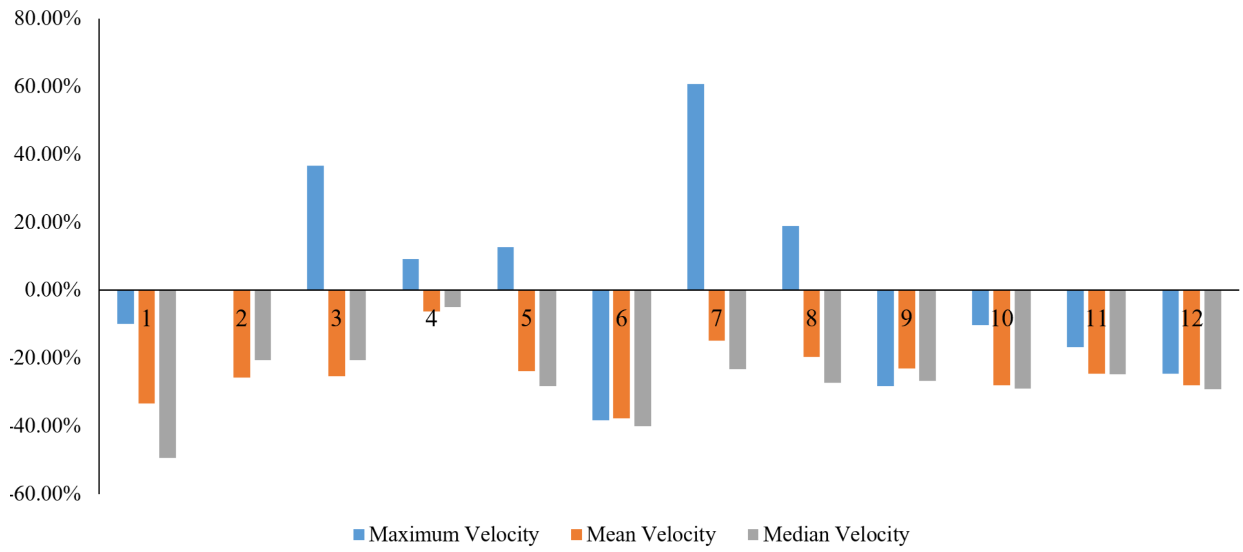

Figure 4.23 Velocity Change due to Increase of Fracture Intersection Angle

4.6 Effect of Proppant Volumetric Concentration

4.6.1 Effect on Dune Slope

Proppant particle volumetric concentration has a limited effect on settlement slope across different fluid viscosities, as shown in Figure 4.24. The linear fit slope of data changes from 844° to 824° for 10% to 20% volumetric particle concentrations, which is trivial compared with the effect of fracture intersection angle. Also, an increase in proppant concentration from 10% to 20% will averagely cause dune slope increase 0.2°. Under different combined conditions, the dune angle decreases down to 3.6°, while it can also increase up to 2.5°. There are 6 comparisons with increasing slope trend, 5 comparisons with decreasing trend, and 1 with no decreasing or increasing trend. Therefore, the effect of proppant concentration does not show very strong preference on settlement slope changing trend.

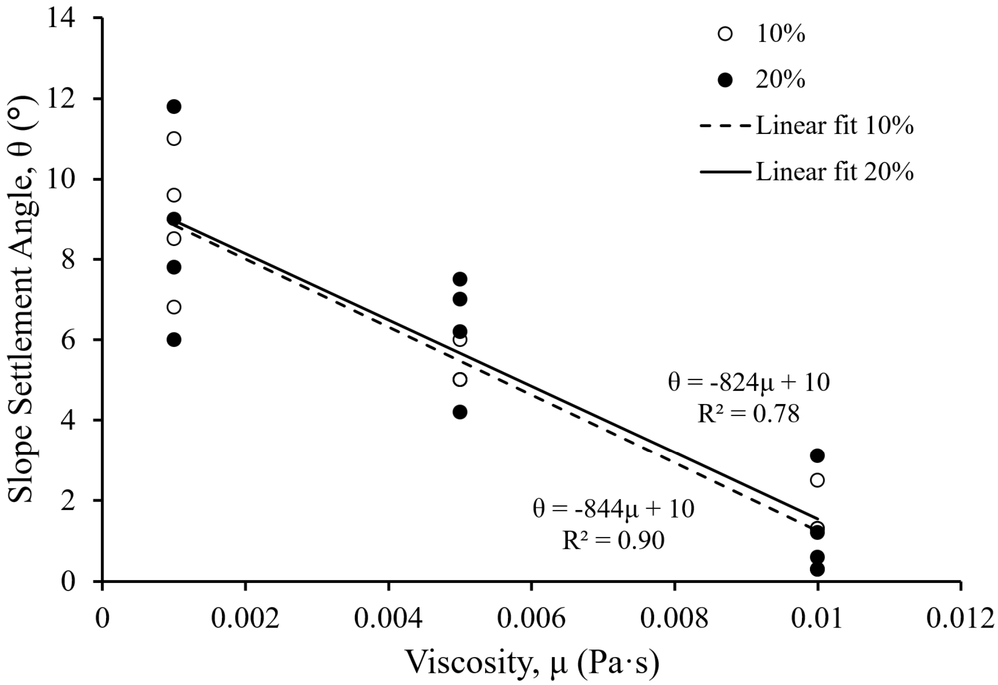

Figure 4.24 Effect of Proppant Volumetric Concentration on Dune Slope

When checking the combined effects of particle volumetric concentration and intersection angle, the intersection angle plays a dominant role in forming the dune slope compared to proppant volumetric concentration, as shown in Figures 4.25a to 4.25d. When considering two scenarios, the same intersection angle but difference concentration (Figures 4.25a and 4.25b) versus the same concentration but difference intersection angle (Figures 4.25c and 4.25d), the latter scenario has bigger differences in slope settlement by observing the inclination differences between fitted lines for each figure.

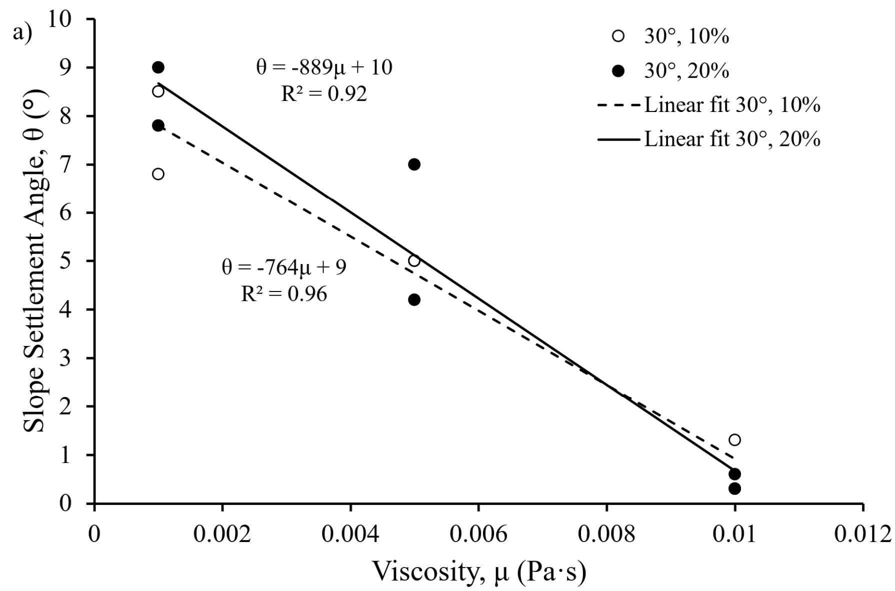

Figure 4.25a Combined Effect of Proppant Volumetric Concentration and 30° Fracture Intersection

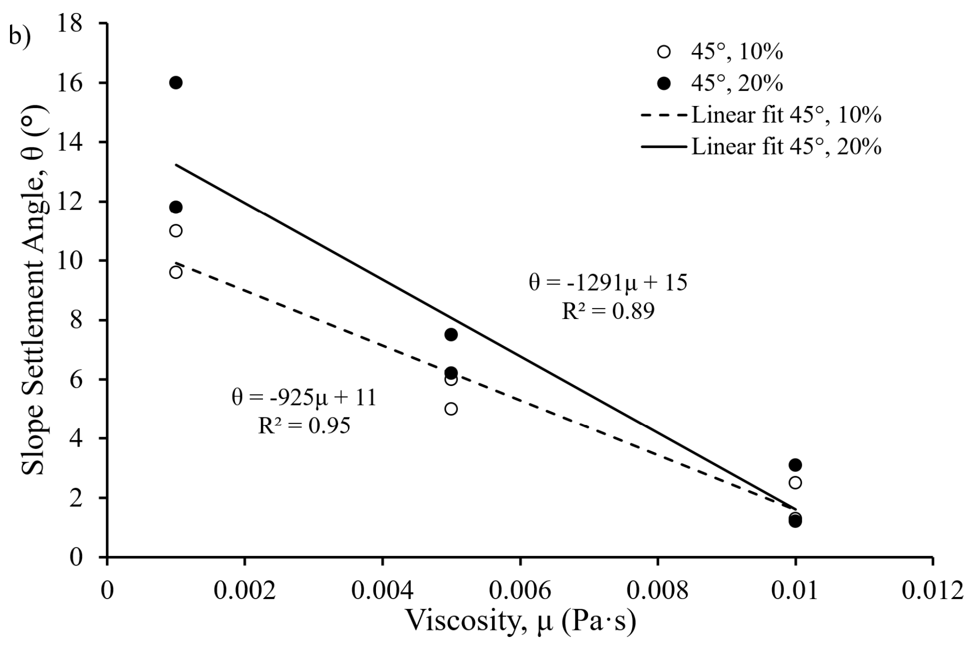

Figure 4.25b Combined Effect of Proppant Volumetric Concentration and 45° Fracture Intersection

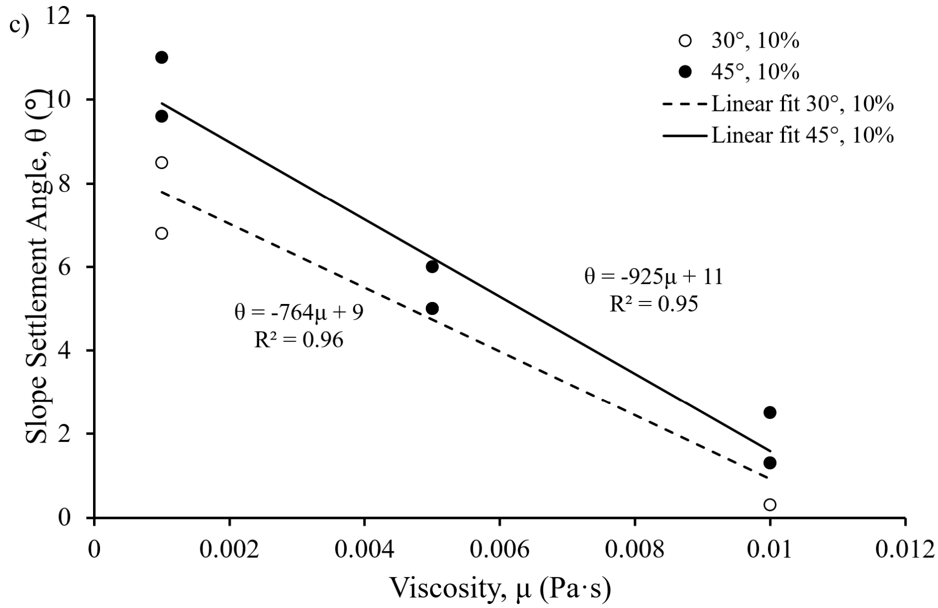

Figure 4.25c Combined Effect of 10% Proppant Volumetric Concentration and Fracture Intersection Angles

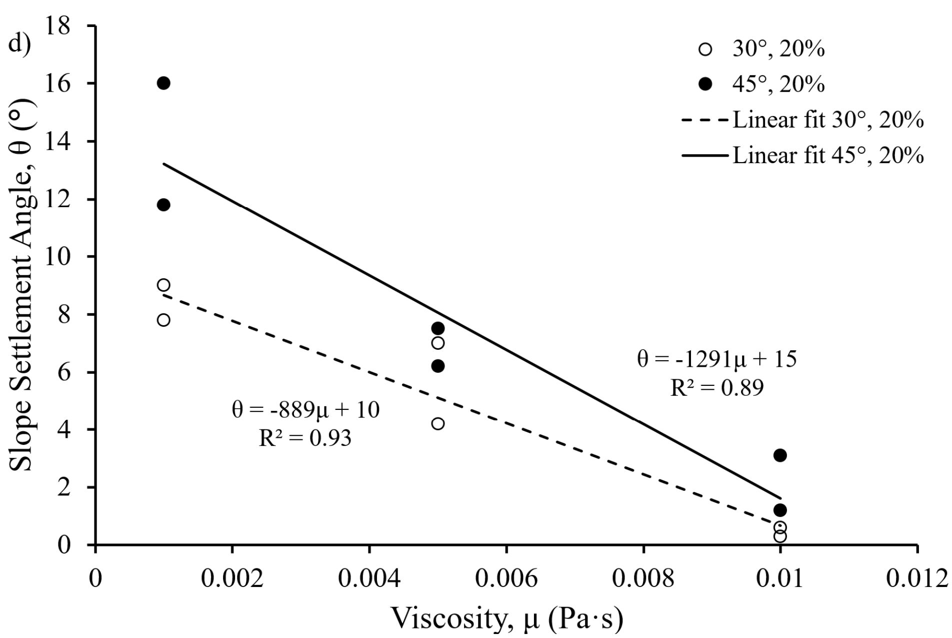

Figure 4.25d Combined Effect of 20% Proppant Volumetric Concentration and Fracture Intersection Angles

4.6.2 Effect on Particle Velocities

An increase in proppant volumetric concentration has a vague effect in maximum, mean, and median particle velocities as shown in Table 4.2 and Figure 4.26. An increase in proppant concentration from 10% to 20% causes both increase and decrease in maximum, mean, and median particle velocities. Most of the cases show decrease (about 10% to 35%) in velocity when proppant volumetric concentration increases, which is in accordance to previous findings. However, there are some extremely increased cases in our experiments, which push the average result towards velocity increase. On average, maximum velocities goes up 15%, mean velocity goes up 8.6%, and median velocity goes up 3%.

Table 4.2 Effect of Proppant Volumetric Concentration on Maximum, Mean and Median Velocity

	Max Velocity		**Mean Velocity**		**Median Velocity**	
	cm/sec	**% Difference**	**cm/sec**	**% Difference**	**cm/sec**	**% Difference**
1	15.82	-28.1%	7.76	-19.1%	7.92	-11.3%
5	11.38		6.28		7.03	
3	9.84	44.5%	4.29	125.8%	5.40	87.3%
7	14.22		9.69		10.11	
2	14.25	9.2%	5.16	63.5%	4.01	121.2%
6	15.56		8.43		8.87	
4	9.84	57.8%	5.79	56.6%	6.80	41.1%
8	15.53		9.07		9.59	
9	3.81	0.8%	1.87	-39.4%	1.75	-38.6%
13	3.84		1.13		1.08	
11	5.69	3.2%	2.56	-24.4%	2.54	-44.4%
15	5.87		1.93		1.41	
10	4.29	43.8%	1.42	-3.7%	1.26	-34.3%
14	6.17		1.37		0.83	
12	3.51	98.9%	1.59	-2.4%	1.52	-32.6%
16	6.98		1.55		1.03	
17	3.50	-20.57%	1.98	-8.10%	1.96	-8.42%
21	2.78		1.82		1.80	
19	3.55	-4.23%	2.65	-17.75%	2.67	-19.10%
23	3.40		2.18		2.16	
18	2.51	-7.97%	1.52	-9.88%	1.44	-5.92%
22	2.31		1.37		1.35	
20	3.18	-19.50%	1.91	-17.72%	1.90	-19.26%
24	2.56		1.57		1.53	
Average		14.8%		8.6%		3.0%

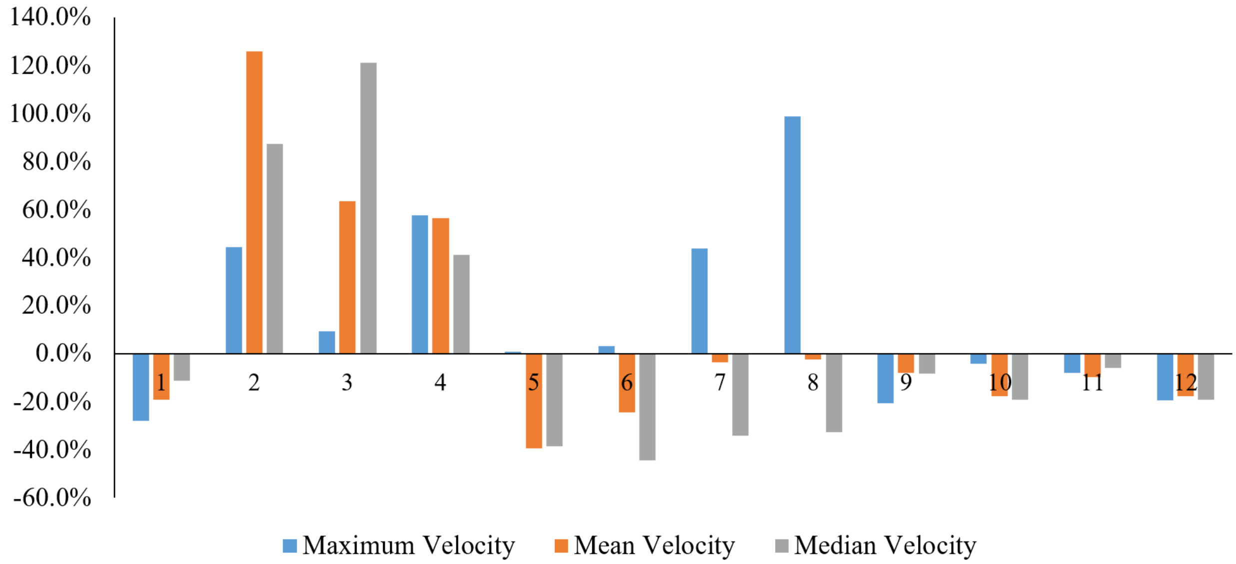

Figure 4.26 Velocity Change due to Increase of Proppant Volumetric Concentration

4.7 Effect of Flow Rate

4.7.1 Effect on Dune Slope

Flow rate has a clear effect on settlement slope across fluid viscosities as shown in Figure 4.27. For flow rate associated with 10 Hz pump rotor frequency has 870° decrease in the data linear fit slope and a 1064° for 20 Hz. Therefore, the flow rate significantly effects the fitted data. An increase in fluid flow rate will averagely cause an increase of 0.2° in the dune slope. Under different combined conditions, the slope settlement angle decreases down to 1.7°, while it can also increase up to 4.2°. There are 4 comparisons with increasing slope trend, 7 comparisons with decreasing trend, and 1 with no decreasing or increasing trend. Therefore, the effect of proppant concentration tends to indicate a flattening effect on dune slope.

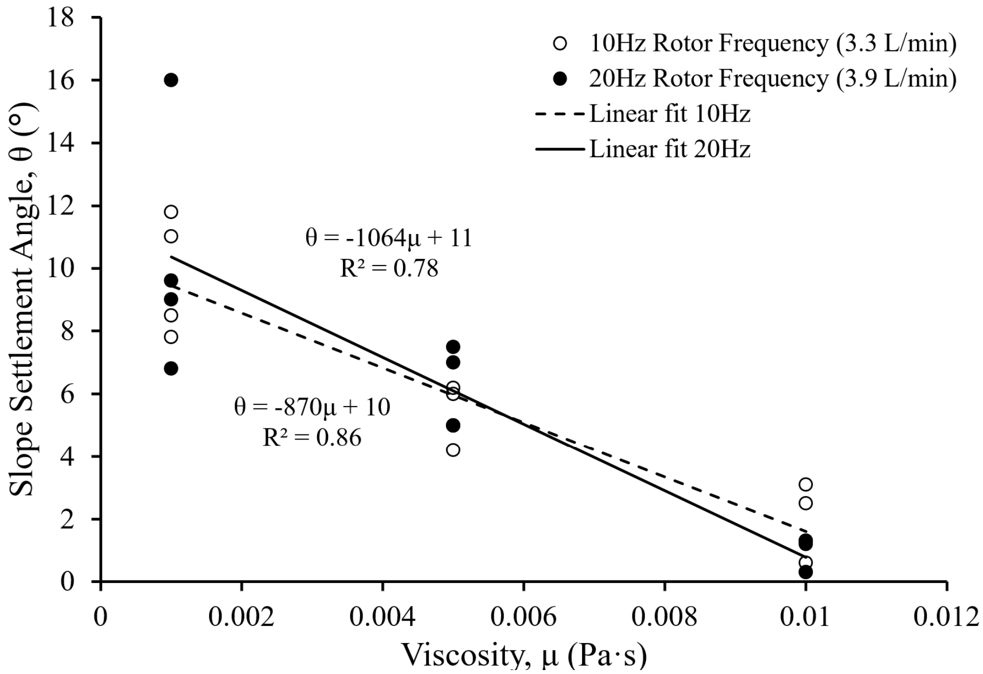

Figure 4.27 Effect of Fluid Flow Rate

When checking the combined effect of fluid flow rate and intersection angle, it is clear to see that the intersection angle helps to magnify the slope settlement as shown in Figures 4.28a to 4.28d below. When considering two scenarios, the same intersection but different flow rate (Figures 4.28a and 4.28b) vs. same flow rate but different intersection (Figures 4.28c and 4.28d), the latter case causes more significant differences in slope settlement by observing the inclination differences between fitted lines for each figure.

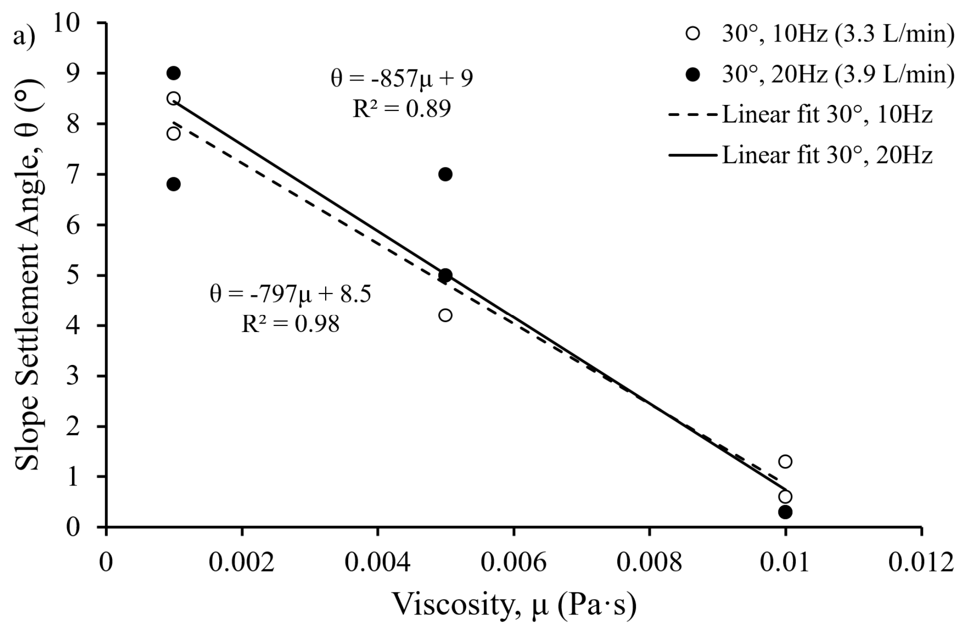

Figure 4.28a Combined Effect of Fluid Flow Rate and 30° Fracture Intersection

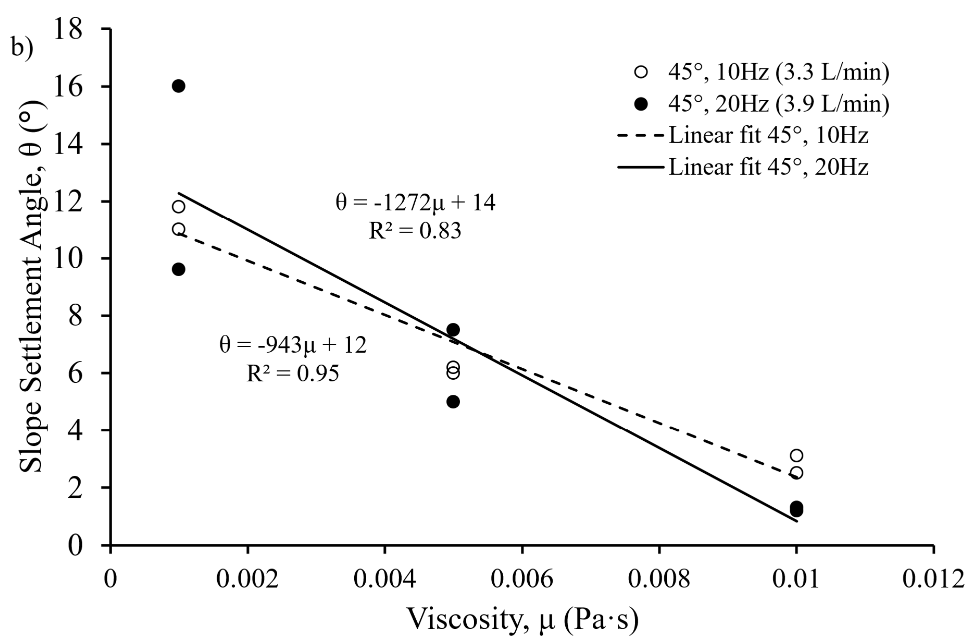

Figure 4.28b Combined Effect of Fluid Flow Rate and 45° Fracture Intersection

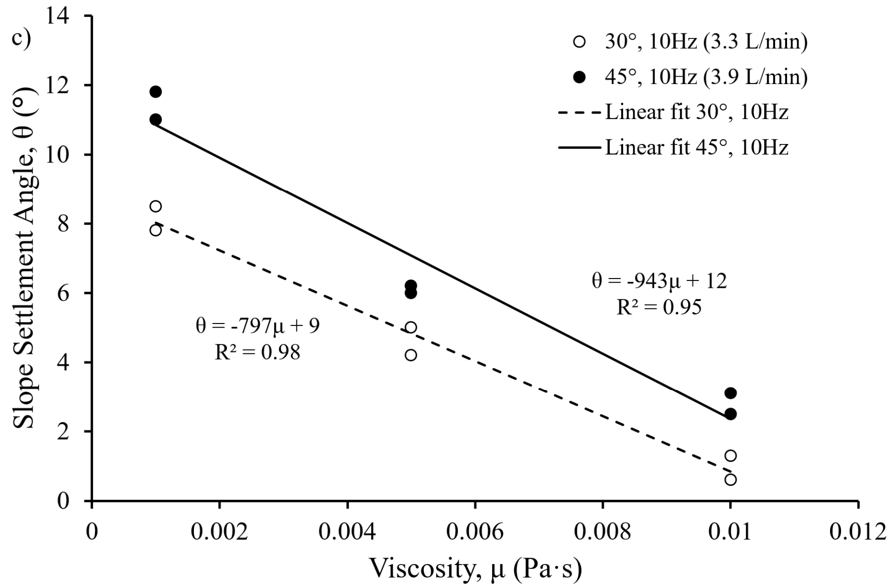

Figure 4.28c Combined Effect of Fluid Flow Rate at 10Hz Pump Rotor Rate and Fracture Intersection Angles

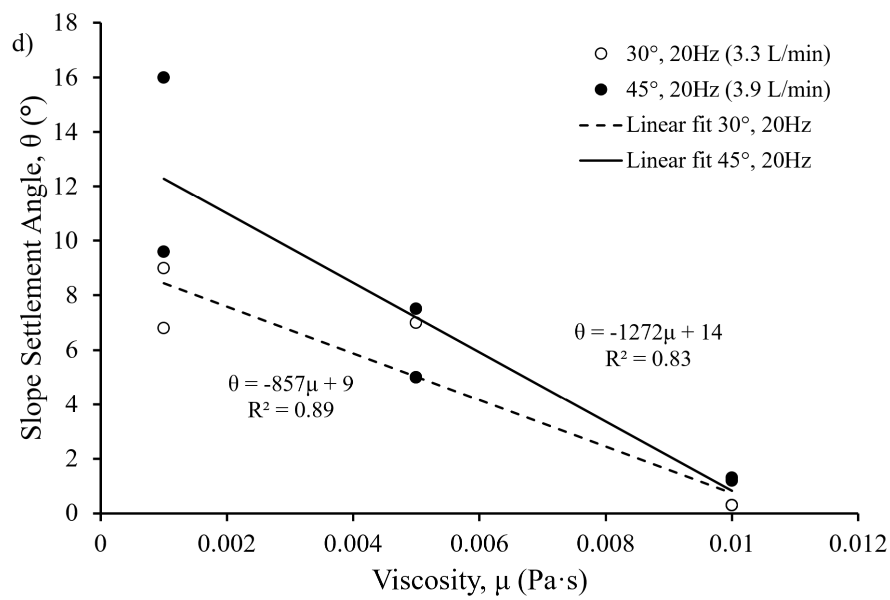

Figure 4.28d Combined Effect of Fluid Flow Rate at 20Hz Pump Rotor Rate and Fracture Intersection Angles

4.7.2 Effect on Particle Velocities

An increase in fluid flow rate will undoubtfully increase maximum, mean, and median particle velocities after the intersection region, as shown in Table 4.3 and Figure 4.29. Except for some experiments with decreasing effects, particle velocities general increases more than 20% for most of the experiments. In general, while eliminating the effects of proppant volumetric concentration, fracture intersection angle, and fluid viscosity, an increase in flow rate (pump rotor frequency from 10Hz to 20Hz, i.e. flow rate increases about 10% to 37%) will averagely cause maximum velocity increase 25%, mean velocity increase 27%, and median velocity increase 31%.

Table 4.3 Effect of Fluid Flow Rate on Maximum, Mean and Median Velocity

	Max Velocity		**Mean Velocity**		**Median Velocity**	
	cm/sec	**% Difference**	**cm/sec**	**% Difference**	**cm/sec**	**% Difference**
01	15.82	-37.8%	7.76	-44.6%	7.92	-31.9%
03	9.84		4.29		5.40	
05	11.38	25.0%	6.28	54.4%	7.03	43.8%
07	14.22		9.69		10.11	
02	14.25	-30.9%	5.16	12.3%	4.01	69.5%
04	9.84		5.79		6.80	
06	15.56	-0.2%	8.43	7.5%	8.87	8.1%
08	15.53		9.07		9.59	
09	3.81	49.3%	1.87	36.8%	1.75	44.9%
11	5.69		2.56		2.54	
13	3.84	52.9%	1.13	70.6%	1.08	31.2%
15	5.87		1.93		1.41	
10	3.51	22.2%	1.42	11.8%	1.26	21.1%
12	4.29		1.59		1.52	
14	6.17	13.1%	1.37	13.3%	0.83	24.2%
16	6.98		1.55		1.03	
17	3.50	1.43%	1.98	34.05%	1.96	36.22%
19	3.55		2.65		2.67	
21	2.78	22.30%	1.82	19.97%	1.80	20.33%
23	3.40		2.18		2.16	
18	2.51	26.69%	1.52	25.54%	1.44	32.06%
20	3.18		1.91		1.90	
22	2.31	10.82%	1.37	14.63%	1.35	13.33%
24	2.56		1.57		1.53	
Average		24.9%		27.4%		31.3%

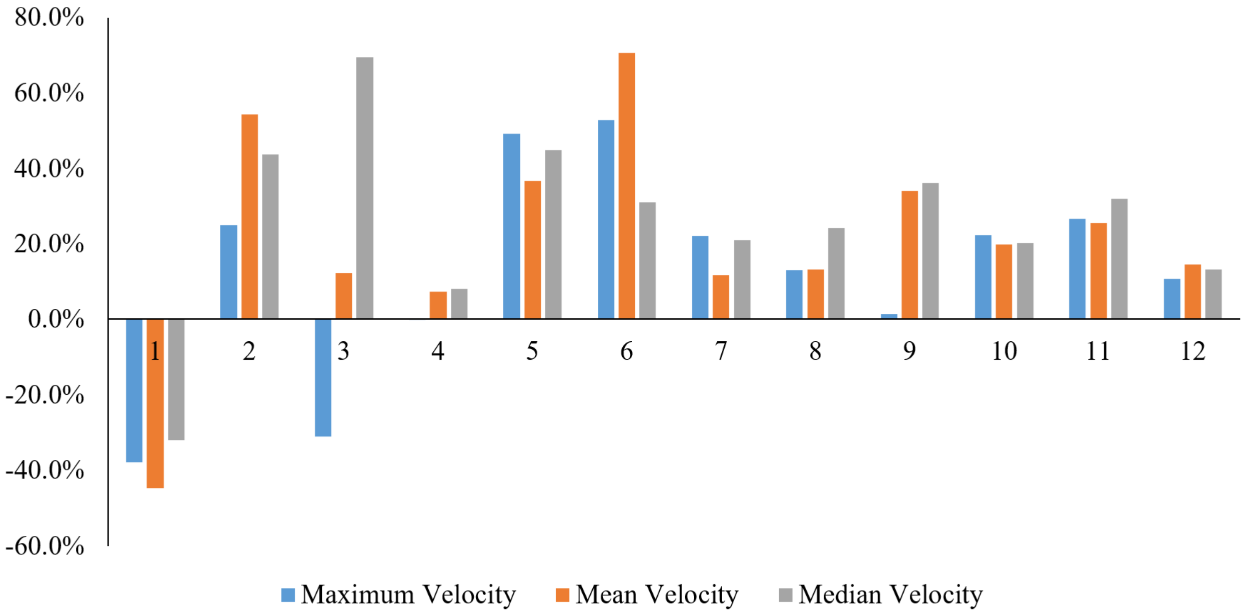

Figure 4.29 Velocity Change due to Increase of Fluid Flow Rate

4.8 Effect of Fluid Viscosity

4.8.1 Effect on Dune Slope

An increase of fluid viscosity will effectively flatten the slope settlement angle as shown in Figure 4.30. An increase of 0.001 Pa·s of fluid viscosity will cause a 967° decrease in linear-fit slope.

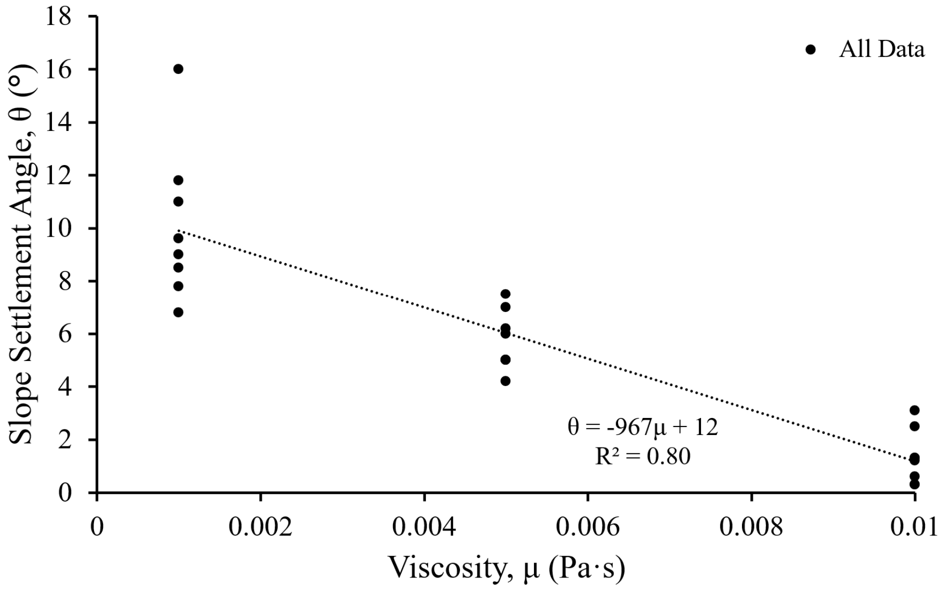

Figure 4.30 Effect of Fluid Viscosities on Dune Slope for All Experiments

4.8.2 Effect on Particle Velocities

An increase in fluid viscosity will effectively decrease particle maximum velocities as shown in Table 4.4. While within more viscous domain, the particle mean and median velocities may also increase a little bit as viscosity increases. Increase fluid viscosity will also cause flow vectors more horizontal.

Table 4.4 Effect of Fluid Viscosity on Maximum, Mean and Median Velocities

	Max Velocity		**Mean Velocity**		**Median Velocity**		**Mode Velocity Angle**
	cm/sec	**Trend**	**cm/sec**	**Trend**	**cm/sec**	**Trend**	**degree**
01	15.82	keep decreasing	7.76	decrease, then increase a little bit	7.92	decrease, then increase a little bit	(15,20)
09	3.81		1.87		1.75		(0,5)
17	3.50		1.98		1.96		(0,5)
03	9.84	keep decreasing	4.29	decrease, then increase a little bit	5.40	decrease, then increase a little bit	(15,20)(20,25)
11	5.69		2.56		2.54		(0,5)
19	3.55		2.65		2.67		(0,5)
05	11.38	keep decreasing	6.28	decrease, then increase	7.03	decrease, then increase	(10,15)
13	3.84		1.13		1.08		(0,5)
21	2.78		1.82		1.80		(0,5)
07	14.22	keep decreasing	9.69	decrease, then increase a little bit	10.11	decrease, then increase	(10,15)
15	5.87		1.93		1.41		(0,5)
23	3.40		2.18		2.16		(0,5)
02	14.25	keep decreasing	5.16	decrease, then increase a little bit	4.01	decrease, then increase a little bit	(15,20)
10	4.29		1.42		1.26		(0,5)
18	2.51		1.52		1.44		(0,5)
04	9.84	keep decreasing	5.79	decrease, then increase	6.80	decrease, then increase	(15,20)(20,25)
12	3.51		1.59		1.52		(0,5)
20	3.18		1.91		1.90		(0,5)
06	15.56	keep decreasing	8.43	decrease, then remain same	8.87	decrease, then increase	(10,15)
14	6.17		1.37		0.83		(0,5)
22	2.31		1.37		1.35		(0,5)
08	15.53	keep decreasing	9.07	decrease, then remain same	9.59	decrease, then increase	(5,10)
16	6.98		1.55		1.03		(0,5)
24	2.56		1.57		1.53		(0,5)

4.9 Correlation between Settlement Slope and Proppant Transportation Velocity

4.9.1 Correlation Involved with Reynolds Number

Slope settlement slope has a logarithmic relationship with particle Reynolds number. The suggested relationships are provided below:

$$Slope(^\circ) = 1.757(^\circ) * \ln(Re) + 3.647(^\circ) \quad \text{for } 30^\circ \text{ intersection} \tag{7a}$$

$$Slope(^\circ) = 2.648(^\circ) * \ln(Re) + 5.865(^\circ) \quad \text{for } 45^\circ \text{ intersection} \tag{7b}$$

The correlation is also shown in Figure 4.31. As particle Reynolds number increases, the settlement slope angle increases accordingly. Also, a higher fracture intersection angle will cause more effect on the slope settlement angle as the particle Reynolds number increases.

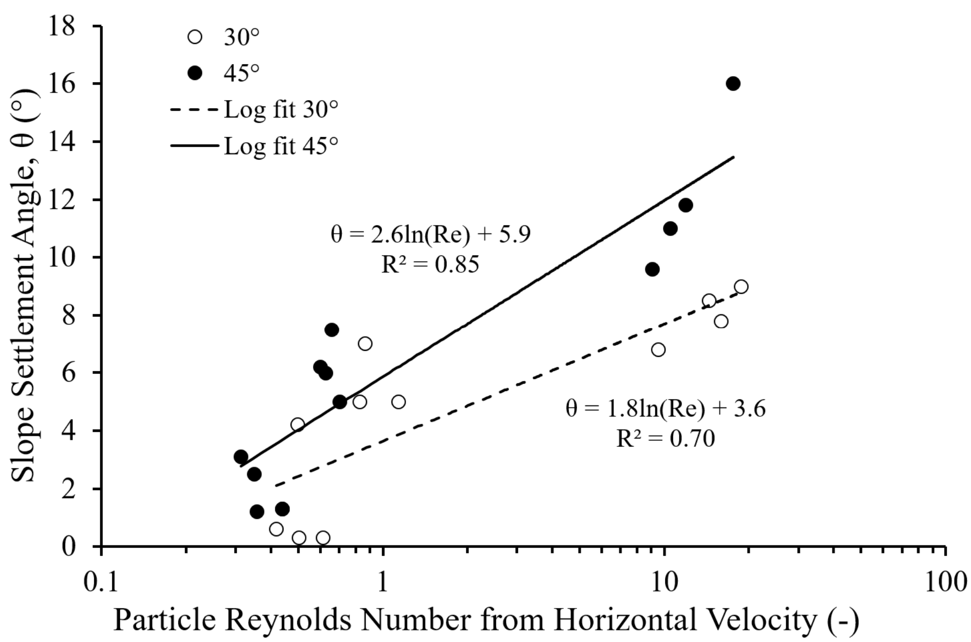

Figure 4.31 Relationship between Dune Slope and Particle Reynolds Number from Horizontal Velocity

4.9.2 Correlation Involved with Stokes Number

Settlement slope also has a logarithmic relationship with particle vertical Stokes number. Suggested relationships are provided below:

$$\text{Slope}\,(^\circ) = 1.013(^\circ)\cdot \ln(St) + 12.02(^\circ) \quad for\ 30^\circ\ intersection \tag{8a}$$

$$\text{Slope}\,(^\circ) = 1.865(^\circ)\cdot \ln(St) + 20.34(^\circ) \quad for\ 45^\circ\ intersection \tag{8b}$$

The correlation is also shown in Figure 4.32. As particle Stokes number increases, the settlement slope angle increases accordingly. Also, a higher fracture intersection angle will cause more effect on the slope settlement angle as the particle Stokes number increases.

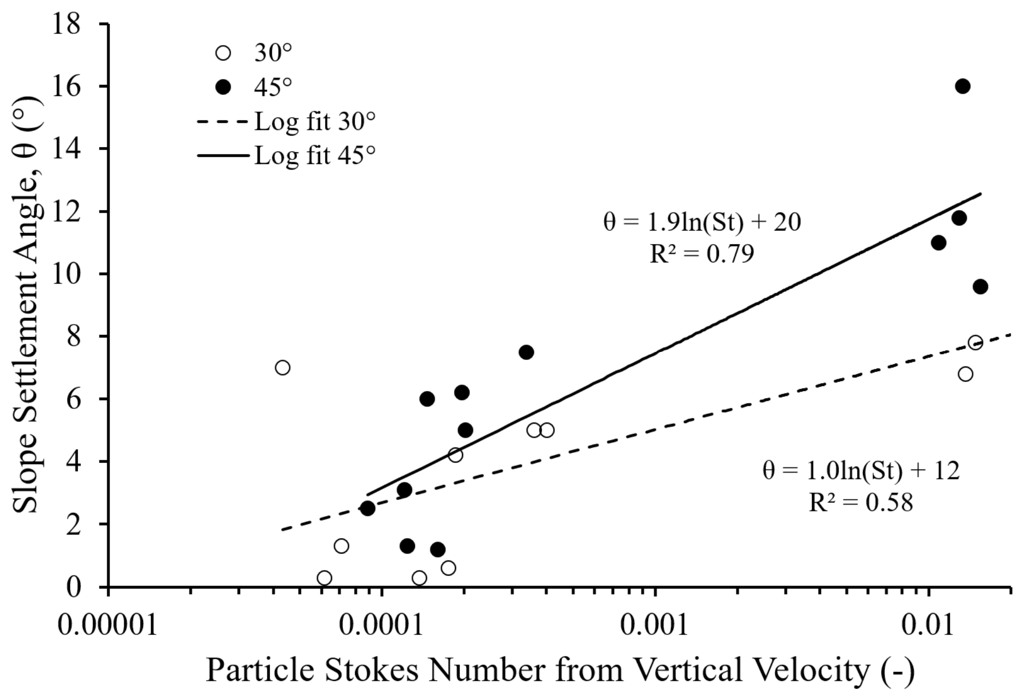

Figure 4.32 Relationship between Dune Slope and Particle Stokes Number from Vertical Velocity

4.9.3 Correlation Involved with Particle Velocity Direction

Supplemental to finding the correlation between the dune slope angle and an average particle velocity, it is also interesting to examine the correlation between the dune slope angle and an average particle velocity direction under the effect of fracture intersection angle. Particle velocity direction is compared relative to the horizontal level. A positive number is counted in a clockwise direction. As shown in Figure 4.33, a higher fracture intersection angle will cause a stronger effect on the dune slope angle as the average particle velocity direction increases. As particle velocity direction increases, the settlement slope angle also increases.

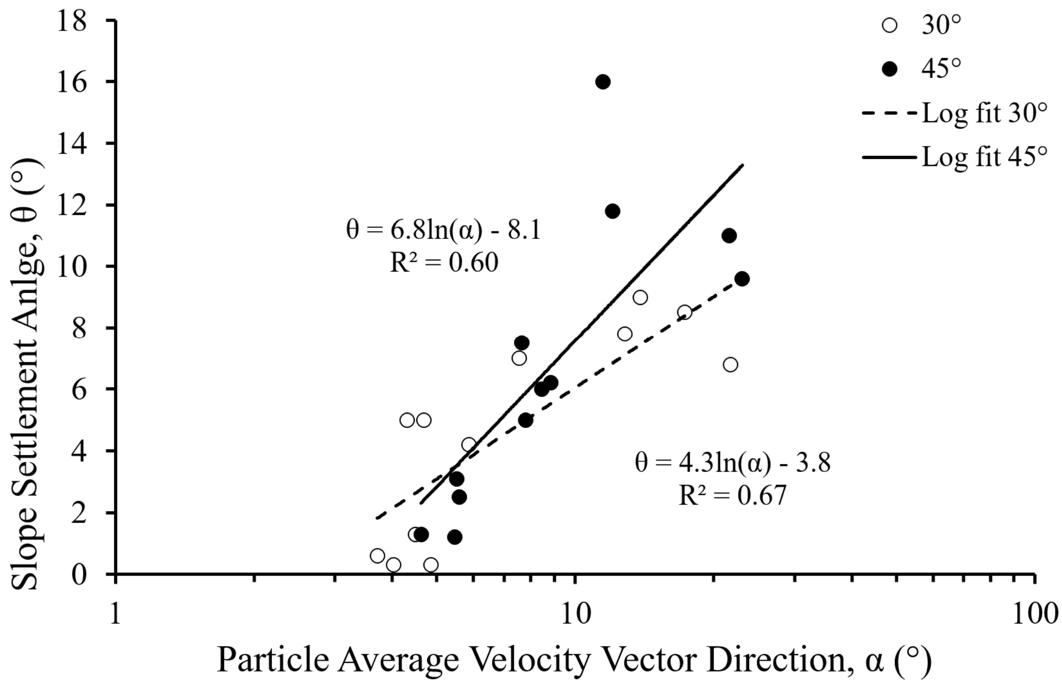

Figure 4.33 Relationship between Dune Slope and Average Particle Velocity Direction

Chapter 5: CONCLUSIONS

The study uses plexiglas laboratory slot experiments enhanced with advanced image analysis for identifying particle trajectories and quantifying slurry velocities. GeoPIV analysis helps to visualize the particle flow in the fracture and find correlation between settlement slope, particle velocity and velocity direction. GeoPIV enable us to quantify effects of intersection angle, coupled with fluid viscosity, fluid flow rate, and proppant volumetric concentration on proppant velocities. Also, this study aims to find a correlation between particle velocity and dune slope.

Fracture intersection angle has a strong effect on proppant transport and settlement. Higher fracture intersection angle will generally induce a steeper dune after the intersection. An increasing in intersection angle from 30° to 45° will cause an increase of 2.1° in dune slope. Higher fracture intersection angle will generally decrease mean and median particle velocity, while creating different effects on maximum velocity. An increase in intersection angle from 30° to 45° causes a decrease of mean and median particle velocities for about 20% to 30%, which is significant. Maximum velocities could increase up to 60% while it may also decrease to about 40%, which suggests local eddies could have occurred.

Changes in proppant concentration have relatively vague effect on slope settlement and particle velocities compared with fluid flow rate. However, intersection angle will help to activate that effect. An increase of proppant volumetric concentration from 10% to 20% causes only 0.2° on average increase dune slope. However, among all 12 comparisons, a change in proppant volumetric concentration has a more balanced preference on increasing or decreasing trend in dune slope, unlike fluid flow rate. Mean, median and maximum particle velocities recorded in experiments show conflicting and varied values, such as are increase up to about 100% and decrease down to about 40% at higher proppant concentrations. Variations in velocities and the observed swirls suggest that the higher proppant concentration may cause more particle collisions and fluid-particle coupled effects.

Fluid flow rate effects on the slope settlement and particle velocities are more significant than the proppant concentration effects. Higher fluid flow rate results in clear change of the dune slope. Besides, fracture intersection angle will help to make this effect more significant. An increase in fluid flow rate (pump rotor frequency from 10 Hz to 20 Hz) will averagely cause an increase of 0.2° in slope settlement. However, among all 12 comparisons, a change in fluid flow rate has decreasing-biased effect on settlement slope, unlike proppant concentration. An increase in fluid flow rate increases maximum, median, and mean particle velocities for 25%, 31%, and 27% respectively.

Fluid viscosity effect flattens the proppant dune slope in exit branch after intersected fracture and helps to transport proppant further. However, fracture intersection angle increase counter-balances this flattening effect. Particle velocities significantly decrease under lower viscosity range, while they will remain similar or increase slightly under higher viscosity range.

Particle agglomerations are not easily observed for proppant with small particle sizes, such as in this study. However, particle agglomerations are more clearly observed under higher fluid viscosities and proppant concentrations. The shape of clusters are highly varied from more rounded shape to a more angular shape. Variation of eclipse shape is the most common observed shape. For some of experiments with medium viscosity and all experiments with high viscosities, fluid with less proppant concentration will flow above fluid with higher proppant concentration with a clearly observed boundaries, although fluid has been mixed evenly in the storage bucket and pumped into the fracture.

References:

1. Aimene YE, Ouenes A. Geomechanical modeling of hydraulic fractures interacting with natural fractures — Validation with microseismic and tracer data from the Marcellus and Eagle Ford. *Interpretation*. 2015; 3(3). doi:10.1190/int-2014-0274.1

2. Alotaibi MA, Miskimins JL. Slickwater proppant transport in complex fractures: New experimental findings and scalable correlation. *SPE Annual Technical Conference and Exhibition*. 2015. doi:10.2118/174828-ms

3. Bec J, Celani A, Cencini M, Musacchio S. Clustering and collisions of heavy particles in random smooth flows, *Physics of Fluids*. 2005; 17. https://doi.org/10.1063/1.1940367

4. Chang O, Dilmore R, Wang JY. Model development of proppant transport through hydraulic fracture network and parametric study. *Journal of Petroleum Science and Engineering*. 2017;150: 224 - 237. doi:10.1016/j.petrol.2016.12.003

5. Cheng N-S. Formula for the viscosity of a glycerol−water mixture. *Industrial and Engineering Chemistry Research*. 2008; 47(9): 3285-3288. doi:10.1021/ie071349z

6. Dayan A, Stracener SM, Clark PE. Proppant transport in slickwater fracturing of shale gas formations. *SPE Annual Technical Conference and Exhibition*. 2009. doi:10.2118/125068-ms

7. Fiabane L, Zimmermann R, Volk R, Pinton JF, Bourgoin M. Clustering of finite-size particles in turbulence, *Physical Review E*, 2012; 86(3). https://link.aps.org/doi/10.1103/PhysRevE.86.035301

8. Fjaestad D, Tomac I. Experimental investigation of sand proppant particles flow and transport regimes through narrow slots. *Powder Technology*. 2019; 343: 495-511. doi:10.1016/j.powtec.2018.11.004

9. Frash LP, Hampton J, Gutierrez M, Tutuncu A, Carey JW, Hood J, Mokhtari M, Huang H, Mattson E. Patterns in complex hydraulic fractures observed by true-triaxial experiments and implications for proppant placement and stimulated reservoir volumes. *Journal of Petroleum Exploration and Production Technology*. 2019; 9(4): 2781-2792. doi:10.1007/s13202-019-0681-2

10. El Ghoraiby M, Park H, Manzari MT. Physical and mechanical properties of Ottawa F65 sand. In: Kutter B, Manzari M, Zeghal M, eds. *Model Tests and Numerical Simulations of Liquefaction and Lateral Spreading*. Springer, Cham; 2020. https://doi.org/10.1007/978-3-030-22818-7_3

11. Guala M, Liberzon A, Hoyer K, Tsinober A, Kinzelbach W. Experimental study on clustering of large particles in homogeneous turbulent flow. *Journal of Turbulence*. 2008; 9. doi: 10.1080/14685240802441118

12. Gualtieri P, Picano F, Casciola CM. Anisotropic clustering of inertial particles in homogeneous shear flow. *Journal of Fluid Mechanics*. 2009; 629: 25-39. doi:10.1017/S002211200900648X

13. Gustavsson K, Vajedi S, Mehlig B. Clustering of particles falling in a turbulent flow, *Physical Review Letters*. 2014; 112(21). https://link.aps.org/doi/10.1103/PhysRevLett.112.214501

14. Hampton J, Gutierrez M, Frash L. Predictions of macro-scale fracture geometries from acoustic emission point cloud data in a hydraulic fracturing experiment. *Journal of Petroleum Exploration and Production Technology*. 2019; 9(2): 1175-1184. doi:10.1007/s13202-018-0547-z

15. Ho CA, Sommerfeld M, Modelling of micro-particle agglomeration in turbulent flows, *Chemical Engineering Science*. 2002; 57(15): 3073-3084. https://doi.org/10.1016/S0009-2509(02)00172-0.

16. Kesireddy VR. *Quantifying ceramic proppant transport in complex fracture networks [master thesis]*. Rolla, Missouri: Missouri University of Science and Technology. 2017.

17. Kou R, Moridis GJ, Blasingame T. Field scale proppant transport simulation and its application to optimize stimulation strategy. *Proceedings of the 6th Unconventional Resources Technology Conference*. 2018. doi:10.15530/urtec-2018-2878230

18. Kumar D, Ghassemi A. Modeling and analysis of proppant transport and deposition in hydraulic/natural fracture networks. *Proceedings of the 7th Unconventional Resources Technology Conference*. 2019. doi:10.15530/urtec-2019-243

19. Li N, Li J, Zhao L, Luo Z, Liu P, Guo Y. Laboratory testing and numeric simulation on laws of proppant transport in complex fracture systems. *SPE Asia Pacific Hydraulic Fracturing Conference*. 2016. doi:10.2118/181822-ms

20. Li S, Marshall JS, Liu G, Yao Q. Adhesive particulate flow: The discrete-element method and its application in energy and environmental engineering. *Progress in Energy and Combustion Science*. 2011; 37(6): 633-668. https://doi.org/10.1016/j.pecs.2011.02.001.

21. Lund JW, Bertani R, Boyd TL. Worldwide geothermal energy utilization 2015. *GRC Transactions*. 2015; 39.

22. Luo L, Tomac I. Experimental investigation of particle agglomeration effects on slurry settling in viscous fluid. *Transport in Porous Media*. 2018; 121(2): 333-352. doi:10.1007/s11242-017-0956-3

23. Luo L, Tomac I. Particle image velocimetry (PIV) analysis of particle settling in narrow fracture experiments. *Geotechnical Testing Journal*. 2018; 41(2): 354-370. doi:10.1520/gtj20170136

24. Nandlal K, Weijermars R. Drained rock volume around hydraulic fractures in porous media: planar fractures versus fractal networks. *Petroleum Science*. 2019; 16(5): 1064-1085. doi:10.1007/s12182-019-0333-7

25. Pan L, Zhang Y, Cheng L, Lu Z, Kang Y, He P, Dong B. Migration and distribution of complex fracture proppant in shale reservoir volume fracturing. *Natural Gas Industry B*. 2018; 5(6): 606-615. doi:10.1016/j.ngib.2018.11.009

26. Raiskinmäki P, Aström JA, Kataja M, Latva-Kokko M, Koponen A, Jasberg A, Shakib-Manesh A, Timonen J. Clustering and viscosity in a shear flow of a particulate suspension. *Physical Review E*. 2003; 68: 061403. doi:10.1103/PhysRevE.68.061403

27. Reeks MW. Transport, mixing and agglomeration of particles in turbulent flows. *Journal of Physics: Conference Series*. 2014; 530. doi:10.1088/1742-6596/530/1/012003

28. Reynolds O. An experimental investigation of the circumstances which determine whether the motion of water shall be direct or sinuous, and of the law of resistance in parallel channels. *Philosophical Transactions of the Royal Society*. 1883; 174: 935–982. Bibcode:1883RSPT..174..935R. doi:10.1098/rstl.1883.0029. JSTOR 109431.

29. Rhodes M. Introduction to Particle Technology. Wiley. 1989. ISBN 978-0-471-98482-5.

30. Sahai, R. *Laboratory Evaluation of Proppant Transport in Complex Fracture Systems, [MS Thesis]*, Golden, Colorado: Colorado School of Mines. 2012.

31. Sahai R, Miskimins JL, Olson KE. Laboratory results of proppant transport in complex fracture systems. *SPE Hydraulic Fracturing Technology Conference*. 2014. doi:10.2118/168579-ms

32. Sahai R, Moghanloo RG. Proppant transport in complex fracture networks – A review, *Journal of Petroleum Science and Engineering*. 2019; 182: 106-199. doi: https://doi.org/10.1016/ j.petrol.2019.106199.

33. Saw EW, Shaw RA, Ayyalasomayajula S, Chuang PY, Gylfason A. Inertial clustering of particles in high-Reynolds-number turbulence, *Physical Review Letters*. 2008; 100(21). https://link.aps.org/doi/10.1103/PhysRevLett.100.214501

34. Segur JB, Oberstar HE. Viscosity of glycerol and its aqueous solutions. *Industrial and Engineering Chemistry*. 1951; 43(9): 2117-2120. doi:10.1021/ie50501a040

35. Stanier S, Blaber J, Take W, White D. Improved image-based deformation measurement for geotechnical applications. *Canadian Geotechnical Journal*. 2015; 53(5): 727-739. doi:10.1139/cgj-2015-0253

36. Stokes G. On the Effect of the Internal Friction of Fluids on the Motion of Pendulums. *Transactions of the Cambridge Philosophical Society*. 1851; 9: 8–106

37. Tomac I, Gutierrez M. Fluid lubrication effects on particle flow and transport in a channel. *International Journal of Multiphase Flow*. 2014; 65: 143-156. https://doi.org/10.1016/j.ijmultiphaseflow.2014.04.007.

38. Tomac, I, Gutierrez, M. Micromechanics of proppant agglomeration during settling in hydraulic fractures. *Journal of Petroleum Exploration and Production Technology*. 2015; 5: 417 - 434. https://doi.org/10.1007/s13202-014-0151-9

39. Tong S, Mohanty KK. Proppant transport study in fractures with intersections. *Fuel*. 2016; 181: 463-477. doi:10.1016/j.fuel.2016.04.144

40. Wen Q, Wang S, Duan X, Li Y, Wang F, Jin X. Experimental investigation of proppant settling in complex hydraulic-natural fracture system in shale reservoirs. *Journal of Natural Gas Science and Engineering*. 2016; 33: 70-80. doi:10.1016/j.jngse.2016.05.010

41. White DJ, Take WA. GeoPIV: Particle image velocimetry (PIV) software for use in geotechnical testing. *Cambridge University Engineering Department Technical Report 322*. 2002; 15.

42. Wong S-W, Geilikman M, Xu G. The geomechanical interaction of multiple hydraulic fractures in horizontal wells. *Effective and Sustainable Hydraulic Fracturing*. 2013. doi:10.5772/56385

43. Zhang X, Jeffrey RG, Thiercelin M. Deflection and propagation of fluid-driven fractures at frictional bedding interfaces: A numerical investigation. *Journal of Structural Geology*. 2007; 29(3): 396-410. doi:10.1016/j.jsg.2006.09.013

44. Zou Y, Zhang S, Ma X, Zhou T, Zeng B. Numerical investigation of hydraulic fracture network propagation in naturally fractured shale formations. *Journal of Structural Geology*. 2016; 84: 1-13. doi:10.1016/j.jsg.2016.01.004